UNIVERSITÀ DEGLI STUDI DI MILANO

Doctorate School in Chemical Sciences and Technologies

XXV Cycle

PhD Course in Chemical Sciences

03/A2 - Models and methods for chemistry

Local disorder in doped ceria: a crystallographic study

DOTTORANDO:
Mauro Coduri

TUTOR:
Dr. Marco Scavini

COORDINATOR:
Prof. Silvia Ardizzone

A.A. 2011/2012

Abstract

Local disorder in doped ceria: a crystallographic study

by

Mauro Coduri

In recent years, doped ceria compounds have attracted increasing attention as electrolytes for application in Solid Oxide Fuel Cell devices, thanks to their high performance at intermediate temperature. In cerium oxide, ionic conductivity is driven by the presence of oxygen vacancies, introduced for charge balance after doping with a lower valent cation. With increasing doping concentration the oxygen diffusion is impeded, probably because of the formation of aggregates that trap oxygen vacancies. Their nature is though still under debate.

Owing to the close interplay between transport properties and local structure, an accurate description of the defects on the atomic scale is of the utmost importance for understanding the mechanisms at work in doped ceria.

In this study we propose to unveil the complex disorder in doped ceria with a combined powder diffraction study. On the one hand, X-ray and Neutron powder diffraction are joint to couple their potentialities; on the other hand, two different crystallographic approaches are exploited.

The conventional crystallographic methods allow to study the long range structure modifications that occur with doping. The Pair Distribution Function is instead employed to study the local structure, in terms of deviations from the long range atomic ordering.

The goal of the thesis is to provide a crystallographic description of the atomic rearrangements induced by doping, looking for a relationship between the local structure and the transport properties.

This thesis is divided into 7 chapters. In the first chapter pure and doped ceria are introduced and a state of the art about the reports on structural investigations is given. In chapter 2, first the main concepts about powder diffraction are briefly recalled, then the Pair Distribution Function method is introduced. In chapter 3 some experimental details about the investigated samples and the instruments employed are provided.

The hearth of the thesis consists in the next three chapters, each one referred to a different thematic of interest on doped ceria. In chapter 4, the structural evolution upon doping is investigated by considering the whole compositional range of ceria-dopant oxide systems. A continuum of structural evolution is observed on both locally and on average. The Pair Distribution Function provides evidence that after doping, atoms locally rearrange in a different way than in the pure oxide. A model is proposed to account for these local deviations.

In chapter 5, samples having the same doping concentration, but a different dopant, were compared in order to establish the role of the dopants on the induced local disorder. Different dopants affect in a similar way the local structure of doped ceria, but differ in the magnitude of the induced distortion. The latter, as determined by XRPD or NPD, matches the trends of ionic conductivity observed in the literature.

The above mentioned studied were performed at low temperature, which is the best experimental condition for a crystallographic study aimed at unravelling static disorder. In chapter 6 we investigate the local structure under the real conditions of application of doped ceria, that is at high temperature and under controlled atmosphere. The doping-induced distortions are retained even at high temperature and are magnified when doped ceria is subjected to a reducing atmosphere. Finally, in chapter 7 some conclusions remarks are given.

Summary

1. Introduction

It was late spring 2012, when during a typical afternoon coffee break at the White Whale's bar, smoking a Toscano, my tutor told me "*At difference with my desk, disorder in oxides is an opportunity rather than a problem*". I immediately understood I had to write down this words and so I did.

I think there is no better way to introduce the leading wire of the present thesis: the disorder. Many interesting oxides are characterised by the presence of strong disorder which, in turn, is strictly related to their physical properties. In the present thesis the case of cerium oxide doped with trivalent cations is thoroughly investigated, trying to unravel disorder from a crystallographic point a view. Y and rare earth (*RE*) were considered as dopants.

In this first chapter we give a brief overview of doped ceria applications and of the work already done based on literature reports. Eventually, a crystallographic description of pure ceria and of the dopant oxides is given.

1.1. Disorder

Disorder is here defined as any deviation from an ideally infinite periodic structure. This definition includes both electronic and atomic structure. Focusing on the latter, disorder can be classified on the basis of its dimensionality, that is 0, 1 or 2.

Defects with 0 dimensionality are also called “point defects”.

Typical examples of mono-dimensional defects are dislocations while two-dimensional defects are, for example, antiphase domains, grain boundaries or even surfaces and interfaces.

In this work particular attention is devoted to “point defects” which are atomistic in nature and are confined to one or a few sites. To this purpose we will use the Kröger-Vink notation [*Kröger, 1977*] which allows not only to identify each defect with a concise symbol, but also to define equilibria among defects. Let’s consider, as an example, the formation of an anti-Frenkel (AF) defect in CeO_2 (fluorite structure, space group *Fm*-3*m*): some oxygen ions occupy the octahedral interstitial sites leaving vacancies in the tetrahedral

sites [*Mamontov and Egami, 2000, Mamontov et al., 2000*]. In the Kröger-Vink framework, it can be expressed as follows:

$$O_O \leftrightarrows V_O^{\cdot\cdot} + O_i^{''} \tag{1.1}$$

where $O_i^{''}$ means that an oxygen ion (main symbol) occupies an interstitial site (subscript) and has a double negative charge (superscript). At the same time an oxygen vacancy $V_O^{\cdot\cdot}$ (main symbol) occupies an oxygen site (subscript) and has a double positive charge (superscript). The equilibrium constant can be written as:

$$K_{AF} \leftrightarrows \frac{[V_O^{\cdot\cdot}][O_i^{''}]}{[O_O]} \tag{1.2}$$

If the concentration of AF defects is small, the $[O_O]$ term is in general omitted.

The charges shown according to the Kröger-Vink notation are not absolute values, but the difference between the oxidation state of the defect and the one foreseen by the same site in the reference structure. For this reason, the oxygen vacancy is considered "double positive charged" because in the ideal fluorite structure the same site is occupied by a O^{2-} ion.

The present study demonstrates that disorder could be more complex than predicted by point defect equilibriums.

1.2. Applications

Cerium oxide, in its pure or modified form, is a widely studied material due to its manifold applications (see [*Trovarelli, 2002*] and references therein). Generally it is not employed alone, but rather in combination with other metal oxides or with active metals. Here follows a short list of some of the major applications of cerium oxide:

- vehicle emission control to remove pollutants from vehicle (auto-exhaust) emissions. The main role played by CeO_2 is to mediate the amount of available oxygen in the catalytic converter.
- wet-oxidation process to decompose organic pollutants in wastewaters [*Trovarelli99*]
- polishing agent for most glass compositions [*Khaladji and Peltier, 1990*], particularly for glass decolorization. For example it is added to television faceplates to prevent darkening caused by to electron bombardment.
- treatment of SO_x to prevent catalysts pollution, e.g. in fluid catalytic cracking

- electrolyte in Solid Oxide Fuel Cell (SOFC) devices

Although the present work is not directly aimed to applicative aspects, all the structural investigations are performed, in terms of nature of samples and operating conditions, with reference to materials applied as electrolytes in SOFC.

1.3. Undoped ceria

Cerium oxide (CeO_2) exhibits fluorite structure, space group *Fm*-3*m*. Ce and O ions lie in the 4a (0,0,0) and 8c (¼, ¼, ¼) sites respectively. The fluorite structure is very stable over a wide range of *T* and oxygen non stoichiometry δ, defined as $CeO_{2-\delta}$. When CeO_2 is reduced to $CeO_{\sim 1.7\text{-}1.8}$, the structure is described by the so-called α phase, a disorder non-stoichiometric fluorite related phase [*Trovarelli, 2002; Bevan and Kordis, 1964*]. By further increasing the oxygen non-stoichiometry δ, a number of fluorite related superstructures were observed, lowering the cell symmetry owing to vacancy orderings, which likely occurs along the fluorite <111> direction. A comprehensive description of the superstructures in $CeO_{2-\delta}$ is given by a single crystal neutron diffraction study by Kümmerle and Heger [*Kümmerle and Heger, 1999*].

After atomistic calculations performed by Minervini *et al.* [*Minervini et al., 1999*], there are three possible intrinsic disorder reaction in ceria:

$$Ce_{Ce} + 2O_O \rightleftarrows V_{Ce}^{''''} + 2V_O^{\cdot\cdot} + CeO_2 \qquad \Delta E = 3.53 \text{ eV} \qquad (1.3)$$

$$Ce_{Ce} \rightleftarrows V_{Ce}^{''''} + Ce_i^{\cdot\cdot\cdot\cdot} \qquad \Delta E = 11.11 \text{ eV} \qquad (1.4)$$

$$O_O \rightleftarrows V_O^{\cdot\cdot} + O_i^{''} \qquad \Delta E = 3.2 \text{ eV} \qquad (1.5)$$

It is evident from above equilibriums that AF defects are the most common, while Frenkel defects, which imply the formation of Ce^{+4} ions in interstitial position is unfavoured. The concentration of such defects is anyhow limited in room temperature. The presence of interstitial O ions in pure ceria was observed to depend on the annealing process performed on the material [*Mamontov and Egami, 2000*].

As to transport properties, undoped ceria does not display particularly high ionic conductivity, because of the low concentration of oxygen vacancies. The trends of conductivity as a function of temperature and oxygen partial pressure (635<T<1500 °C, 10^{-20}<pO_2<1 atm) were deeply investigated in early times by Tuller and Novick **[***Tuller and Novick, 1979*] using also the previous data of Blumenthal and co-workers

[*Blumenthal et al., 1971***]**. By supposing small oxygen non-stoichiometry and negligible impurity concentration, the defect equilibrium is the following:

$$O_O \leftrightarrows \tfrac{1}{2}O_2 + V_O^{\cdot\cdot} + 2e' \tag{1.6}$$

The electrons produced in equilibrium (1.6) reduce Ce^{4+} to Ce^{3+} and electronic conduction is achieved via adiabatic small polaron hopping mechanism [*Tuller and Novick, 1977, Chiang et al. 1996, Oliva et al. 2004*]. The ionic conductivity σ_i can be expressed as [*Tuller and Novick, 1975*]:

$$\sigma_i = n_i \frac{\upsilon a^2 q^2}{4kT} \exp\left(-\frac{E_i}{kT}\right) \tag{1.7}$$

where $n_i = \left[V_O^{\bullet\bullet}\right]$, q is the charge, ν is a frequency factor, E_i is the activation energy for oxygen diffusion and a is the fluorite CeO_2 cell parameter ($a/2$ is the jump distance for an oxygen vacancy).

Nevertheless, electronic conductivity is not negligible in undoped ceria and dominates for high oxygen non stoichiometry. At high temperature (T= 1000°C) and under reducing atmosphere ($pO_2=10^{-6}$ atm) ionic conductivity contributes only for ~3% and cerium oxide behaves as *n*-type conductor [*Mogensen et al., 1994*]. Thus pure CeO_2 is not a candidate electrolyte for SOFC.

1.4.Doped ceria

In the present section, the main findings from literature reports are reviewed. *First*, the transport properties will be described, *then* the main finding of theoretical studies will be briefly discussed, *finally* we will focus on the experimental results. Due to their technological importance, particular attention will be devoted to *RE* = Gd, Sm and Y doping.

1.4.1. Transport properties

A schematic drawn of a SOFC is displayed in Fig. 1.1. In a SOFC, gaseous oxygen on the cathode side of the cell reduces to O^{-2}, diffuses through the electrolyte layer and combines with hydrogen (or other fuels) producing water and electrons. A good candidate electrolyte material for SOFC must then possess i) large O mobility and ii) negligible electronic conductivity, which would otherwise shortcut the cell.

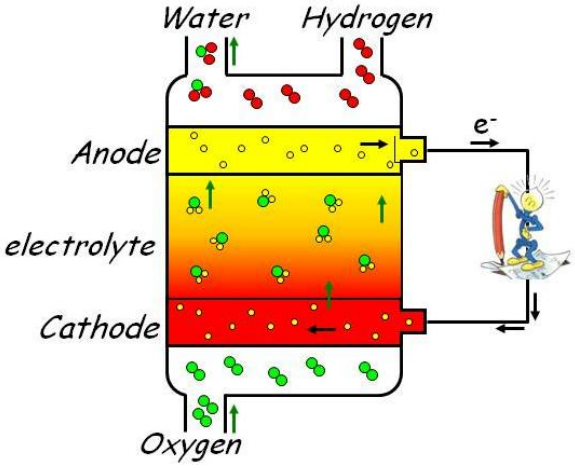

Fig 1.1. Scheme of a SOFC. green balls: O, red balls: H, yellow balls: electrons.

The most common electrolyte used in SOFC is yttria-stabilised zirconia, which is very stable under both reducing and oxidizing atmosphere, but requires high operating temperature (~1000°C) to exhibit high ionic conductivity [*Goodenough, 2003*]. Such high temperature requires an all-ceramic construction which raises the cost of the fuel cell. Overall manufacturing costs can be considerably reduced by operating at lower temperature. This is the case of doped ceria electrolytes, which maintain a high ionic conductivity even at intermediate temperatures (e.g. 500-700°C). On the other hand, the main limitation to the application of doped ceria in SOFC devices is the occurrence of electronic conductivity under reducing atmosphere, which diminishes the efficiency of the cell.

Although pure ceria (CeO_2) doesn't show a significant ionic conductivity, this can be raised by doping its fluorite structure with aliovalent RE^{3+} cations, giving rise to $Ce_{1-x}RE_xO_{2-x/2}$. In doped ceria RE^{3+} substitutes for Ce^{4+} and ionic conductivity occurs via oxygen diffusion through the vacancies formed by the following equilibrium:

$$(1-x)CeO_2 + \tfrac{x}{2}RE_2O_3 \rightleftarrows (1-x)Ce_{Ce} + xRE'_{Ce} + (2-\tfrac{x}{2})O_O + \tfrac{x}{2}V_O^{\cdot\cdot} \qquad (1.8)$$

Half an oxygen vacancy is introduced into the structure for each *RE* dopant in order to preserve charge balance. At large doping amount, the equilibrium (1.6) is moved leftwards and negligible electronic conductivity is observed over a wide *T* and pO_2 range. The above equilibriums are affected by the grain size, too [*Chiang et al., 1997*].

On the basis of equations (1.7) and (1.8), one can conceive that the isothermal σ_i should monotonically increase with n_i. Conversely, it decreases above a critical concentration x_c, although the total concentration of vacancies is increased and the CeO_2 based structure is preserved. This phenomenon is widely reported for *RE* = Gd [*Zhang et al., 2002, Zhang et al., 2004*], Sm [*Jung et al., 2002, Zhan et al. 2001*], Y [*Zhang et al., 2004, Sato et al., 2009, Wang et al., 1981*] and for the other trivalent *RE* dopants [*Faber et al., 1989, Dikmen et al., 1999*]. The critical concentrations x_c reported in the literature are much scattered and usually occur at around x_c=0.1-0.2, depending on the selected *RE* dopant, the sintering temperature and the synthesis routes

adopted. For example, in the case of *RE* = Gd, maxima at x_c~0.10 [*Steel, 2000*], 0.15 [*Zha et al., 2003*] and 0.20 [*Zhang et al., 2002*] were observed by different authors. The optimum concentration appeared to be temperature dependent [*Zhang et al., 2002*].

The solid electrolytes performance in fuel cell devices strongly depend on the selected *RE* dopant [*Faber et al., 1989, Kilner, 2008*]. In particular, among the *RE* lanthanides, the highest σ_i values are observed for *RE* = Gd and Sm [*Balasz and Glass, 1995, Eguchi et al., 1992*], while σ_i reduces by changing *RE* across the lanthanide series. Codoping has been also considered in order to improve conductivity [*Li et al., 1991, Yoshida et al., 2001, Omar et al., 2006, Omar et al., 2007, Zajac and Molenda, 2008*].

1.4.2. Theoretical calculations

It is clear from early Molecular Dynamic simulations that RE^{3+} dopant ions and oxygen vacancies do not disperse randomly in CeO_2, but likely interact with each other forming clusters, composed, at least, of *RE-RE* pairs [*Inaba et al., 1999*]. Thus, the experimental activation energy E_i for ionic conduction should contain a term for oxygen migration and another one for the interaction of a vacancy with other point defects. The latter should take into account both electrostatic attraction among charged defects and strain effects due to the size mismatch between the host structure and the solute [*Kilner, 2008*].

Due to simple electrostatic considerations, the presence of a vacancy induces the distortion of the fluorite cell in terms of oxygen relaxation toward the vacancy [*Hayashi et al., 2000*]. Such effect extends well beyond the adjacent ions and oxygen vacancies order preferably along curve chains [*Ye et al., 2009*].

Atomistic and DFT calculations suggested that the position of the dopant with regard to the vacancy (either Nearest Neighbor, NN or Next Nearest Neighbor, NNN) depends on the size of the dopant: cations smaller than Gd^{3+} prefer to be in a NN position with respect to the vacancy, while larger cations prefer a NNN vacancy [*Minervini et al., 1999, Andersson et al., 2006, Wei et al., 2009*]. The high performance of Gd- and Sm-doped ceria were then explained in terms of distribution of both low energy NN and NNN configuration, whereas for other *RE* dopants, either a NN or NNN configuration is heavily favored.

Genetic Algorithm [*Hooper et al., 2010*] and kinetic lattice Monte Carlo [*Dholabhai et al., 2010*] studies suggested that in highly doped ceria, some vacancy pairs are forced to assume a NN position. The resulting vacancy-vacancy repulsion impedes the vacancy diffusion, thus reducing the ionic conductivity.

As to the atomic arrangement of the vacancy-dopant associates, a continuous structural evolution with doping, from fluorite to C-type, was proposed by Li *et al* [*Li et al., 2011*] in the case of *RE* = Gd doping. On the other hand Wang *et al.* [*Wang et al., 2011*] predicted that for low Gd concentration, dilute defects arrange with pyrochlore structure.

1.4.3. Experimental results

Because of the conductivity drop, the application of doped ceria is usually limited to relatively low doping concentrations (usually x<0.25) where the fluorite structure is preserved. The solubility limit in fluorite depends on the single *RE* dopant and it is reported to be dependent even on the annealing route [*Grover and Tyagi 2004*]. Room Temperature CeO_2-RE_2O_3 phase diagrams are reported elsewhere for Gd [*Grover and Tyagi 2004, Grover et al., 2003*], Sm [*Nitani et al., 2004, Mandal et al., 2006*], Y [*Chavan et al., 2004*] and other dopants [*Nitani et al., 2004, Mandal et al., 2006, Chavan et al., 2005, Malecka et al., 2008*]. In most cases, among which *RE* = Gd, Sm and Y, highly doped systems produce a C-type structure (space group *Ia*-3). A-Type (hexagonal, *RE* = La, Nd [*Boucherle and Schweizer, 1975*]) and B-type (monoclinic, *RE* = Gd [*Grover and Tyagi 2004*], Sm [*Nitani et al., 2004*]) structures were also observed at room temperature in doped ceria. These three modifications of sesquioxides (RE_2O_3) are described in details in section 1.5.

Insights on local deviations from the average structure have been widely investigated in doped ceria by using EXAFS [*Yoshida et al., 2001, Nitani et al., 2004, Wang et al., 2006, Deguchi et al., 2005, Yamazaki et al., 2000, Yamazaki et al., 2001, Ohashi et al., 1998*], XANES [*Hormes et al., 2000*], Nuclear Magnetic Resonance (NMR) [*Kim and Stebbins, 2007, Heinmaa et al., 2010*], RAMAN spectroscopy [*Banerji et al., 2009*] and Neutron Diffuse Scattering [*Anderson and Cox, 1983*]. Evidence of dopant rich domains were provided by Electron microscopy [*Ye et al., 2008, Mori and Drennan, 2003, Ou et al., 2006a, Ou et al., 2006b, Ou et al., 2008, Ye et al., 2007, Ye et al., 2009b*]. Henceforth the findings of the above reports are summarized, showing *first* the investigation of the local structure in terms of cation-O and O vacancy distributions, *then* the possible relationships between the local structure evolution and the transport properties.

The above XANES measurements on doped ceria reported the tendency of Ce and *RE* dopants to retain their +4 and +3 oxidation states, respectively. This is not the case of *RE* = Pr [*Nitani et al., 2004*] and *RE* = Tb [*Martìnez-Arias et al., 2005*], which exhibit a mixed valence state. EXAFS experiments suggested that, except for *RE* = Pr and Tb, the Ce [N(Ce-O)] coordination numbers are larger than those of *RE* [=N(*RE*-O)] and they decrease by increasing doping amount. However, this is not consistent with above described atomistic simulations which locate vacancies in a NNN position with respect to the dopant. Moreover, literature reports do not agree about the effective coordination numbers: in the case of $Ce_{0.8}Y_{0.2}O_{1.9}$, as an example, different authors found out N(Y-O)~6 [*Wang et al., 2006*], ~6.5 [*Deguchi et al., 2005*] and ~7 [*Kim and Stebbins, 2007*], with the latter determined through Y^{89} MAS NMR spectroscopy.

After EXAFS measurements [*Yamazaki et al., 2000, Yamazaki et al., 2001*], on *RE*-doped samples (*RE*=Y, Nd, Sm, Gd, Yb) both Ce-O and *RE*-O interatomic distances decrease upon *RE* doping, even when the crystallographic cell expands, which is the case of *RE* = Gd, Sm. The shrinking of the *RE*–O interatomic distances was explained with the formation of defects association with two *RE* ions and one oxygen vacancy and/or four *RE* ions and two oxygen vacancies.

The shrinking upon doping of cation-O distances was confirmed by [*Nitani et al., 2004*] and [*Deguchi et al., 2005*] for all the *RE* dopants investigated, with the only exception of *RE* = La [*Deguchi et al., 2005*]. In this case the La-O pair is observed to increase upon doping, while the Ce-O distance shortens.

RE-O distances are usually larger than Ce-O, except for smaller cations, such as Y^{+3}. In this case, EXAFS [*Deguchi et al., 2005*] and MD simulations [*Hayashi et al., 2000*] probed shorter Y-O pairs, while a recent work by Burbano *et al.* [*Burbano et al., 2012*] suggested longer Y-O pairs than Ce-O, on the basis of a combined Reverse Monte Carlo and Molecular Dynamics approach. This finding was explained by the authors in terms of a stronger Coulombic attraction exerted by Ce^{+4}.

As to the O vacancies distribution, EXAFS studies [*Ohashi et al., 1998*] suggested that oxygen ions relax towards oxygen vacancies, as predicted by early Molecular Dynamics simulations [*Inaba et al., 1999*]. The first experimental confirmation came with a pioneered neutron diffuse scattering study by Anderson *et al.* [*Anderson and Cox, 1983*], who tested different dopants-vacancy clusters for M = Sc, Y. A more comprehensive description of possible O orderings in a fluorite parent structure (doped ZrO_2) was provided by Neder *et al.* [*Neder et al., 1992*] through a single crystal diffuse scattering study. Only a few EXAFS

experiments investigated also the cation-cation coordination shell for *RE* = Y [*Wang et al., 2006 Deguchi et al., 2005*], Gd and La [*Deguchi et al., 2005*]. Different Ce-Ce, Ce-*RE* and *RE-RE* distances were determined, the latter being always the longest one even for the small Y^{3+} ion. Since, as reported later on in this thesis, long *RE-RE* distances are retained in the C-type structure when one vacancy is shared by the two cations; this finding has been considered as a proof of $RE'_{Ce} - V_O^{\cdot\cdot}$ defects clustering. Both studies testified the strong tendency of RE^{3+} to associate with oxygen vacancies and to form *RE*-rich clusters, with a very limited coherence. In other words, the dopants retains its chemical environment as in its pure oxide. The development of C-type regions in the fluorite structure, as well as its evolution with doping, was supported by a RAMAN study [*Banerji et al., 2009*].

The presence of dopant-rich nanodomains is also consistent with the above mentioned High Resolution Transmission Electron Microscopy (HRTEM) studies. Their extent was observed to be strongly dependent on both the sintering temperature and the composition [*Mori and Drennan, 2003, Ou et al., 2006a*]. Higher sintering temperatures would favour the development of larger domains, which in turn reduce the ionic conductivity. For example, Ou *et al.* [*Ou et al., 2006a*] showed that in *x*=0.25 Y-doped ceria, domains appear by increasing the sintering temperature from 950°C to 1100°C. The same effect is observed by increasing the doping amount. The domains were observed to be rich in dopant [*Ye et al., 2007*] and with lower symmetry [*Ye et al., 2009, Ou et al., 2006b*] than the host fluorite structure. Selected Area Electron Diffraction (SAED) revealed in the domains the presence of diffuse scattering which develops in extra reflections at high doping amounts [*Ou et al., 2006a, Ou et al., 2008*]. In particular, Ye *et al.* [*Ye et al., 2009b*] were able to simulate SAED patterns for *RE* = Gd by considering 1-3 nm large spheres, randomly dispersed in a CeO_2 matrix. The oxygen ordering causes the lowering of the symmetry of the dopant rich-region and was consistent with a $I2_13$ space group. Electron Energy Loss Spectroscopy (EELS) measurements at the O-K absorption edge confirmed oxygen vacancy orderings in doped samples, which appeared to be strictly related to the selected *RE* dopant [*Ou et al., 2006b*].

A further possible relationship between structural parameters and transport properties was proposed by Yashima and Takizawa [*Yashima and Takizawa, 2010*] by studying the *mean square displacement* parameters (*msd*) in $Ce_{0.8}RE_{0.2}O_{1.9}$ (*RE* = La, Nd, Sm, Gd, Y, Yb). They observed that the *msd* increases with

the size mismatch between the host $r(Ce^{4+})$ and the dopant $r(RE^{3+})$ ionic radii and the isothermal ionic conductivity σ_i increases as long as *msd*(O) decreases.

To conclude, it is clear that when dopant ions enter the fluorite structure of CeO_2, instead of randomly distribute, they tend to form some kind of clusters/aggregates. Their structure is proposed to resemble the atomic arrangement of the pure oxides. To this purpose, in the next section, the structure of the A, B and C-type modifications of RE_2O_3 sesquioxides are described and compared to the fluorite structure of cerium oxide.

1.5. Pure oxides structures

1.5.1. Cerium oxide

As stated above, cerium oxide exhibits fluorite structure, space group *Fm*-3*m*. Ce and O ions lie in the 4a (0,0,0) and 8c (¼, ¼, ¼) sites respectively. As shown in the left-hand panel of Fig 1.2, Ce ions are in a cubic environment (8 next neighbor O ions) with polyhedra connected by edges along the <110> direction. Each anion is tetrahedrally coordinated to four cations. The anion substructure is cubic primitive, the cube centers being alternatively occupied by cations. The cubes share faces along the <100> direction. From an interatomic distances point of view, each cation is surrounded by a set of 8 equivalent O ions and 12 Ce ions. It is clear from the bottom part of Fig. 1.2 that a unique NN Ce-Ce distance is present.

1.5.2. Sesquioxides

Trivalent metal oxides in the form RE_2O_3 are defined sesquioxides. The phase diagram of sesquioxides is comprehensively reviewed by Adachi and Imanaka [*Adachi and Imanaka, 1998*] and more recently by Zinkevich [*Zinkevich, 2007*] focusing on thermodynamic aspects. Except for very high temperature, sesquioxides crystallize under three different polymorphs, designated as the hexagonal A-type, the monoclinic B-type and the cubic C-type. At Room Temperature (RT) Adachi and Imanaka, based on [*Foëx and Traverse, 1966*], indicated that all sesquioxides are in the C-type form, whilst Zinkevich [*Zinkevich, 2007*] proposed that La_2O_3 and Nd_2O_3 exhibit A-type structure, as described in section 1.5.2.2. The C-type structure is supposed to transform into a B-type at high temperature, the heavier the *RE* atom, the higher the temperature transition. Such transition is not observed to occur for the heaviest *RE* atoms, that is from Er to

Lu. The phase diagram is made more complicated by some irreversible phase transitions occurring at high temperature, especially regarding the C to B type phase transition. Grover [*Grover et al., 2003*] indicated that the high temperature (1300°C) ageing of Gd_2O_3 induces the stabilization of the B-type phase, which is retained even at RT. As indicated in chapter 4 of the present thesis, we observed that Sm_2O_3 sintered at 700°C exhibits C-type structure, while it transforms into B-type by increasing the annealing temperature up to 900 °C. Again this transition is irreversible upon cooling. The phase diagram is even affected by particle size: B-type Y_2O_3 was obtained by reducing the particle size down to less than 15 nm [*Guo et al. 2006*].

In the next section the basics characteristics of the above main RE_2O_3 modifications are reported, placing particular emphasis on the C-type structure, widely recalled in the rest of the thesis.

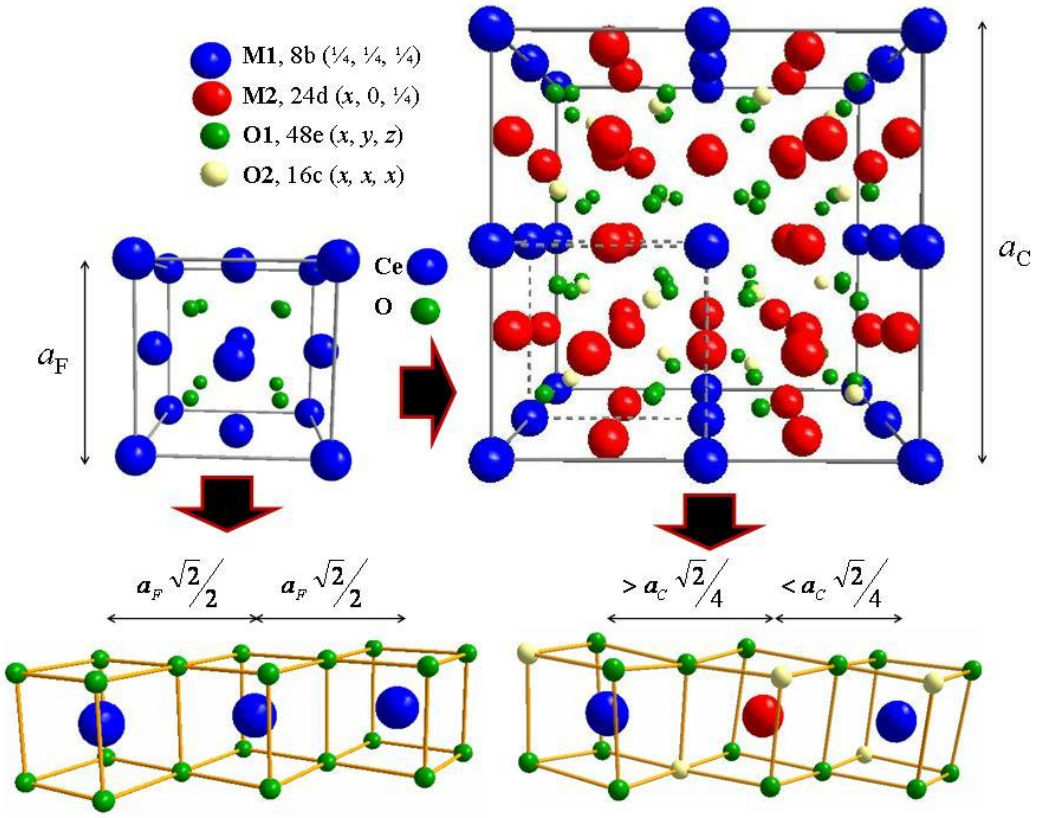

Fig 1.2. Top: fluorite (left) and C-type (right) structures. The M and O crystallographic sites in the C-type structure are also shown. Bottom: cationic environments for the two structures and their connectivity along the [1 1 0] direction. In fluorite all M-M distances are equal, while in C-type longer and shorter M-M distances are present. a_F and a_C are the fluorite and C-type cell constants respectively.

1.5.2.1. C-type

The C-type structure can be ideally built up from fluorite by eliminating 25% of oxygen ions and by oxygen vacancies ordering. As a consequence, the fluorite cell parameter doubles and both the cationic and anionic sites split into two non equivalent. The symmetry of the space group is reduced to *Ia*-3. The C-type is

displayed in the right-hand panel of Fig. 1.2. An octant in the C-type structure designated by dashed lines is compared to the fluorite structure on its left.

The C-type is usually reported with the same setting as Bixbyite, that is with the origin shifted by (¼, ¼, ¼) with respect to the fluorite structure. This is the same setting we adopt for sake of comparison with literature reports. In pure RE_2O_3, three different sites are defined: *RE*1: 8b, (¼,¼,¼); *RE*2: 24d, (*x*,0,¼); O1: 48e, *x,y,z* [*Faucher and Pennetier, 1980*]. Because of the doubling of the cell axis, except for O vacancies, when *x*(*RE*2) = 0 and O lies in (0.375, 0.125, 0.375), the atomic positions are the same as in fluorite.

In Fig. 1.2 the C-type structure is displayed with reference to the fluorite setting, that is by placing a *RE*1 site at the origin, to facilitate comparisons with fluorite. White balls stand for oxygen vacancies, located in the O2 site: 16c, (*x*, *x*, *x*), with *x* corresponding to 0.375 in case of a fluorite arrangement. This site is here mentioned because along the CeO_2-RE_2O_3 solid solution, the introduction of Ce in the C-type structure produces the partial occupation of the O2 site [*Grover and Tyagi 2004*]. The *RE*2 site is shown in red in the figure. It corresponds to the cation placed in the middle of the face diagonal in the fcc cation arrangement in fluorite. Its *x*(*RE*2) coordinate is reported to be ~0.03 for all the pure sesquioxides considered [*Hirosaki et al., 2003*]. By looking at the right-hand bottom panel of Fig. 1.2, one can observe that the cation in the *RE*1 site is surrounded by two O vacancies placed opposite to each other. Conversely, the cation in the *RE*2 site is surrounded by two O vacancies on the same side, which attract the cation off the center of the corresponding cuboid.

In the same panel the connectivity of the cation coordination polyhedra in RE_2O_3 is displayed. Each cation is surrounded by six full O1 sites and two empty O2 sites. Short *RE-RE* distances occur when the edge connecting two polyhedra are formed by two O1 sites, while long *RE-RE* distances involve the presence of one O2 site at the edge. This is different from the case of fluorite, where one single Ce-Ce is observed.

1.5.2.2. A-type

Although it is clear that the A-type polymorph exhibit hexagonal symmetry, the description of the space group in the literature is somewhat controversial. Adachi and Imanaka [*Adachi and Imanaka, 1998*] in their review indicated the A-type form has a "P32/m" space group, which is not in the space group standard notation. Early works suggested that the A-type structure possesses $P6_3/mmc$ space group [*Müller-Buschbaum and Schnering, 1965*], while now it is commonly accepted that the correct A-type space group is

P-3*m1* [*Boucherle and Schweizer, 1975*], with atoms in the *RE*1: 2d, (1/3,2/3,*z*); O1: 2d, (1/3,2/3,*z*) and O2: 1a, (0,0,0) sites. Three different *RE-RE* distances are present and cations gain a 7-fold coordination. Each cation is bound to four O1 and three O2 ions. The O1 oxygen site is coordinated to four cations, while O2 is bound to six cations.

A schematic A-type structure is drawn in Fig. 1.3.

1.5.2.3. B-type

The B-type is the monoclinic form of sesquioxides, space group *C*2/*m*. It is stabilized at high temperature, particularly for *RE* having intermediate ionic radii, such as Gd, Eu and Sm. The structure is more complex than the other polymorphs. Three cation sites are present, two of them being 7-fold coordinated to O ions, with the other one 6-fold coordinated. Five different O sites are in the unit cell.

A scheme of the monoclinic cell is drawn in Fig. 1.4.

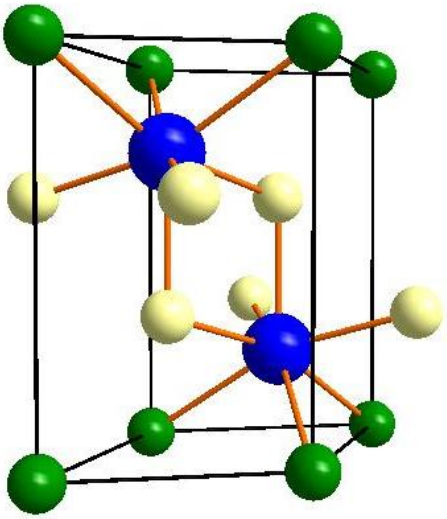

Fig 1.3. Schematic draw of the hexagonal A-type structure. Blue: RE1, white: O1, green: O2.

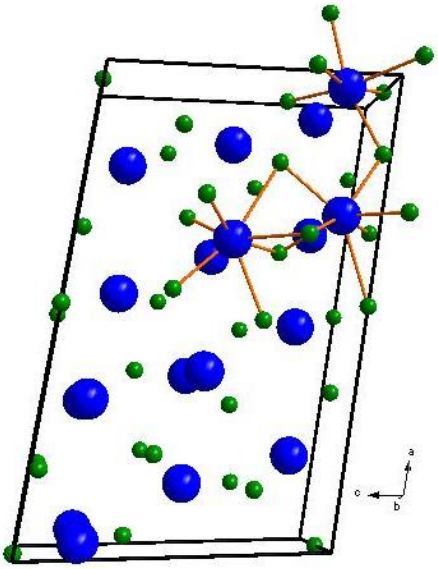

Fig 1.4. Schematic draw of the monoclinic B-type structure. Blue: cation sites, green: oxygen sites.

1.6. The rest of the thesis

In this first chapter pure and doped ceria were introduced, giving a brief review on the structural investigations conducted so far. To summarize the above findings, it is a shared opinion that defect associations among dopant and oxygen vacancies do exist in doped ceria. Different research groups, though,

disagree about the nature and the extent of defect clusters, the latter spanning between simple dopant-vacancy couples to nanodomains as large as few nanometers.

Aim of the present thesis is then to shed light on the complex defect structure of doped ceria, employing both X-ray and neutron powder diffraction. It is important here to recall that the present work is not aimed to the direct application of doped ceria, for which it is plenty of literature available (see e.g. [*Kilner, 2008*, *Goodenough, 2003*] and references therein). Here we propose to gain insight into the defects chemistry of doped ceria from a crystallographic point of view, being aware of the effective conditions required for their application. Also highly doped systems are investigated, to better appreciate the induced disorder. To this purpose we introduce the application of the Pair Distribution Function (PDF) method, i.e the real space analysis of the diffraction data, to doped ceria. We hope with the present study to add another brick in the wall of the knowledge of defect structure in doped ceria.

The PDF method is here combined with the conventional crystallographic approach, in order to study both average and local scale modifications induced by doping. The latter approach, defined as the reciprocal space analysis, is introduced in chapter 2, where some basics concepts about powder diffraction are recalled. The thesis assumes that the reader has a basic understanding of the main ideas of X-ray diffraction and crystallography, such as Bragg's law, Ewald sphere and reciprocal space. For a comprehensive description of these concepts the reader is referred to textbooks [*Giacovazzo et al., 2002*]. Still in chapter 2, we instead focus on the foundations of Pair Distribution Function. Being the PDF a relative less common field in crystallography, still in evolution and with many different formalisms, an overview of PDF is given.

In chapter 3, the instruments employed for this study are briefly described, together with the details of sample preparation and data collection. Emphasis is placed on the quality degree of data collections and to the accessible structural investigations, rather than on technical details.

From chapter 4 on, the results of the present work are shown and discussed in different examples. Each chapter concerns a different thematic related to doped ceria.

As stated above, the most interesting dopants for possible applications are Sm, Gd and Y. In chapter 4 we investigate the whole compositional range of the corresponding CeO_2-RE_2O_3 solid solutions employing high resolution X-Ray Powder Diffraction (XRPD). Since, as shown above, many studies suggested the tendency

of the dopant to form aggregates, the investigation of highly doped samples could be useful to understand how the dopant behaves even at low doping amount.

The role of the ionic radius of dopant is described in chapter 5. The application of Neutron Powder Diffraction (NPD) to doped ceria is exploited. The $x(RE)=0.25$ dopant composition, not far from the critical concentration corresponding to the peak in ionic conductivity, was investigated combining XRPD and NPD.

The aforementioned examples all refer to data collected at low temperature. In chapter 6 we try to fill the gap between the former measurements and the actual fuel cells' operating conditions. NPD was used to assess the stability of the average structure, whilst XRPD was employed to collect fast PDF under air and a reducing atmosphere. Final remarks are given in chapter 7.

References

[*Adachi and Imanaka, 1998*] G. Adachi and M. Imanaka, *Chem. Rev.* 1998, **98**, 1479-1514.

[*Anderson and Cox, 1983*] M. P. Anderson and D. E. Cox, *Solid State Ionics* 1983, **9 & 10**, 953-960.

[*Andersson et al., 2006*] D. A. Andersson, S. I. Simak, N. V. Skorodumova, I. A. Abrikosov, B. Johansson, *PNAS* 2006, **103**, 3518–352.

[*Balasz and Glass, 1995*] G. B. Balasz and R. S. Glass, *Solid State Ionics* 1995, **76**, 155-162.

[*Banerji et al., 2009*] A. Banerji, V. Grover, V. Sathe, S. K. Deba and A. K. Tyagi, *Sol. State Comm.*, **2009**, *149*, 1689-1692.

[*Bevan and Kordis, 1964*] D. J. M. Bevan and J. Kordis, *J. Inorg. Nucl. Chem.* 1964, **26**, 1509-1523.

[*Blumenthal et al., 1971*] R. N. Blumenthal, P. W. Lee and R. J. Panlener, *J. Electrochem. Soc.* 1971, **118**, 123-129.

[*Boucherle and Schweizer, 1975*] J. X. Boucherle and J. Schweizer, *Acta Cryst.* 1975, **B31**, 2745-2746.

[*Burbano et al., 2012*] M. Burbano, S. T. Norberg, S. Hull, S. G. Eriksson, D. Marrocchelli, P. A. Madden and G. W. Watson. *Chem. Mater.* 2012, **24**, 222-229.

[*Chavan et al., 2004*] S. V. Chavan, M. D. Mathews and A. K. Tyagi, *J. Am. Ceram. Soc.* 2004, **87**, 1977–1980.

[*Chavan et al., 2005*] S. V. Chavan, M. D. Mathews and A. K. Tyagi, *Materials Research Bulletin* 2005, **40**, 1558–1568.

[*Chiang et al. 1996*] Y.-M. Chiang, E. B. Lavik, I. Kosacki, H. L. Tuller and J. Y. Ying, *Appl. Phys. Lett.* 1996, **69**, 185-187.

[*Chiang et al., 1997*] Y.-M. Chiang, E. B. Lavik, I. Kosacki, H. L. Tuller and J. Y. Ying, *J. Electroceramics* 1997, **1**, 7-14.

[*Deguchi et al., 2005*] H. Deguchi, H. Yoshida, T. Inagaki and M. Horiuchi *Solid State Ionics* 2005, **176**, 1817-1825

[*Dholabhai et al., 2010*] P. P. Dholabhai, S. Anwar, J. B. Adams, P. A. Crozier and R. Sharma, *Modelling Simul. Mater. Sci. Eng.* 2012, 20, 015004.

[*Dikmen et al., 1999*] S. Dikmen, P. Shuk and M. Greenblatt, *Solid State Ionics*, 1999, **126**, 89–95.

[*Eguchi et al., 1992*] K. Eguchi, T. Setoguchi, T. Inoue, H. Arai *Solid State Ionics*, 1992, **52**, 165-172.

[*Faber et al., 1989*] J. Faber, C. Geoffroy, A. Roux, A. Sylvestre, and P. Abelard, *Appl. Phys.* 1989, **A49**, 225-232.

[*Faucher and Pennetier, 1980*] M. Faucher and J. Pannetier, *Acta Cryst. B* 1980, **36**, 3209-3211.

[*Foëx and Traverse, 1966*] Foëx, M. and Traverse, *J. P. Rev. Int. Hautes Temp. Refract*. 1966, **3**, 429.

[*Giacovazzo et al., 2002*] C. Giacovazzo, H. L. Monaco, D. Viterbo, F. Scordari, G. Gilli, G. Zanotti and M. Catti, in *Foundamentals of Crystallography*, 2002, Oxford University Press. See chapter 3.

[*Goodenough, 2003*] J. B. Goodenough, *Annu. Rev. Mater. Res.* 2003, **33**, 91–128.

[*Grover et al., 2003*] V. Grover, S. N. Achary and A. K. Tyagi, *J. Appl. Cryst.* 2003, **36**, 1082-1084.

[*Grover and Tyagi 2004*] V. Grover and A. K. Tyagi, *Materials Research Bulletin* 2004, **39**, 859–866.

[*Guo et al., 2006*] B. Guo, A. Harvey, S. H. Risbud and I. M. Kennedy, *Philosophical Magazine Letters* 2006, **86**, 457-467.

[*Hayashi et al., 2000*] H. Hayashi, R. Sagawa, H. Inaba and K. Kawamura, *Solid State Ionics* 2000, **131**, 281-290.

[*Heinmaa et al., 2010*] I. Heinmaa, T. Joon, H. Kooskora, J. Pahapill and J. Subbi, *Solid State Ionics* 2010, **181**, 1309-1315.

[*Hirosaki et al., 2003*] N. Hirosaki, S. Ogata and C. Kocer, *Journal of Alloys and Compounds* 2003, **351**, 31–34.

[*Hooper et al., 2010*] J. Hooper, A. Ismail, J. B. Giorgi, T. K. Woo, *Phys. Chem. Chem. Phys.* 2010, **12**, 12969–12972.

[*Hormes et al., 2000*] J. Hormes, M. Pantelouris, G. B. and B. Rambabu, *Solid State Ionics* 2000, **136–137**, 945–954.

[*Inaba et al., 1999*] H. Inaba, R. Sagawa, H. Hayashi and K. Kawamura, *Solid State Ionics* 1999, **122**, 95-103

[*Jung et al., 2002*] G. B. Jung, T. J., Huang and C. L. Chang. *Journal of the Electrochemical Society* 2002, **6**, 225-230.

[*Khaladji and Peltier, 1990*] J. Khaladji and M. Peltier, *Rare Earth Polishing Compositions*, U. S. Patent 4,942,691, 24 July 1990.

[*Kilner, 2008*] J. A. Kilner, *Chemistry Letters* 2008, **37**, 1012-1015.

[*Kim and Stebbins, 2007*] N. Kim and J. F. Stebbins, *Chem. Mater* 2007, **19**, 5742-5747.

[*Kröger, 1977*] F. A. Kröger, *Annu. Rev. Mater. Sci*., 1977, **7**, 449-475.

[*Kümmerle and Heger, 1999*] E.A. Kümmerle and G. Heger, *J.Sol.State. Chem.* 1999, **147**, 485-500.

[*Li et al., 1991*] P. Li, I.-W. Chen, J. E. Pennerhahn and T.-X. Tien, *J. Am. Ceram. Soc.* 1991, **74**, 958.

[*Li et al., 2011*] Z.-P. Li, T. Mori, F. Ye, D. R. Ou, J. Zou and J. Drennan, *Phys. Rev. B*, 2011, **84**, 180201.

[*Malecka et al., 2008*] M. A. Malecka, L. Kepinski, M. Maczka, *Journal of Solid State Chemistry* 2008, **181**, 2306– 2312.

[*Mamontov et al., 2000*] E. Mamontov, T. Egami, R. Brezny, M. Koranne and S. Tyagi, *J. Phys. Chem. B* 2000, **104**, 11110-11116.

[*Mamontov and Egami, 2000*] E. Mamontov and T. Egami, *J. Phys. Chem. Sol.* 2000, **61**, 1345-56.

[*Mandal et al., 2006*] B. P. Mandal, V. Grover, A. K. Tyagi, *Materials Science and Engineering A* 2006, **430**, 120–124.

[*Martìnez-Arias et al., 2005*] A. Martìnez-Arias, A. B. Hungrìa, M. Fernàndez-Garcìa, A. Iglesias-Juez, J. C. Conesa, G. C. Mather and G. Munuera, *Journal of Power Sources* 2005, **151**, 43-51.

[*Minervini et al., 1999*] L. Minervini, M. O. Zacate and R. W. Grimes, *Solid State Ionics* 1999, **116**, 339-349.

[*Mogensen et al., 1994*] M. Mogensen, T. Lindengaard, U. R. Hansen and G. Mogensen, *J. Electrochem. Soc.* 1994, **141**, 2122.

[*Mori and Drennan, 2003*] T. Mori and J. Drennan, *J Electroceram* **2006**, *17*, 749–757.

[*Müller-Buschbaum and Schnering, 1965*] H. Müller-Buschbaum and H. G. V. Schnering, *Zeitschrift für anorganische und allgemeine Chemie* 1965, **340**, 232-245.

[*Neder et al., 1992*] R. B. Neder, F. Frey and H. Schulz, *Acta Cryst.*, 1990, **A46**, 799-809.

[*Nitani et al., 2004*] H. Nitani, T. Nakagawa, M. Yamanouchi, T. Osuki, M. Yuya and T. A. Yamamoto, *Materials Letters* 2004, **58**, 2076-2081.

[*Ohashi et al., 1998*] T. Ohashi, S. Yamazaki, T. Tokunaga, Y. Arita, T. Matsui, T. Harami and K. *Solid State Ionics* 1998, **113-115**, 559–564.

[*Oliva et al. 2004*] C. Oliva, M. Scavini, O. Ballabio, A. Sin, A. Zaopo and Y. Dubitsky, *J. Sol. State. Chem.*, 2004, **177**,4104-4111.

[*Omar et al., 2006*] S. Omar, E. D. Wachsman and J. C.Nino, *Solid State Ionics* 2006, **177**, 3199.

[*Omar et al., 2007*] S. Omar, E. D. Wachsman and J. C.Nino, *Appl. Phys. Lett.* 2007, **91**, 144106

[*Ou et al., 2006a*] D. R. Ou, T. Mori, F. Ye, M. Takahashi, J. Zou and J. Drennan, *Acta Materialia* 2006, **54**, 3737-3746.

[*Ou et al., 2006b*] D. R. Ou, T. Mori, F. Ye and T. Kobayashi, *Appl. Phys. Lett.* 2006, **89**, 171911.

[*Ou et al., 2008*] D. R. Ou, T. Mori, F. Ye, J. Zou, G. Auchterlonie, and J. Drennan, *Phisical Review B* 2008, **77**, 024108

[*Sato et al., 2009*] K. Sato, K. Suzuki, K.; Yashiro, T. Kawada, H. Yugami, T. Hashida, A. Atkinson and J. Mizusaki, *Solid State Ionics* 2009, **180**, 1220-1225.

[*Steel, 2000*] B. C. H. Steele, *Solid State Ionics* 2000, **129**, 95–110.

[*Trovarelli et al., 1999*] A. Trovarelli, C. de Leitenburg, M. C. Boaro and G. Dolcetti, *Catal. Today* 1999, **50**, 353-367.

[*Trovarelli, 2002*] A. Trovarelli in *Catalysis by ceria and related materials*, 2002, Imperial College Press.

[*Tuller and Novick, 1975*] H. L. Tuller and A. S. Nowick, 1975, **122**, 255-259.

[*Tuller and Novick, 1977*] H. L. Tuller and A. S. Nowick, *J. Phys. Chem. Solids*, 1977, **38**, 859-867.

[*Tuller and Novick, 1979*] H. L. Tuller and A. S. Nowick, *J. Electrochem. Soc.* 1979, **126**, 209-217.

[*Wang et al., 1981*] D. Y. Wang, D. S. Park, J. Griffith and A. S. Nowick, *Solid State Ionics*, 1981, **2**, 95-105.

[*Wang et al., 2006*] Y. Wang, H. Kageyama, T. Mori, H. Yoshikawa and J. Drennan, *Solid State Ionics*, 2006, **177**, 1682-1685.

[*Wang et al., 2011*] B. Wang, R. J. Lewis and A. N. Cormak, *Acta Materialia* 2011, **59**, 2035-2045.

[*Wei et al., 2009*] X. Wei, W. Pan, L. Cheng, B. Li, *Solid State Ionics* 2009, **180**, 13–17.

[*Yamazaki et al., 2000*] S. Yamazaki, T. Matsui, T. Ohashi and Y. Arita, *Solid State Ionics* 2000, **136-137**, 913-920.

[*Yamazaki et al., 2001*] S. Yamazaki, T. Matsui, T. Sato, Y. Arita and T. Nagasaki, *Solid State Ionics* 2002, **154-155**, 113-118.

[*Yashima and Takizawa, 2010*] M. Yashima and T. Takizawa, *J. Phys. Chem. C*, 2010, **114**, 2385-92.

[*Ye et al., 2007*] F. Ye, T. Mori, D. R. Ou, J. Zou, G. Auchterlonie and J. Drennan, *J. Appl. Phys.* 2007, **101**, 113528.

[*Ye et al., 2008*] F. Ye, T. Mori, D. R. Ou, J. Zou, G. Auchterlonie and J. Drennan, *Solid State Ionics* 2008, **179**, 827– 831.

[*Ye et al., 2009*] F. Ye, T. Mori, D. R. Ou and A. N. Cormack, *Solid State Ionics* 2009, **180**, 1127-1132.

[*Ye et al., 2009b*] F. Ye, T. Mori, D. R. Ou, J. Zou and J. Drennan, *Solid State Ionics* 2009, **180**, 1414-1420.

[*Yoshida et al., 2001*] H. Yoshida, H. Deguchi, K. Miura, M. Horiuchi and T. Inagaki, *Solid State Ionics* 2001, **140**, 191–199.

[*Zajac and Molenda, 2008*] W. Zajac and J. Molenda, *Solid State Ionics* 2008, **179**, 154.

[*Zha et al., 2003*] S. Zha, C. Xia, G. Meng, *J. Power Sources* 2003, **115**, 44-48.

[*Zhan et al., 2001*] Z. L. Zhan, T.-L. Wen, H. Tu, Z.-Y. Lu, Z-Y, *J. Electrochem. Soc.* 2001, **148**, A427-A432

[*Zhang et al., 2002*] T. S. Zhang, P. Hing, H. T. Huang and J. A. Kilner, *Solid State Ionics* 2002, **148**, 567-573.

[*Zhang et al., 2004*] T. S. Zhang, J. Ma, L. B. Kong, S. H. Chan and J. A. Kilner, *Solid State Ionics* 2004, **170**, 209–217.

[*Zinkevich, 2007*] M. Zinkevich, *Progress in Materials Science* 2007, **52**, 597–647.

2. Introduction to powder diffraction

In the first chapter we introduced the materials under investigation in the present thesis. Here we describe the approach we employed to their investigation.

Powder diffraction is nowadays a routine technique for the characterization of crystalline materials. Its employ is often limited to the determination and quantification of crystalline phases. Nevertheless, a comprehensive investigation of powder diffraction patterns makes accessible a large amount of structural information. Often they are given by subtle modifications in the powder diffraction patterns, such as small variation in the intensity of diffraction peaks, peak splitting, small peaks popping up from the background or even peculiar shapes of diffraction peaks. These effects can be attributed to structural modifications, phase transitions and microstructure. When these effects only produce fine modulations of the diffraction intensity, their detection is precluded using laboratory instruments, because of their limited resolution and signal to noise ratio. High quality data for detailed crystallographic studies can be attained by exploiting the synchrotron radiation, which generally allows to tune the incident beam energy and is characterized by a large brilliance and a small instrumental contribution to peak broadening.

The coupling of X-rays to another probe, that is neutrons, can provide complementary information based on the different mechanism of interaction with matter.

The structural investigations were performed with two different approaches, defined as *reciprocal space* and *real space* analysis. The former is the conventional crystallographic method apt to determine the atomic arrangement in a crystal. The latter consists in the Pair Distribution Function (PDF) method, which describes the atomic structure from the interatomic distances point of view.

The present thesis assumes that the reader has a basic understanding of the foundations of diffraction and crystallography. For their derivation, the reader is referred to textbooks [*Giacovazzo et al., 2002, Stout and Jensen, 1989*].

In the next sections a few basics concepts of powder diffraction are recalled to introduce newcomers in the field of powder diffraction to the following chapters.

As to the *real space* analysis, being the Pair Distribution Function new to many scientists, it will be thoroughly introduced.

2.1.Reciprocal space analysis

Let us consider for the moment X-Ray Powder Diffraction (XRPD).

In a XRPD experiment, a monochromatic X-ray incident beam hits the sample, whose atoms scatter the beam at some scattering angle, defined as 2θ. The diffracted intensity is recorded by scanning a detector along 2θ.

A full treatment of the radiation-matter interaction is given, for example, in [*Giacovazzo et al., 2002*]. Here follows a qualitatively description after the classical mechanics to introduce some useful concepts.

Being the incoming beam an electromagnetic wave, it interacts with the charges present in the sample. When a charge is subjected to an electromagnetic wave with an oscillating electric field, is set into vibration. As a consequence, the vibrating charge emits radiation with the same frequency of the incident beam and a phase shift equal to π. The intensity of the emitted radiation has a reciprocal dependence with the square of the mass of the charged particle: X-rays are mostly scattered by electrons, which exhibit a mass by far smaller than that of protons.

By defining as $\mathbf{k}_0$ and $\mathbf{k}_f$ the wave-vectors associated to the incoming and diffused photon, the difference between the two is given by:

$$\boldsymbol{Q} = \boldsymbol{k}_f - \boldsymbol{k}_0 \tag{2.1}$$

According to the approximation of elastic scattering (Thompson scattering), since momentum is conserved, the $\boldsymbol{Q}$ vector can be replaced by its modulus:

$$\boldsymbol{Q} = |Q| = 2ksin\theta = 4\pi sin\theta/\lambda \tag{2.2}$$

The amplitude of the interference given by the electrons of a single atom is generally defined as the atomic scattering factor *f*. A fully constructive interference is only obtained in the case of Q=0, then it decays by reason of the spatial distribution of the electrons. An analytical description of the scattering factors is given for example in [*Waasmeier and Kirfel, 1995*].

Additional effects to the scattering factor are to be considered when the energy of the incident beam is close to an absorption edge of an element present in the sample. Its scattering factor will be modified as follows:

$$f(Q,E) = f^0(Q) + f'(E) + if''(E) \tag{2.3}$$

It is evident from equation 2.3 that also the phase of the scattering factor is affected. Suitable values for anomalous scattering are given in [*Brennan and Cowan, 1992*].

The observed diffracted intensity depends on the atomic coordinates and is proportional to the square modulus of the structure factor *F*,

$$I \div |F(Q)|^2 \tag{2.4}$$

with $F(Q)$ defined as:

$$F(Q) = \sum_{j=1}^{atoms} \mathrm{T_j} f_j exp\left[2\pi i \boldsymbol{Q}\boldsymbol{r}_j\right] \tag{2.5}$$

where $\boldsymbol{r}_j$ defines the atomic positions in respect to the origin of the axes and T_j accounts for thermal vibration and every further possible delocalization of the electronic cloud. Further details are given below. This approach is correct for every set of atoms, even in the absence of any symmetry rule. When dealing with a crystalline material, the whole crystal can be described by the translation of the content of a single unit cell according to linear combinations of the translational vectors **a**, **b** and **c**. The edges of the unit cell (*a*, *b* and *c*) as well as the angles between couples of vectors (α, β, γ) are defined as the cell parameters.

As a consequence, the structure factor of equation 2.5, can be described as the product of two different summations:

$$F(Q) = \left(\sum_{j=1}^{N} \mathrm{T_j} f_j(Q) exp\left[2\pi i \boldsymbol{Q}\boldsymbol{r}_j\right]\right)\left(\sum_{n=1}^{M} exp[2\pi i \boldsymbol{Q}\boldsymbol{R}_n]\right) \tag{2.6}$$

where $\boldsymbol{R}_n = u\boldsymbol{a} + v\boldsymbol{b} + w\boldsymbol{c}$ $(u, v, w = integers)$. The first one runs over the N atoms j in the unit cell, while the second summation stands for the sum over all the cells in the crystal. The latter summation produces non-null values only when the $\boldsymbol{Q}\boldsymbol{R}_n$ product is an integer number. This condition is fulfilled only when $\boldsymbol{Q}$ corresponds to a reciprocal space vector $\boldsymbol{r}_{\boldsymbol{H}}^*$:

$$\boldsymbol{Q}\boldsymbol{R}_n = \boldsymbol{r}_{\boldsymbol{H}}^*\boldsymbol{R}_n = (h\boldsymbol{a}^* + k\boldsymbol{b}^* + l\boldsymbol{c}^*)(u\boldsymbol{a} + v\boldsymbol{b} + w\boldsymbol{c}) = hu + kv + lw \tag{2.7}$$

where *h k l* are integer numbers, defined as Miller indexes. For these reasons, the present approach is defined in the following as the reciprocal space analysis.

The same results were geometrically derived by Bragg, describing the diffraction condition in terms of the reflection of the incident beam by a series of parallel planes:

$$n\lambda = 2dsin\theta \tag{2.8}$$

where *n* is an integer number, θ is half of the 2θ scattering angle, λ is the wavelength of the scattered photon and *d* is defined as the distance between two parallel consecutive crystallographic planes. After Bragg, the scattering condition amounts to the requirement that the path difference between waves reflected from successive planes should be an integer multiple of the wavelength of the incident radiation. Each plane is characterized by a tern of Miller indexes (*hkl*) which indicates that the *hkl* plane crosses the *a*, *b* and *c* cell axes at 1/*h*, 1/*k* and 1/*l* of their length. In Fig. 2.1 the interplanar distance *d* for the [111] reflection in cerium oxide (cubic) is shown. The corresponding XRPD pattern is shown in Fig. 2.2.

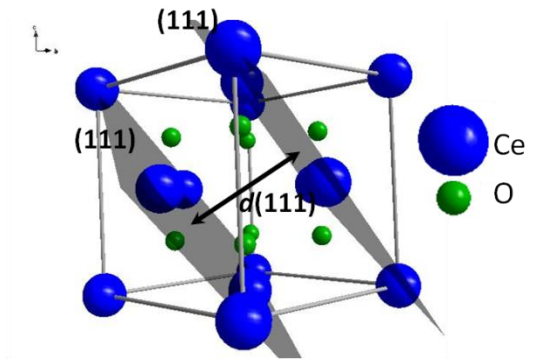

Fig 2.1. Sketch of the fluorite cell of CeO_2. Two parallel [111] planes are shown together with the corresponding interplanar distance *d*.

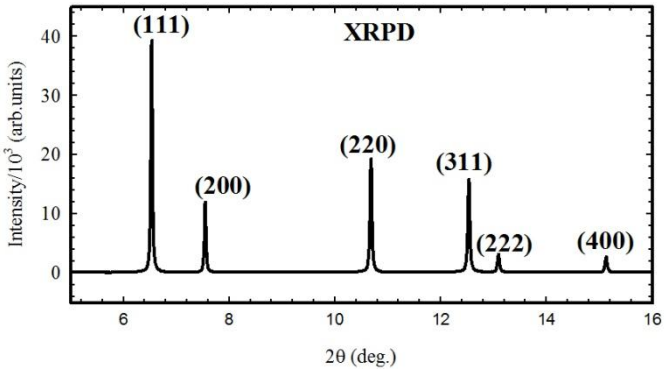

Fig 2.2. XRPD pattern of CeO_2. The corresponding Miller indexes are indicated.

It is clear from Fig. 2.2.that the <111> reflection exhibits the highest intensity and that the diffracted intensity decays with 2theta.

As described above, this occurs because of the delocalization of the scattering centers. In real materials, atomic vibrations induce a more spread distribution of the electronic cloud, thus producing an even faster intensity decay with 2theta. This effect is accounted for by the parameter T_j:

$$T_j = \exp\left(-8\pi^2 U^2 (sin\theta/\lambda)^2\right) \tag{2.9}$$

formerly introduced in equation 2.5 when defining the structure factor. In equation 2.9 *U* indicates the atomic *mean square displacement* around the equilibrium position. In the following, the term *U* will be referred to as "thermal parameter" or "*msd*".

The thermal parameters are a powerful tool for the study of disordered systems. Basically, disorder means that the equilibrium positions of atoms are locally moved away from their average crystallographic sites. As a consequence, the electronic cloud is more dispersed and the effect is, though to a larger extent, the same as a huge atomic vibration. This effect is thus detected in a diffraction experiment as the increase in the mean square displacements *msd*. In the approximation that the amplitude of atomic vibrations does not change with doping, or whatever originates disorder, disorder causes a rigid shift of *msd* towards higher values. Thus the overall thermal parameter can be described as follows [*Argyriou, 1994*]:

$$\langle msd \rangle^{exp} = \langle msd \rangle^{thermal} + \langle msd \rangle^{static} \tag{2.10}$$

where $\langle msd \rangle^{thermal}$ indicates the effective amplitude of vibration and $\langle msd \rangle^{static}$ is the additive contribution given by static disorder in atomic position.

Atomic vibrations reduce the structure factor, thus the intensity of a diffraction peak, without affecting its width. The width of a diffraction peak depends on two main contributions: one arising from instrumental effects, such as axial divergence, distribution of wavelengths and finite size of the beam; another one from the sample, in terms of extended defects. Finite grain size, strain effects, dislocations, antiphase boundaries and all other defects affecting the profile of a diffraction peak are defined as microstructure. The present thesis is mainly focused on the structural investigation, whereas microstructure is considered only qualitatively (see chapter 4). A comprehensive introduction to microstructure analysis is given in [*Mittemeijer and Scardi, 2004, Snyder et al., 1999*].

2.1.1. Neutron Powder Diffraction

The above results were referred to the employ of X-ray as a probe. In principle, every probe having a wavelength of the same order of interatomic distances in crystals is apt for studying the crystal structure of materials. In this thesis, XRPD is combined with Neutron Powder Diffraction (NPD).

Unlike X-ray radiation, neutrons interact with the nuclei of the atoms. Magnetic scattering is not of interest for the materials investigated in this thesis. The neutron scattering is given by short-range nuclear

forces. The scattering event occurs in a spatial region which is by 4 orders smaller compared to X-ray scattering. As a consequence, setting aside atom vibrations, the diffracted intensity is constant with 2theta.

When dealing with neutron, the scattering factor is usually indicates as the scattering length *b*, expressed in fm units. For X-ray scattering, the scattering length is obtained as follows:

$$b_X^0(\theta) = f^0(\theta) \cdot r_e \tag{2.11}$$

where r_e is the classical radius of the electron (2.812 Å). The neutron scattering length (b_N) has no linear trend along the periodic table and depends on the single isotopes. O atoms (5.803 fm) scatter neutron largely than Ce (4.84 fm) [*Sears, 2006*].

For the above reasons, the NPD and XRPD of the same material look different, as displayed in Fig 2.3 for ceria. For NPD the main peak is the [222] reflection and it is evident that the intensity falls off faster in case of X-ray.

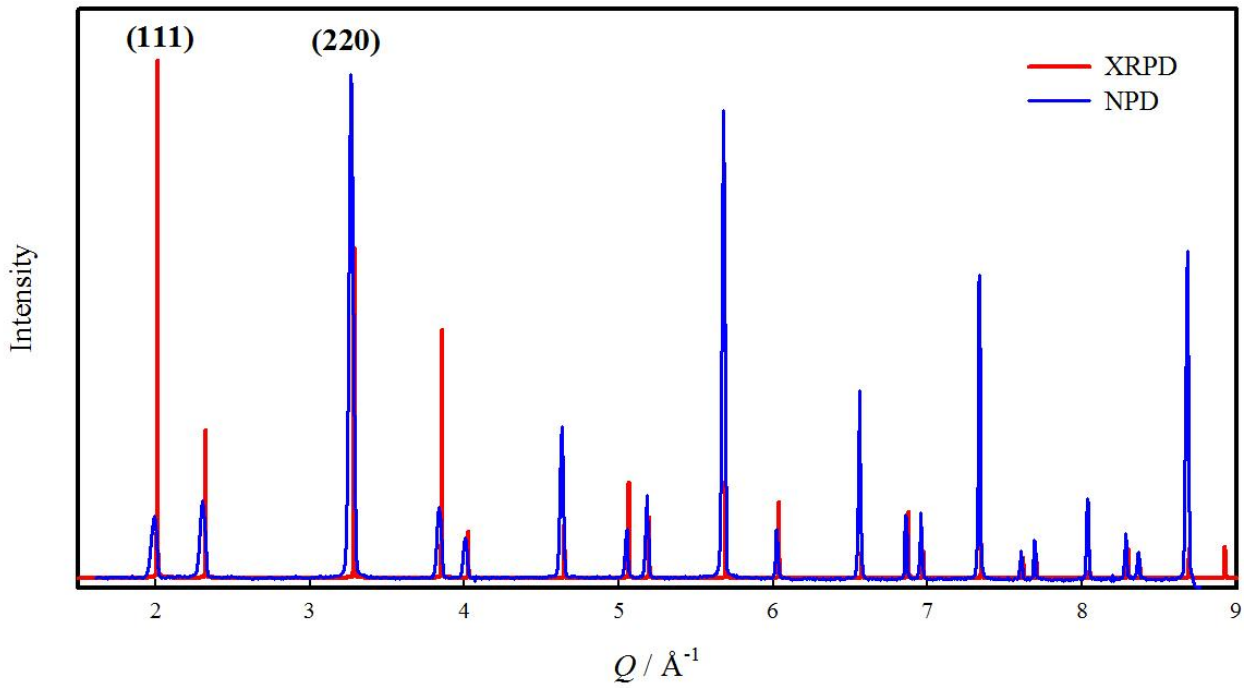

Fig. 2.3. XRPD (red) and NPD (blue) of CeO_2 collected at T = 90 K.

Being collected with two different wavelengths, the patterns are plotted in the *Q* space to get rid of the dependence on λ. It should be noted that the physical meaning of *msd* determined by XRPD and NPD is slightly different, since they originate from a different radiation-matter interaction. NPD probes the actual motion of the nuclei upon vibration. Conversely, being mostly sensitive to electrons, the XRPD *msd* can be affected by the non-spherical deformations of the valence electron-density distribution due to chemical bonding [*Blessing 1995*]. This is not expected to occur in the ionic crystals of this study.

The effect of *msd* on the diffracted intensity is evident by looking at the NPD patterns collected on pure CeO_2 by increasing temperature from 100 to 700°C. The effect is particularly evident for peaks at higher 2theta angles.

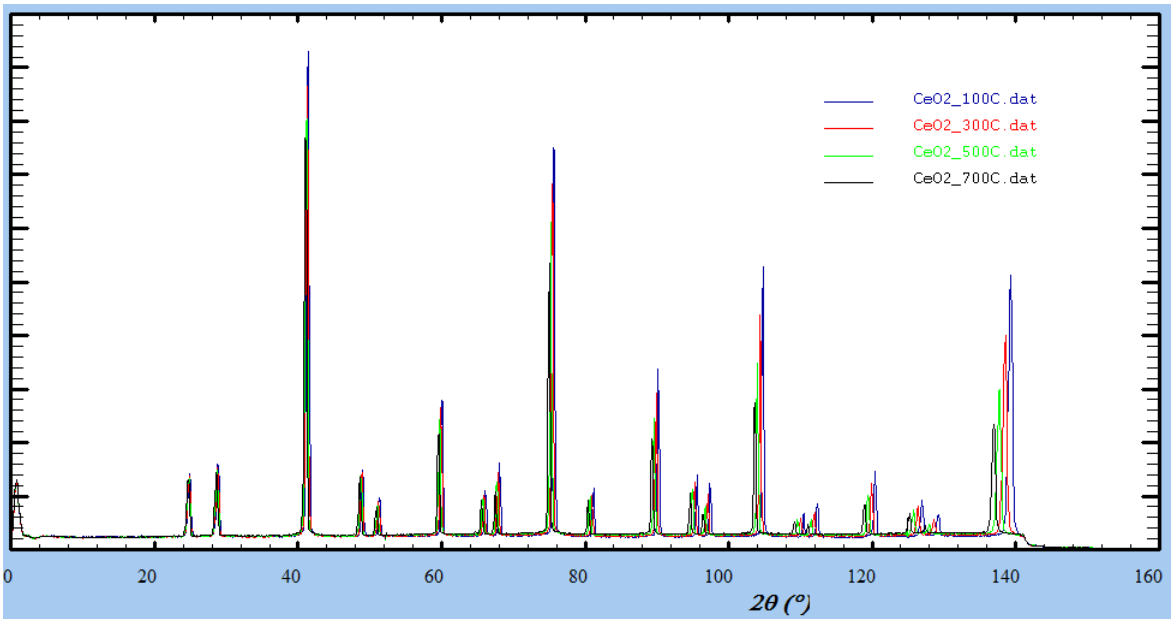

Fig 2.4. NPD patterns collected on CeO_2 from T = 100 to 700°C. Colors are defined in the inset. The data collection is described in chapter 6.

Finally, it's worthwhile noting that the use of NPD has also some drawbacks. A NPD experiment is not easily accessible. Whereas a XRPD pattern can be readily collected in every suitable equipped laboratory, either a reactor or a spallation source is necessary to provide neutrons. Moreover due to the limited cross section of the neutron scattering event, a very large amount of sample is often required (a few grams) to perform NPD, but not always it is available.

The investigation of some elements in their natural isotopic composition is precluded because of their large absorption. This problem can be overcome by employing isotopic enriched material, which are rather expensive.

2.1.2. Rietveld refinements

The structural information about the way atoms arrange in a crystal may be extracted by a powder diffraction pattern via the Rietveld method [*Rietveld, 1967*]. The experimental data are refined against a given structural model. The observed intensity y_{oi} at the angle i is compared to the corresponding calculated intensity y_{ci} as follows:

$$y_{ci} = s\sum_k m_k L_k |F_k|^2 G(2\theta_i - 2\theta_k)A + y_{bi} \quad (2.12)$$

where *s* is the scale factor, F_k the structure factor for the *k* reflection, $G(2\theta_i - 2\theta_k)$ is the profile function where $2\theta_k$ is the calculated Bragg angle corrected for the zero-point shift error, *A* is the linear absorption correction coefficient and $y_{bi}$is the background intensity. Generally, a Pseudo-Voigt function is employed to account for the profile. The goal of the Rietveld refinement is to minimize the residual *M* between the calculated and observed pattern:

$$M = \sum \omega_i |y_{oi} - y_{ci}|^2 \quad (2.13)$$

where ω_i is a weighting factor which depends on the standard deviation associates to the peak and to the background intensity.

The angular dependence of the peak broadening, described in terms of Full Width at Half Maximum (FWHM) is accounted for by the following empirical formula, according to the Gaussian component:

$$FWHM(\theta)_G = (Utan^2\theta + Vtan\theta + W)^{\frac{1}{2}} \quad (2.14)$$

and to the Lorentzian component:

$$FWHM(\theta)_L = Xtan\theta + Y/cos\theta \quad (2.15)$$

where U, V, W, X and Y are variable parameters.

Equation 2.14 is generally employed to determine the so-called Instrumental Resolution Function, that is the broadening of the diffraction peaks due to the instrument-related contributions, by refining the U, V and W parameters against the pattern of a standard material, in this study a certificated Si powder.

In this thesis, the following agreement factors, which testify the goodness of the fit, were considered:

$$R_{wp} = \left[M/\sum w_i y_{oi}^2\right]^{\frac{1}{2}} \quad (2.16)$$

$$R(F^2) = \frac{\sum|F_0^2 - sF_c^2|}{\sum|F_0^2|} \quad (2.17)$$

2.1.3. Data analysis strategy

The XRPD and NPD patterns were analyzed via the above described Rietveld method [*Rietveld, 1967*] as implemented in the GSAS software suite of programs [*Larson and Von Dreele, 2004*] which features the graphical interface EXPGUI [*Toby, 2001*]. The background was fitted by Chebyshev polynomials.

Absorption correction was considered negligible for NPD data, while for XRPD it was performed through the Lobanov empirical formula [*Lobanov and Alte da Veiga, 1998*]. Anomalous scattering *f'* and *f''* values were taken from [*Brennan and Cowan, 1992*] and line profiles were fitted using a modified pseudo-Voigt function [*Thompson et al., 1997*] accounting for asymmetry correction [*Finger et al., 1994*].

In the final refinement cycles, for samples having fluorite structure, the cell parameter and *msd* were allowed to vary along with background and line profile parameters. For samples having C-type structure, also positional coordinates and anisotropic *msd* parameters were refined.

When possible, *combined* XRPD and NPD refinements were performed on datasets collected at the same temperature: the profile parameters as well as the background coefficients were refined separately for both patterns, while the same structural model, in terms of *msd*, cell parameter and atomic coordinates, was applied to both datasets.

Except when explicitly indicated, site occupations were fixed to the nominal composition according to the formula $Ce_{1-x}RE_xO_{2-x/2}$.

2.2.The real space analysis

Deviations from a perfect periodic atomic arrangement give rise to diffuse scattering. Diffuse scattering is a coherent and inelastic form of scattering. In the reciprocal space analysis it is considered as a background feature and no modeling is generally performed. In principle, one can model diffuse scattering directly in the reciprocal space, see [*Anderson and Cox, 1983*] for example. A more straightforward approach to face the problem of the structural investigation of a disorder material is to consider the relative positions of atoms in a crystal, instead of the absolute ones. In contrast with the above mentioned reciprocal space approach, disordered materials are easier to handle in the space of the interatomic distances, that is the real space.

This is the case of the Pair Distribution Function method.

2.2.1. The Pair Distribution Function

The PDF provides the probability of finding a couple of atoms separated by a certain distance *r*. This section shows how to produce a PDF from a powder diffraction experiment. See [*Egami and Billinge, 2003*] for a complete derivation.

Basically, the PDF is obtained via Fourier Transform (FT) of the coherent intensity diffracted by the sample, after proper normalization.

The first step is the subtraction of the container contribution. This is done after measuring the diffraction pattern of the sample holder and, if necessary, of the empty apparatus.

The coherent diffracted intensity is given by two contributes: the Bragg peaks, as described in section 2.1, and the diffuse scattering. The coherent diffracted intensity $I_{coh}(Q)$ is though only a part of the overall diffracted intensity $I_0(Q)$:

$$I_0(Q) = P \cdot A \cdot N[I_{coh}(Q) + I_{inc}(Q) + I_{ms}(Q) + ..] \tag{2.18}$$

In equation 2.18, P is the polarization factor, A the absorption coefficient, N a normalization factor, $I_{inc}(Q)$ is the incoherent intensity, $I_{ms}(Q)$ is the multiple scattering contribution.

The Polarization correction is often non necessary, since P approaches unity when employing synchrotron radiation. The other corrections are generally performed with tabulated values. Multiple scattering occurs when the incident beam is scattered twice or more before reaching the detector. A suitable correction is given in [*Dwiggins and Park, 1971*].

The incoherent scattering is the most problematic correction to perform. In case of X-ray scattering, it is generally present in the form of Compton scattering and is non-negligible especially when working at high energy. Since it increases with Q whilst the coherent intensity decreases, even small error in Compton correction can lead to significant error in the high-Q correction [*Young 1993*]. As to NPD, the velocity of the neutron is of the same order of the one of vibrating atoms. As a consequence the modulus of $\mathbf{k}_f$ can significantly differ from $\mathbf{k}_0$. This problem is overcome by using the Placzek correction [*Plackek 1952, Egami and Billinge 2003*].

Consider finally that in equation 2.18 only the main corrections are reported, but others are generally necessary, depending on the instrument set-up, the type of detectors, the experimental condition and the probe employed.

Once obtained the coherent diffracted intensity $I_{coh}(Q)$, which is the results of Bragg and diffuse scattering contributions, it needs to be properly normalized before FT. The normalized coherent intensity, also defined as total scattering function, is shown in equation 2.19:

$$S(Q) = \frac{I_{coh}(Q) - \langle b^2(Q)\rangle + \langle b(Q)\rangle^2}{\langle b(Q)\rangle^2} \tag{2.19}$$

where $\langle b(Q)\rangle^2 = [\sum_i c_i\, b(Q)_i]^2$ and $\langle b^2(Q)\rangle = \sum_i c_i [b(Q)_i]^2$ are the square of mean and the mean of square scattering lengths weighted over the concentration of the i^{th} atom in the sample. This makes the high-Q region oscillating around the unity. Note that in equation 2.19 the Q-dependence of the scattering length b is indicated with reference to X-ray scattering.

A typical XRPD S(Q) curve of doped ceria is shown in Fig. 2.5 (*a*).

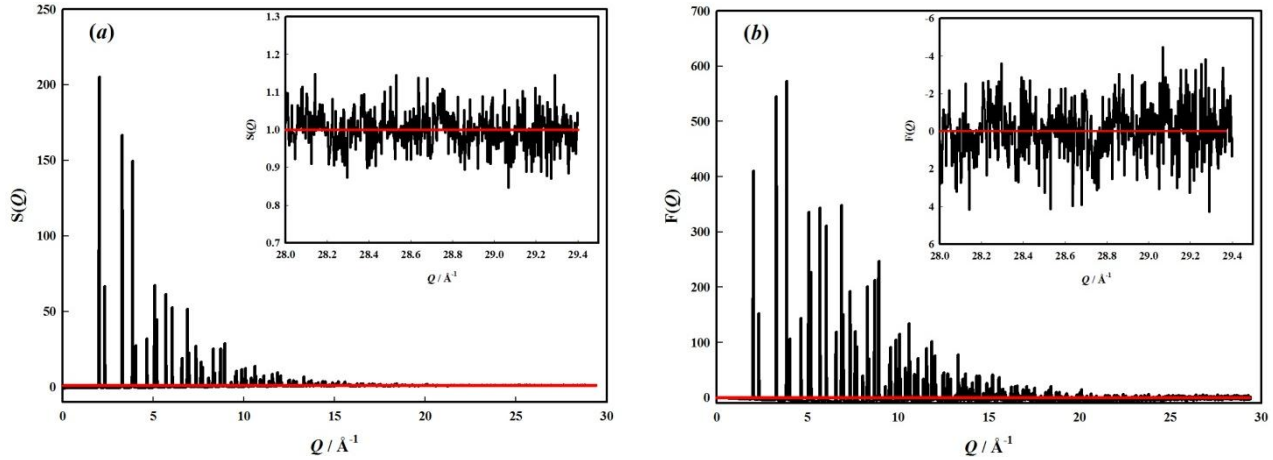

Fig. 2.5. S(Q) (*a*) and F(Q) (*b*) curves determined on a 25% Y-doped ceria sample. The inset indicates the high-Q region.

In Fig. 2.5 (*b*) the so-called reduced structure F(Q) is shown. It's derivation from S(Q) is trivial:

$$F(Q) = Q[S(Q) - 1] \tag{2.20}$$

In equation 2.20 F(Q) is obtained by multiplying S(Q)-1 by Q. This means that at high Q values, the dispersion of experimental data around the mean value is magnified. The same applies to noise. Note that in Fig. 2.5 (*b*) the scale in the inset has been modified in order to accommodate for larger oscillations.

There are different formalisms in the definition of the actual Pair Distribution Function. An overview is given by Keen [*Keen, 2001*]. In the present thesis, we refer to G(r), defined as the sine Fourier Transform of total scattering function S(Q):

$$G(r) = \frac{2}{\pi}\int_0^\infty Q[S(Q) - 1]\sin(Qr)\, dQ = \frac{2}{\pi}\int_0^\infty F(Q)\sin(Qr)\, dQ \tag{2.21}$$

Equation 2.21 indicates that G(r) is obtained after integration over an infinite range of Q. This is obviously not possible, and the maximum Q value (Q_{max}) accessed experimentally is determined by the incident wavelength and the maximum 2theta value (see equation 2.2). By reason of the limited Q_{max}, *S(Q)* is

multiplied by a step function [=1 for $Q \leq Q_{max}$; = 0 for $Q > Q_{max}$], that in real space produces the convolution of G(r) with a broadening function, given by

$$\frac{\sin(Q_{max}\Delta r)}{\Delta r} \tag{2.22}$$

corresponding to the FT of the step function [*Toby and Egami 1992*]. By increasing Q_{max} the truncation induced broadening becomes negligible with respect to the thermal broadening. The Q_{max} termination produces the appearance of spurious oscillations in G(r) with wavelength ~ $\frac{2\pi}{Q_{max}}$. They are defined as "termination ripples" and are evident at low r aside each peak. In general, the intensity of termination ripples is damped by increasing the overall thermal parameter. Toby and Egami [*Toby and Egami 1992, Egami 2004*] provided a rule of thumb to face this problem: termination effects are negligible when Q_{max} is greater then $\frac{3}{2\langle msd \rangle}$, where $\langle msd \rangle$ is the average mean square displacement.

The presence of ripples can also arise by a non-correct high-Q normalization, as shown by [*Peterson et al., 2003*]. A limited Q_{max} would also produce a further broadening of the peaks with increasing r-interatomic distances and would reduce the resolution in the real space. Basically, in order to reduce these artifacts, data have to be collected on a very large Q range. At Q_{max} ~30 Å^{-1}, termination effects should be negligible, but the correct Q range to investigate depends on the sample and the instrument set-up and, most important, a high Q_{max} is not the only condition to fulfill in order to acquire reliable data. Indeed, higher Q_{max} are obtained by increasing the 2theta range over which data are collected. We have to consider, though, that noise is cumulative: due to the intensity decay with 2theta, the higher the Q-value, the higher the noise. This effect is evident in Fig 2.5. Data are then to be collected for longer times at high Q in order to increase the signal-to-noise ratio. Conversely, noise is constant with r in G(r) curves.

When ripples (or noise) strongly affect the low-r peaks in PDF, a possible correction is proposed by Lorch [*Lorch, 1969*], by multiplying S(Q) with a damping function before FT. This facilitates the high-Q normalization of S(Q) and minimizes the possible contribution of ripples, at the expense of an additional peak broadening. This procedure was not employed in this thesis, except when otherwise stated in chapter 6. Provided that the counting statistics does not affect the quality of our data, the effect of Q_{max} can be observed by calculating G(r) starting from a structural model after convolution with the *sinc* function described in 2.22 according to different Q_{max} values.

A G(r) function can be calculated based on a structural model according to:

$$G(r) = \frac{1}{r}\sum_i \sum_j \left[\frac{b_i b_j}{\langle b \rangle^2}\delta(r - r_{ij})\right] - 4\pi\rho_0 r \tag{2.23}$$

with the sum running over the atoms i and j separated by a distance r_{ij}. Note that equation 2.23 does not account for atomic vibrations. To this purpose, the delta term can be replaced by a modified Gaussian function [*Neder and Proffen, 2009*]:

$$T_{ij}(r) = \frac{1}{\sqrt{2\pi}\sigma_{ij}(r)} exp\left[-\frac{(r - r_{ij})^2}{2\sigma_{ij}^2(r)}\right] \cdot \left[1 + \left(\frac{r - r_{ij}}{r_{ij}}\right)\right] \tag{2.24}$$

where $\sigma_{ij}(r)$ is related to the *msd* of atoms i and j. In some cases the 1st neighbors pairs are subjected to correlated motion, which produces a sharpening of some peaks in the low-r region. This effect is detailed in [*Jeong et al., 1999*].

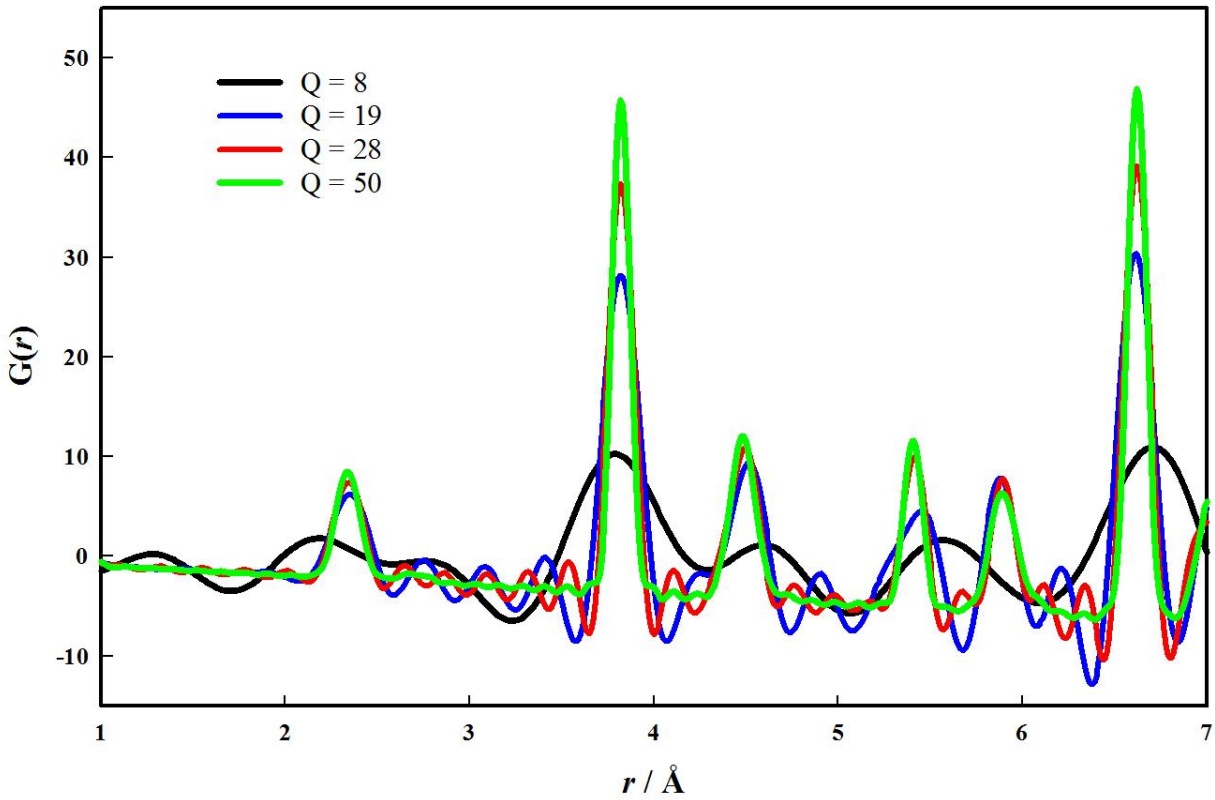

Fig. 2.6. Calculated G(r) for CeO_2, considering low temperature structural parameters, as determined in this study. The Q_{max} values indicated are in $Å^{-1}$ units.

In Fig. 2.6 XRPD G(r) curves are calculated based on the CeO_2 low temperature structural model described in chapter 4 terminating the FT at different Q_{max}.

It is evident from Fig 2.6 that to get rid of ripples one should collect data up to very high Q_{max}. The black curve refers to Q_{max} = 8 $Å^{-1}$ and corresponds to the PDF that one can obtain by employing a laboratory

diffractometer equipped with a Cu anode. Modern diffractometers can have a Mo, or even Ag anode, which allows to access higher Q_{max}, around 20 Å^{-1}. The corresponding PDF is reported in blue. The data of the present study are terminated to Q_{max} = 28 Å^{-1} and are shown in red. Again some ripples are present and are discussed in chapter 4. Ripples almost disappear only reaching Q_{max} = 50 Å^{-1}.

After equation 2.23, all G(r) curves have a negative slope in the $r \to 0$ limit. In the limit of large r, G(r) will instead tend to zero. The amplitude of the oscillations gives a direct measure of the structural coherence of the sample. For example, when dealing with nanoparticles, for interatomic distances larger than the size of the particle, the coherence is lost and the G(r) will fall to zero. The finite size effect is described in [*Kodama et al., 2006*] for nanoparticles having different shapes.

Another source of damping of the G(r) amplitude with r is given by the limited instrumental resolution. The lower the instrumental resolution, the faster the G(r) amplitude decays with r. Generally X-ray diffractometers feature a constant $\Delta Q/Q$ resolution, which can be easily modeled [*Egami and Billinge, 2003*]. In case of NPD, the resolution is often dependent with Q, some corrections are provided in [*Qiu et al., 2004*].

Finally, another commonly employed function is the Radial Distribution Function R(r), which can be derived from G(r) by adding and multiplying constants:

$$R(r) = r[G(r) + 4\pi r\rho_0] \tag{2.25}$$

where ρ_0 stands for the number density of the material (number of atoms in the cell divided by its volume). In principle, R(r) is the most physically intuitive way to describe the PDF, since the integration of R(r) provides the coordination number, or number of neighbors, in a certain interatomic distance range between r_1 and r_2:

$$Nc = \int_{r1}^{r2} R(r)dr \tag{2.26}$$

The main problem in determining Nc from PDF data is that one should know a priori which atoms contribute to a certain peak, which is not always straightforward in disordered materials. In addition to that, no peak overlap should occur. The first neighbors peak is often affected by the presence of termination ripples which introduces a bias in the correct fit of the peak. See [*Fischer et al. 2006*] and references therein, or [*Svab and Hajdu, 1994*], for useful indications for calculating Nc from PDF.

2.2.2. Differential PDF

One of the limitations of the PDF approach is that it is apparently not possible to recover an element sensitive information. A differential pair distribution function can be employed to circumvent this problem [*Egami and Billinge 2003, Fischer et al., 2006*].

Let's consider to collect two powder diffraction patterns, the differences of which are related to only one of the atoms present in the sample. The differential PDF obtained by subtracted the two datasets will only refer to pairs involving the investigated atom.

This can be done with neutrons by isotopic substitution, see e.g. [*Louca et al. 1999*]. In case of XRPD, it is possible to exploit the anomalous scattering phenomenon around an absorption edge. By collecting XRPD patterns at two slightly different energies just below an absorption edge (say Ce K-edge), the difference of the two patterns will be only related to the absorber atom, in this case Ce, by virtue of the difference of the anomalous f' contribution to the overall scattering factor. Obviously, the variation in energy should affect only the absorber atom.

Part of the data shown in this thesis were collected with the goal of carrying out an anomalous differential PDF study on doped ceria. This is the reason why some measurements were performed just below the Ce absorption K-edge. Some first results were published in [*Allieta et al., 2011*] and [*Allieta, 2012*]. The project is still in progress and a lot of work has to be done yet, thus the application of differential PDF goes beyond the goal of this thesis.

2.2.3. PDF on CeO_2

CeO_2 is the reference material of this study. In this section we discuss the main features of PDF curves employing XRPD and NPD. First of all, since in a fluorite structure only special positions are occupied (atomic coordinates are fixed by symmetry), it is possible to determine a priori all the atom pair distances based on the value of the cell parameter *a*.

The Ce-O, O-O and Ce-Ce distances can be determined as follows:

$$d(Ce-O) = \sum_{N=0} \frac{a}{4}\sqrt{3+8N} \tag{2.27}$$

$$d(O-O) = \sum_{N=1} \frac{a}{2}\sqrt{N} \tag{2.28}$$

$$d(Ce-Ce) = \sum_{N=1} \frac{a}{2}\sqrt{2N} \tag{2.29}$$

It turns out from equations 2.28 and 2.29 that O-O pairs contribute to all the peaks involving Ce-Ce pairs. The main distances of interest in study are reported in Table 2.1, together with pair multiplicity, the relation to the cell parameter *a* and the distance calculated based on the cell parameter *a* at RT.

Table 2.1. Some information (direction, multiplicity, dependence with cell parameter *a* and the value in Å units for a reference CeO_2 at RT) about the principle atom pairs mentioned in the text.

pair	*direction*	*mult.*	*distance*	*RT CeO_2*
1st M-O	<111>	8	$\frac{a}{4}\sqrt{3}$	2.34 Å
1st O-O	<100>	6	$\frac{a}{2}$	2.72 Å
1st M-M	<110>	12	$\frac{a}{2}\sqrt{2}$	3.82 Å
2nd O-O	<110>	12	$\frac{a}{2}\sqrt{2}$	3.82 Å
2nd M-O	<131>	24	$\frac{a}{4}\sqrt{11}$	4.49 Å
3rd O-O	<111>	8	$\frac{a}{2}\sqrt{3}$	4.69 Å
2nd M-M	<100>	6	a	5.41 Å
4th O-O	<100>	6	a	5.41 Å
3rd M-O	<133>	24	$\frac{a}{4}\sqrt{19}$	5.90 Å
5th M-M	<130>	24	$\frac{a}{2}\sqrt{10}$	8.55 Å
7th M-M	<123>	48	$\frac{a}{2}\sqrt{14}$	10.12 Å

Note that in equation 2.23 G(*r*) is weighted over the scattering lengths of the atoms involved in the pair. For this reason, the coexistence of some Ce-Ce and O-O pairs at the same distance is not a problem in case of XRPD scattering. The calculated G(*r*), based on equation 2.23 are shown in Fig. 2.7 for XRPD (*a*) and NPD (*b*) data. The contributions of the G(*r*) due the single atom pairs is also shown.

The different slopes observed in Fig. 2.7 are due to the smaller number density calculated considering only a fraction of atom pairs. No truncation error has been considered. Note that the G(*r*) scale of panel (*b*) is reduced, according to the lower neutron scattering lengths compared to X-rays. In case of XRPD, the contribution of O-O pairs is negligible: spurious oscillations, coming either from truncation error or noise, would cover the O-O peaks. This is not case of NPD: the peak at ~2.7 Å is now evident and to the peak ~3.8 mainly O-O pairs contribute. It is thus more difficult, employing NPD diffraction, to resolve features related to only Ce-Ce pairs.

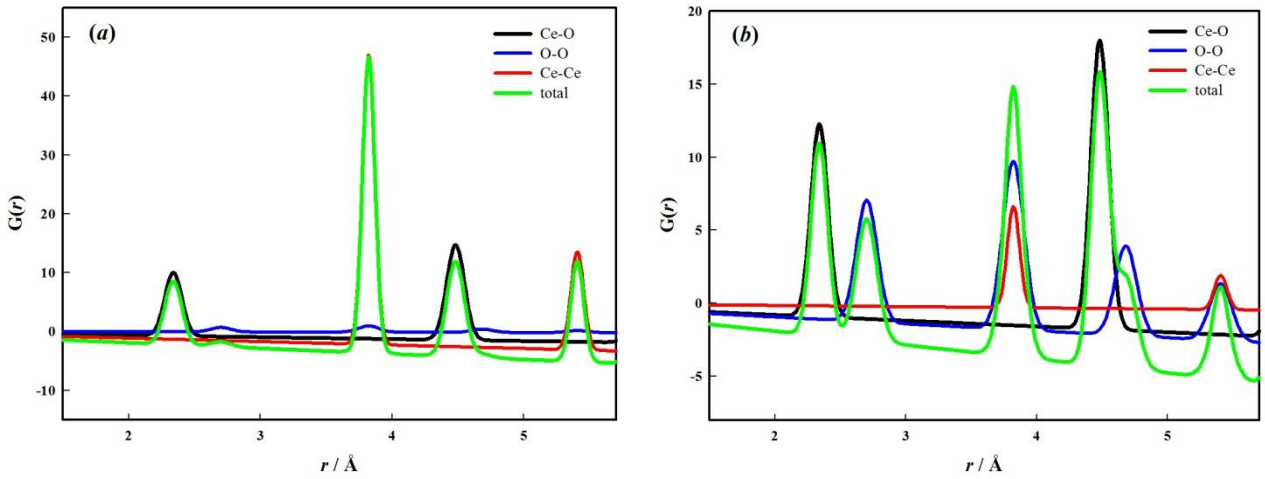

Fig. 2.7. Calculated G(*r*) for CeO_2 considering XRPD (*a*) and NPD (*b*).

2.2.4. Data analysis strategy

XRPD real space data reported in chapters 4 and 5 were processed using the PDFGetX2 software [*Qiu et al., 2004b*]: data were corrected for background, sample self-absorption, multiple and Compton scattering. XRPD data reported in chapter 6 were processed with the PDFGetX3 software [*Billinge and Farrow, 2012*].

NPD real space data were processed by regrouping repeated scans of the D4c detectors over the available range of scattering angles in the reciprocal space. For each sample, empty container and sample environment contributions were subtracted from raw data, taking into account attenuation effects [*Howe et al., 1996*] as well as the incoherent-scattering contribution. A standard multiple-scattering [*Howe et al., 1996*] and Placzek [*Yarnell et al., 1973*] corrections were applied.

The first step in PDF data analysis is the so-called direct analysis: after proper baseline subtraction, a Gaussian function is fitted against each G(*r*) peak of interest in order to determined its peak position, its width and its area. Note that this is an approximation, since in principle a Gaussian function should be convolved with a *sinc* function, as described above.

As to modeling, it is performed with the "Real Space Rietveld" method [*Egami and Billinge, 2003*] featured by the software PDFGUI [*Farrow et al., 2007*]. As done with the Rietveld method in the reciprocal space analysis section, some parameters of a structural model are refined against the experimental G(*r*) curve. The quality of the fit is defined by the agreement factor:

$$R_w = \left[\frac{\sum_{i=1,n}^{n} \omega(r_i)[G_{obs}(r_i) - G_{calc}(r_i)]^2}{\sum_{i=1,n}^{n} \omega(r_i) G_{obs}^2(r_i)}\right]^{\frac{1}{2}} \quad (2.30)$$

where $\omega(r_i) = 1/\sigma^2(r_i)$ and $\sigma(r_i)$ is the standard deviation.

References

[*Allieta, 2012*] M. Allieta, PhD Thesis, 2012, Università degli Studi di Milano.

[*Allieta et al., 2011*] M. Allieta, M. Brunelli, M. Coduri, M. Scavini and C. Ferrero. *Z. Kristallogr. Proc.* 2011, **1**, 15-20.

[*Anderson and Cox, 1993*] M. P. Anderson and D. E. Cox, *Solid State Ionics* 1983, **9 & 10**, 953-960.

[*Argyriou, 1994*] D. N. Argyriou, *J. Appl. Cryst.* 1994, **27**, 155-158.

[*Billinge and Farrow, 2012*] S. J. L. Billinge and C. L. Farrow, 2012, arXiv:1211.4284.

[*Blessing, 1995*] R. H. Blessing, *Acta Cryst* 1995, **B51**, 816-823.

[*Brennan and Cowan, 1992*] S. Brennan and P. L. Cowan, *Rev. Sci. Instrum.* 1992, **63**, 850.

[*Dwiggins and Park, 1971*] C. W. Dwiggins and D. A. Park, Calculation of the intensity od secondary scattering of -tays by non crystalline materials. *Acta Cryst.* 1971, **A27**, 264.

[*Egami 2004*] T. Egami, *Z. Kristallogr*. 2004, **219**, 122–129.

[*Egami and Billinge, 2003*] T. Egami and S. J. L. Billinge in *Underneath the Bragg peaks,* 2003, Pergamon.

[*Farrow et al., 2007*] C. L. Farrow, P. Juhàs, J. W. Liu, D. Bryndin, E. S. Bozin, J. Bloch, T. Proffen and S. J. L. Billinge, *J. Phys.: Condens. Matter* 2007, **19**, 335219.

[*Finger et al., 1994*] L. W. Finger, D. E. Cox and A. P. Jephcoat: *J. Appl. Cryst*. 1994, **27**, 892-900.

[*Fischer et al. 2006*] H. E. Fischer, A. C. Barnes and P. S. Salmon, *Rep. Prog. Phys.* 2006, **69**, 233–299.

[*Giacovazzo et al., 2002*] C. Giacovazzo, H. L. Monaco, D. Viterbo, F. Scordari, G. Gilli, G. Zanotti and M. Catti, in *Foundamentals of Crystallography*, 2002, Oxford University Press. See chapter 3.

[*Howe et al., 1996*] M. A. Howe, R. L. McGreevy and P. Zetterstrom, 1996, NFL Studsvik internal report.

[*Jeong et al., 1999*] I.-K. Jeong, T. Proffen, F. Mohiuddin-Jacobs and S. J. L. Billinge, *J. Phys. Chem. A* 1999, **103**, 921-924.

[*Keen01*] D. A. Keen, J. Appl. Cryst. 2001, **34**, 172-177.

[*Kodama et al., 2006*] K. Kodama, S. Iikubo, T. Taguchi and S.-I. Shamoto, *Acta Cryst.* 2006, **A62**, 444–453.

[*Larson and Von Dreele, 2004*] A. C. Larson and R. B. Von Dreele *General Structural Analysis System (GSAS)*; Los Alamos National Laboratory Report LAUR, 2004, 86-748.

[*Lobanov and Alte da Veiga, 1998*] N. N. Lobanov and L. Alte da Veiga, *6th European Powder Diffraction Conference*, 1998, Abstract P12-16.

[*Lorch, 1969*] E. Lorch, *J. Phys. C* 1969, **2**, 229-237.

[*Louca et al. 1999*] D. Louca, G. H. Kwei, B. Dabrowski and Z. Bukowski, *Phys Rew. B* 1999, **60**, 7558.

[*Mittemeijer and Scardi, 2004*] E. J. Mittemeijer and P. Scard in *Diffraction Analysis of the Microstructure of Materials*, 2004, Springer.

[*Neder and Proffen, 2009*] R. B. Neder and T. Proffen, in *Diffuse scattering and defect structure simulations: a cook book using the program DISCUS*, 2009, Oxford University Press.

[*Peterson et al., 2003*] P. F. Peterson, E. S. Bozin, T. Proffen and S. J. L. Billinge, *J. Appl. Cryst.* 2003, **36**, 53-64.

[*Plackek 1952*] G. Placzek, *Phys Rev. B* 1952, **86**, 377.

[*Qiu et al., 2004*] X. Qiu, E. S. Bozin, P. Juhas, T. Proffen and S. J. L. Billinge, *J. Appl. Cryst.* 2004, **37**, 110-116.

[*Qiu04 et Al., 2004b*] X. Qiu, J. W. Thompson and S. J. L. Billinge, *J. Appl. Cryst.* 2004, **37**, 678.

[*Rietveld, 1967*] H. M. Rietveld, *J. Appl. Crystallogr.* 1969, **2**, 65-71.

[*Sears, 2006*] V. F. Sears, *Neutron News* 1992, **3**, 26-37.

[*Snyder et al., 1999*] R. L. Snyder, J. Fiala and H. J. Bunge in *Defect and Microstructure Analysis by Diffraction*, 1999, Oxford University Press.

[*Stout and Jensen, 1989*] G. H. Stout and L. H. Jensen, in *X-ray Structure Determination: A Practical Guide*, 1989, Wiley Interscience.

[*Svab and Hajdu, 1992*] E. Svab and F. Hajdu, *J. Appl. Cryst.* 1994, **27**, 25-28.

[*Toby and Egami 1992*] B. H. Toby and T. Egami, *Acta cryst.* 1992, **A48**, 336-346.

[*Thompson et al., 1997*] P. Thompson, D. E. Cox and J. B. Hastings, *J. Appl. Cryst.* 1987, **20**, 79-83.

[*Toby, 2001*] B. H. Toby. *J. Appl. Crystallogr*,. 2001, **34**, 210-214.

[*Waasmeier and Kirfel, 1995*] D. Waasmaier and A. Kirfel, *Acta Cryst.* 1995, **A51**, 416-431.

[*Yarnell et al., 1973*] J. L. Yarnell, M. J. Katz, R. G. Wenzel and S. H. Koenig, Phys. Rev. 1973, **A7**, 2130-2144.

[*Young 1993*] R. A. Young in *The Rietveld method*, 1993, Oxford University Press.

3. Experimental Section

3.1. Synthesis

Except when explicitly indicated, all the investigated samples were prepared following the Pechini sol-gel method. Cerium nitrate, $Ce(NO_3)_3 \cdot 6H_2O$ (Aldrich 99%) and *RE* (=Gd, Sm, Y, Yb, Tb, Nd, La) dopant nitrate $RE(NO_3)_3 \cdot XH_2O$ (X = 5 or 6 depending on *RE*) (Aldrich 99.9%) were used as precursors in stoichiometric ratio, while ethylene glycol (Aldrich ≥99%) and citric acid (Aldrich 99%) were added as polymerization agents for the process. The gel was burned in an ashing furnace (Nabertherm), heated with a 3 °C/min ramp up to 500 °C, and then held at the same temperature for 3 hours. The powder was then pressed into pellets and fired at 900 °C for 72 h in air.

The samples were named after the $Ce_{1-x}RE_xO_{2-x/2}$ formula.

Pure oxides (Gd_2O_3, 99.8%, Y_2O_3, 99.99%) were purchased by Aldrich. Sm_2O_3 was instead prepared after the above mentioned sol gel route, using only $Sm(NO_3)_3 \cdot 6H_2O$ as metal precursor. Two different samples were prepared, firing the pellets at 700°C (Sm_2O_3c) and 900°C (Sm_2O_3m).

3.2. Instruments

In this section the instruments employed for collecting powder diffraction data are briefly described. Instead of giving tedious technical details which can be found elsewhere [*Fitch, 2004, Hansen et al., 2008, Fischer et al., 2002*], the goal of this section is to provide the reader with the basics capabilities of each beamline/instrument, with reference to the kind of data analysis (reciprocal space, PDF or both) that can be performed and relative advantages and drawbacks. This should help the comprehension of the data analysis in the next chapters. In the following we will refer to "Rietveld analysis" with reference to the reciprocal space approach defined in section 2.1.

3.2.1. X-Ray Powder Diffraction

3.2.1.1. ID31

The ID31 diffractometer works in a Debye-Scherrer geometry. The powdered samples are loaded in a glass, or kapton capillary, mounted on the axis of the diffractometer and spun to improve powder

randomization. A bank of nine detectors approximately 2° apart is scanned to measure the diffracted intensity as a function of 2theta. Usually the contribution of two or three detectors is neglected to remove aberrations such as cross talkings. ID31 is considered the high resolution beamline of the ESRF. High resolution means that the broadening of a diffracted peak due to the instrument is very low, in the case of ID31 in the order of ~0.003°. This makes ID31 particularly apt to Rietveld analysis: the peak overlap is extremely reduced and it is possible to detect peak splits otherwise impossible to resolve with a lab diffractometer. Moreover, high quality data enable the accurate determination of thermal parameters, even anisotropic. In the case of doped ceria compounds, this is particularly true for cations. The high resolution facilitates the study of the microstructure, which is determined by the broadening of a diffraction peak. A limited angular resolution is reflected in the real space as the damping of PDF oscillations with increasing *r*-interatomic distance (see section 2.2). Thus at ID31 it is possible to study the real space arrangement of atoms over a wide *r*-range. For example, the estimate of the extent of disorder in a crystalline material is made possible. The main drawback of using point detectors, even though in a stripe, is the long collection time required to get reliable data. For a Rietveld analysis one hour is usually enough to gather high quality data. For PDF analysis, longer collection times are required, basically to improve the statistic significance at high wavevector *Q* values, where the diffracted intensity is very low. A PDF quality pattern is attained merging several scans, the most of them performed in the high 2theta region. Thus, a XRPD pattern for PDF collected at ID31 is also a Rietveld quality pattern.

Finally, a remark on the sample environment. A blower gas stream (cryostream) is used to control the temperature. Being nothing else than a blow of air or nitrogen, it is an ideal sample environment because it does not affect the diffracted intensity. Conversely, the use of a more complex device such a cryostat, which requires the sample to be moved inside a metallic cage, contributes to the diffracted intensity making more difficult the background subtraction for PDF analysis. The lowest temperature which can be safety reached and controlled with a cryostream device is ~90 K. Since a low temperature was chosen to minimize thermal motion, this is one of the reasons why we chose T = 90 K for PDF analysis. Moreover, as shown in chapter 5, the amplitude of vibration does not further reduce below this temperature, thus lower temperatures are not required.

3.2.1.2. ID11

ID11 is a very versatile beamline. We used the diffractometer in a Debye Scherrer geometry, with a non ambient condition sample environment, described in the experimental section of chapter 6.

The powdered sample is loaded in a capillary, in our case a quartz capillary for high temperature measurements. The diffracted intensity is recorded by a CCD FReLoN (Fast Readout Low Noise) camera placed perpendicular to the beam at a certain distance behind the sample. The extremely high incident flux of ID11, coupled to the use of a CCD camera, enables the very fast acquisition of diffraction patterns, even for PDF analysis. This is particularly suitable for temperature evolution or time resolved studies.

The angular resolution can be tuned by acting on the sample to detector distance: by placing the camera far away from the sample, the resolution is increased at the expense of the maximum 2theta, that is Q_{max}. In this way a Rietveld quality pattern is obtained. On the other hand, if one wants to collect data for PDF analysis, he will prefer to move the camera close to the sample, at the expense of the angular resolution. In this way, data up to Q_{max} ~30 $Å^{-1}$ can be readily recorded in few seconds acquisition times.

The sample-to-detector distance is calibrated using a standard material, the *d*-space values of which are known with accuracy. Once the distance and other parameters, such as camera tilting and rotation as well as the coordinates of the beam center are defined, the recorded frames can be converted into conventional intensity against 2theta patterns. Thus the optimal strategy to combine Rietveld and PDF data collection is to record patterns at different sample to detector distances. Unfortunately, the movement of the CCD camera is not perfectly reproducible. Every time the camera is moved, the distance should be calibrated. Since a correct calibration is sometimes hard to obtain, a further correction to be performed directly in the real space is proposed in chapter 6.

In conclusion: the use of a 2D detector makes faster the data analysis at the expense of the accuracy of the collected data. Moreover, it is difficult to extract reliable standard deviation, thus making troublesome the interpretation of the results.

3.2.2. Neutron Powder Diffraction

3.2.2.1. D20

D20 is a high flux instrument at ILL. It is equipped with a large microstrip detector, covering a 2theta range from ~10 to ~140°. The detector bank does not move during the acquisition, thus the angular resolution is limited by the distance between two adjacent cells containing the detectors. The sample is loaded in a vanadium can, typically some cm long and less than 1 cm wide. The D20 instrument is suitable for reciprocal space data collection, but the relatively low energy of incident neutron do not enable PDF studies. The main advantage in using the D20 instrument is given by the very high incident flux, which makes it particularly suitable for time resolved or temperature evolution studies. We used the D20 instrument for the latter goal. Using a cryostat we collected data from RT down to 4 K, whilst using a furnace we collected data from RT up to ~800°C. In order to accurate determine thermal parameters the longest data acquisitions lasted 15-30 minutes.

3.2.2.2. D4c

D4c is the amorphous and liquids diffractometer of ILL. The powdered sample is loaded in a vanadium can of known dimension, in our case generally 6 cm high by 0.75 cm wide. The packing fraction should be accurately measured for proper corrections. The scattered intensity is recorded by a detector made of nine banks, each containing 64 cells. During the measurement the banks move to improve statistics, thus obtaining a complete powder diffraction pattern from 1.5 to 140° 2theta. Being the incident wavelength fixed to ~0.5 Å, the maximum Q value obtainable at D4c is ~23.6 $Å^{-1}$. The D4c is apt to perform PDF data collection, whilst we did not use if for Rietveld analysis, owing to its lower resolution compared to D20.

The high incident flux allows to collect reliable PDF in 3-4 hours collection time, depending on the element scattering cross sections. The backgrounds (empty cryostat, empty can, vanadium rod) should be periodically measured during the experiment to check for stability.

3.3.Data collection

The samples reported in the present thesis were subjected to a number of different XRPD and NPD experiments. X-ray synchrotron radiation data were collected at the ID31 and ID11 beamlines of the

European Synchrotron Radiation Facility (ESRF, Grenoble, France), whereas NPD data were collected at the D20 and D4c instruments of the Institut Laue Langevin (ILL, Grenoble, France).

Apart the in-situ measurements shown in chapter 6, all the PDF data, using either X-rays (ID31) or neutron (D4c), were collected at T = 90 K in order to minimize thermal motion. NPD data for Rietveld analysis were also collected in the 4 K < T < RT range.

Here follows the list of the experiments performed on the samples of interest for this thesis. Temperature and incident wavelength are indicated for each experiment.

- April 2009, experiment ch2907 at ID31. T = 90 K

λ_1=0.3096 Å: PDF data collection on CeO_2, x(Gd)=0.125, 0.250, 0.500, 0.750, 0.875 and Gd_2O_3.

- July 2010 and May 2011, experiment 5-23-605 at D20 and D4c.

λ_1=1.3593 Å ad D20, 4 K < T < RT. Rietveld data collection on CeO_2, Y_2O_3, x(Y)=0.125, 0.250, 0.500.

λ_2=0.4975 Å ad D4c, T = 90 K. PDF data collection on CeO_2, Y_2O_3, x(Y)=0.125, 0.250, 0.500, x(La)=0.25, 0.50

- November 2010, experiments CH3250/CH3251 at ID31, T = 90 K.

λ_1=0.3099 Å: PDF data collection on CeO_2, Y_2O_3, Sm_2O_3c, Sm2O3m, x(Sm)=0.125, 0.250, 0.500, 0.750, x(Y)=0.125, 0.250, 0.500, 0.750, 0.875.

Only Rietveld data collection on x(Sm)=0.3125, 0.375, 0.40625, 0.4375, 0.5625, 0.625, 0.6875, 0.8125, 0.875, 0.9375, x(Y)=0.375 .

- April 2011, experiment CH3366 at ID31, T = 90 K.

λ_1=0.3541 Å: PDF data collection on x(La)=0.25, x(Nd)=0.25, x(Yb)=0.25, x(Tb)=0.25, x(Y)=0.25, 0.3125, 0.34375, 0.4375; x(Sm)=0.3125, 0.34375, 0.375, 0.4375, 0.625; x(Gd)= 0.3125, 0.34375, 0.375, 0.4375.

Only Rietveld data collection on CeO_2.

- August and December 2011, experiment 5-26-198 at D20 and D4c.

λ_1=1.3593 Å and D20, 4 K < T < RT. Rietveld data collection on CeO_2, x(La)=0.125,0.250, 0.375, 0.500; x(Nd)=0.125,0.250, 0.375, 0.500; x(Yb)=0.125,0.250, 0.375, 0.500; x(Tb)=0.125,0.250, 0.375, 0.500; x(Y)=0.375.

λ_2=0.4974 Å and D4c, *T* = 90 K. PDF data collection on CeO_2, *x*(La)= 0.375; *x*(Nd)=0.250, 0.375, 0.500; *x*(Tb)= 0.125, 0.250, *x*(Yb)= 0.250, 0.375, 0.500.

λ_3=0.4969 Å and D4c, *T* = 90 K. PDF data collection on CeO_2, *x*(La)= 0.125; *x*(Nd)=0.125; *x*(Tb)= 0.375, 0.500, *x*(Yb)= 0.125.

- July 2012, experiment ch3401 at ID11, from RT to *T* = 750 °C.

Data collected under static air and under a H_2(7%)/Ar mixture on CeO_2 and a *x*(La)=0.25 sample at incident wavelength λ=0.1232 Å.

- October 2012, experiment 5-26-210 at D20 and D4c.

λ_1=1.3593 Å and D20, RT < *T* < 800 °C. Rietveld data collection on CeO_2, *x*(La)=0.250.

Since samples sharing the same kind and amount of dopant were measured during different experiments, it could be difficult for the reader to have an overview of all the samples investigated. In order to try to make things clearer, the instrument and wavelength for each of the investigated samples are summed up in Table 3.1 and will be recalled in the following chapters when discussing the corresponding results.

Table 3.1. Instrument and wavelength corresponding to all the samples investigated during the present thesis. PDF measurements are indicated in bold. The wavelength of the D20 instrument is not indicated since it was always the same: 1.3593 Å.

x(RE)	***x**16**	***La***	***Nd***	***Sm***	***Gd***	***Tb***	***Y***	***Yb***
0.125	2	D20 D4 **0.4969**	D20 D4 **0.4969**	ID31 **0.3099**	ID31 **0.3096**	D20 D4 **0.4974**	D20 ID31 **0.3099** D4 **0.4975**	D20 D4 **0.4969**
0.250	4	ID31 **0.3541** ID11 **0.1232** D20 D4 **0.4975**	ID31 **0.3541** D20 D4 **0.4974**	ID31 **0.3099**	ID31 **0.3096**	ID31 **0.3541** D20 D4 **0.4974**	ID31 **0.3542** **0.3099** D20 D4 **0.4975**	ID31 **0.35412** D20 D4 **0.4974**
0.3125	5			ID31 0.3099 **0.3541**	ID31 **0.3541**		ID31 **0.3541** D20	
0.34375	5.5			ID31 **0.3541**	ID31 **0.3541**		ID31 **0.3541**	
0.375	6	D20 D4 **0.4974**	D20 D4 **0.4974**	ID31 0.3099 **0.3541**	ID31 **0.3541**	D20 D4 **0.4969**	ID31 0.3099 D20 D4 **0.4969**	D20 D4 **0.4974**
0.40625	6.5			ID31 0.3099				
0.4375	7			ID31 0.3099 **0.3541**	ID31 **0.3541**		ID31 **0.3541**	
0.500	8	D20 D4 **0.4975**	D20 D4 **0.4974**	ID31 **0.3099**	ID31 **0.3096**	D20 D4 **0.4969**	ID31 **0.3099** D20 D4 **0.4975**	D20 D4 **0.4974**
0.5625	9			ID31 0.3099				
0.625	10			ID31 0.3099 **0.3541**				
0.6875	11			ID31 0.3099				
0.750	12			ID31 **0.3099**	ID31 **0.3096**		ID31 **0.3099**	
0.8125	13			ID31 0.3099				
0.875	14			ID31 0.3099	ID31 **0.3096**		ID31 **0.3099**	
0.9375	15			ID31 0.3099				
1	16			ID31 **0.3099**	ID31 **0.3096**		ID31 **0.3099** D4 **0.4975** D20	

References

[*Fischer et al., 2002*] H. E. Fischer, G.J. Cuello, P. Palleau, D. Feltin, A. C. Barnes, Y. S. Badyal and J. M. Simonson, *Appl. Phys.* 2002, **A74**, S160-S162.

[*Fitch, 2004*] A. N. Fitch, *J. Res. Natl. Inst. Stand. Technol.* 2004, **109**, 133-142.

[*Hansen et al., 2008*] T. C. Hansen, P. F. Henry, H. E. Fischer, J. Torregrossa and P. Convert, *Meas. Sci. Technol.* 2008, **19**, 034001.

4. CeO_2-RE_2O_3 solid solutions. The case of Sm, Gd and Y doping.

4.1. Introduction

Since the amount of oxygen vacancies through which O ions can migrate is determined by the dopant concentration, ionic conductivity in doped ceria is expected to continuously increase with doping. A maximum is to be expected when half of the oxygen sites are vacant [*Kilner, 2000*], but it is generally found to happen at much lower doping concentration.

Among all the possible trivalent cations, Gd, Sm and Y are considered the most promising dopants for ceria, since they guarantee the highest performance [*Balasz and Glass, 1995*]. Although it is clear the transport properties are dominated by short range atomic interactions, an exhaustive crystallographic description of the local scale in doped ceria is still lacking. For example, literature reports do not agree about the effective Y coordination numbers in x(Y)=0.20 doped samples: different authors found out N(Y-O)~6 **[***Wang et al., 2006***]**, ~6.5 [*Deguchi et al., 2005*] and ~7 **[***Kim and Stebbins, 2007***]**, employing EXAFS and Y^{89} MAS NMR spectroscopy. Also controversial is the actual magnitude of the 1st neighbour M-O distance: (for M we consider the metal ions, either Ce or *RE*) EXAFS **[***Deguchi et al., 2005***]** and MD simulations **[***Hayashi et al., 2000***]** probed shorter Y-O pairs then Ce-O, whereas shorter Ce-O were suggested by a Monte Carlo study [*Burbano et al., 2012*]. It seems evident that *RE* and Ce cations have a different chemical environment, although they share the same average structure. Electron microscopy studies suggested that for Gd, Sm and Y the peak in ionic conductivity is due to the spread of *RE*-rich nanodomains which trap oxygen vacancies [*Ou et al., 2008, Ye et al., 2009b, Ou et al., 2006a*]. Larger nanodomains result in a reduced amount of free oxygen vacancies, thus a decrease in ionic conductivity. The extent of disorder is then expected to increase with doping.

In this chapter, we propose to investigate the CeO_2-RE_2O_3 (*RE*=Sm, Y, Gd) systems employing high resolution XRPD performed at low temperature in order to minimize thermal motion. Further details are given in the experimental section. We decided not to limit the investigation to low doping amount, but to

consider the whole system from CeO_2 to RE_2O_3. We indeed retain that the evolution of the structure as a function of the dopant concentration could provide a more complete information than the study of the only dilute systems. In highly doped samples indeed the magnitude of disorder is expected to increase and could, in principle, be better understood.

Part of the work presented in this chapter was published in [*Scavini et al., 2012*].

4.2. Experimental section

All XRPD patterns were recorded at the ID31 beamline of the ESRF on a number of samples, reported below. Except when explicitly indicated, the below data were collected for PDF analysis. We recall here that a PDF data collection at ID31 is performed by summing different scans, recording for much longer times the intensity at high angle to increase statistic significance. Conversely, to get reliable data for Rietveld analysis one scan is usually enough. A PDF data collection thus involves the recording of high quality data for reciprocal space analysis. The results reported in the present chapter refer to three different data collections, all performed at T = 90 K. During each experiment, the empty capillary was measured in the same Q range in order to properly subtract the background for PDF analysis.

Here follows the list of the experimental conditions related to all the samples investigated in this chapter.

The Q_{max} reported below correspond to the highest 2θ value recorded. The actual Q_{max} employed for processing PDF was reduced to Q_{max}=28 Å^{-1} i) to increase the signal to noise ratio and ii) for sake of comparison. As a consequence, the list below is shown for sake of completeness, but in principle all data can be comparable since for PDF analysis they were truncated at the same Q_{max} value.

- The samples x(Gd) = 0.125, 0.250, 0.500, 0.750, 0.875 and Gd_2O_3 were investigated at λ = 0.3096 Å in the angular range $0 < 2\theta < 100°$, covering a wave-vector Q region up to Q_{max} ~ 31 Å^{-1}. Measurements lasted about 8 hours for each sample. Glass capillaries (1.0 mm diameter) were used.

- The samples x(Sm) = 0.125, 0.250, 0.500, 0.750, Sm2O3m and Sm_2O_3c; x(Y) = 0.125, 0.250, 0.500, 0.750, 0.875, Y_2O_3 and CeO_2 were investigated at λ = 0.3099 Å in the angular range $0 < 2\theta < 100°$, up to Q_{max} ~ 31 Å^{-1}. Measurements lasted about 9 hours for each sample. Additional fast scans only for Rietveld analysis were collected at λ=0.3099 on x(Sm)=0.3125, 0.375, 0.40625, 0.4375, 0.5625, 0.625, 0.6875, 0.8125, 0.875, 0.9375; x(Y) = 0.375. Kapton capillaries (1.0 mm diameters) were used.

- The x(Y)=0.25, 0.3125, 0.34375, 0.4375, 0.50, x(Sm)=0.3125, 0.34375, 0.375, 0.4375, 0.625, x(Gd)= 0.3125, 0.34375, 0.375, 0.4375 were investigated at λ = 0.3541 Å in the angular range $0 < 2\theta < 120°$, up to Q_{max} ~ 29.4 $Å^{-1}$. Measurements lasted about 3-4 hours for each sample. Kapton capillaries (1.0 mm diameter) were used.

4.3.Reciprocal space analysis

A single phase, either fluorite or C-type, is observed over the whole compositional range of the solid solutions for *RE*=Y and Gd, whilst for *RE* = Sm a biphasic system (B+C) is observed for x(Sm) $\geq$ 0.875. As for pure Sm_2O_3, when sintered at T = 900°C it was observed to be in its pure monoclinic form (Sm_2O_3m), whereas when annealed at T = 700°C, a pure C-type phase was obtained. In the following only the latter is considered.

The use of high resolution XRPD data allows us to exclude the presence of biphasic systems when increasing the doping amount from fluorite to C-type structure, as reported in literature (see e.g. [*Chavan and Tyagi, 2005*]. Instead of a biphasic system, we observed a C-type phase having broader superstructures peaks. The corresponding compositional range is defined as the C* region and is thoroughly described in section 4.3.1.3. Note that the samples in the C* region exhibit a pure crystallographic C-type structure. The distinction between C* and C is done to facilitate comparisons among samples having broaden superstructure peaks, but no crystallographic transition occurs from C* and C-type.

The results of the Rietveld refinements for all the investigated samples are reported in the Appendix, A4.1.

4.3.1. The cell parameter

In order to facilitate comparisons, here we define a_f as the fluorite cell parameter and as the halved C-type cell parameter. The a_f cell parameters for *RE*=Y, Gd and Sm are plotted in Fig. 4.1 (*a*), (*b*) and (*c*), respectively. Dotted lines are guides to the eye to indicate a vegardian behavior of the solid solution. Y- and Sm-doped ceria cell parameter trends feature a similar, though opposite, behavior, consistent with the different ionic radii of the dopant[*], compared to Ce^{+4}. At large Sm doping concentration, the cell parameter

[*] ionic radii based on data reported by Shennon: 0.97 Å for Ce^{+4}(VIII), 0.96 Å for Y^{+3}(VII), 1.00 Å for Gd^{+3}(VII) and 1.02 Å for Sm^{+3}(VII).

remains nearly constant, according to the coexistence with the monoclinic phase. Something different is observed in case of Gd-doped ceria. Although Gd_2O_3 has a smaller a_f cell parameter than pure CeO_2, the cell expands upon Gd-doping up to x~0.45, then shrinks again to Gd_2O_3. Such strong non-vegardianity is explained by Nakamura [*Nakamura, 2010*] in terms of non random *RE* - oxygen vacancies distributions, with Ce and *RE* having different coordination numbers with respect to O ions.

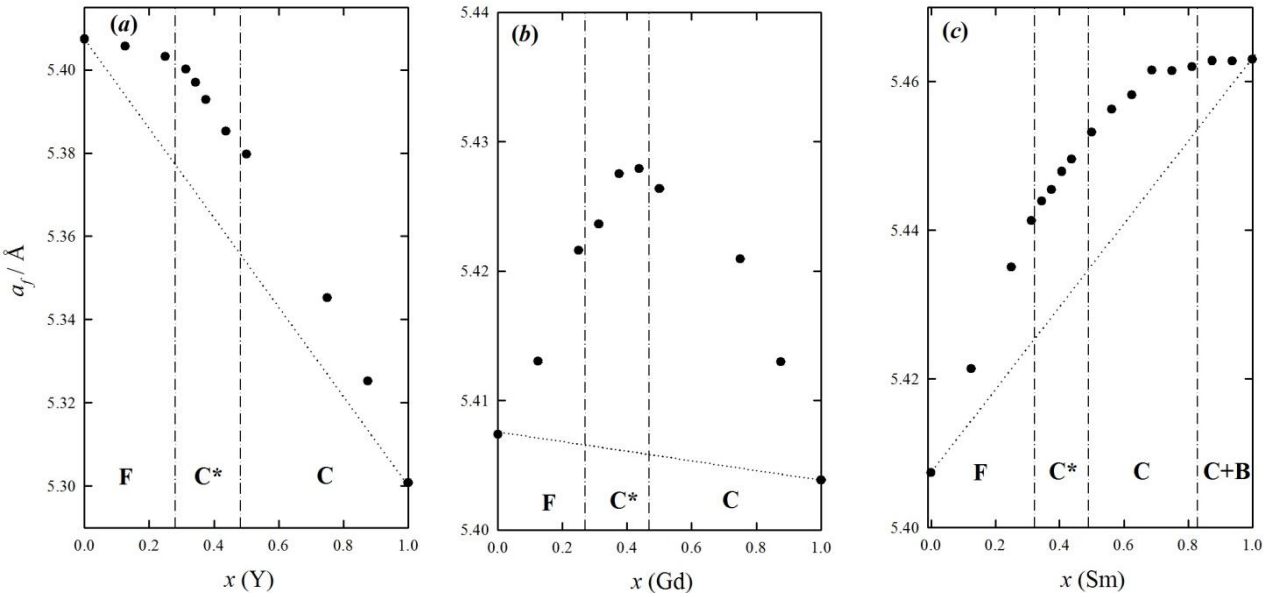

Fig. 4.1. a_f cell parameter (see main text) along the whole solid solutions of CeO_2-Y_2O_3 (*a*) -Gd_2O_3 (*b*) and -Sm_2O_3 (*c*).

4.3.2. The *x*(M2) coordinate

Here we remind the reader that the *x*(*RE*2) coordinate is the only metal positional degree of freedom of cations in a C-type structure. *x*(*RE*2) was introduced in section 1.5.2.1 with reference to a pure RE_2O_3 sesquioxide. Now we refer to *x*(M2) since in the solid solution this site is occupied by Ce and *RE* in due proportions. This structural parameter determines the M-M distances distribution. When *x*(M2) = 0, the cation distribution is the same as in fluorite and a single M-M distance occurs. When *x*(M2) ≠ 0, two sets of different M-M distances are present. This is triggered by the presence of oxygen vacancies in between the two cations. The *x* coordinates of the M2 site in the C-type structure are reported for *RE*=Y, Gd and Sm in Fig. 4.2 (*a*), (*b*) and (*c*), respectively.

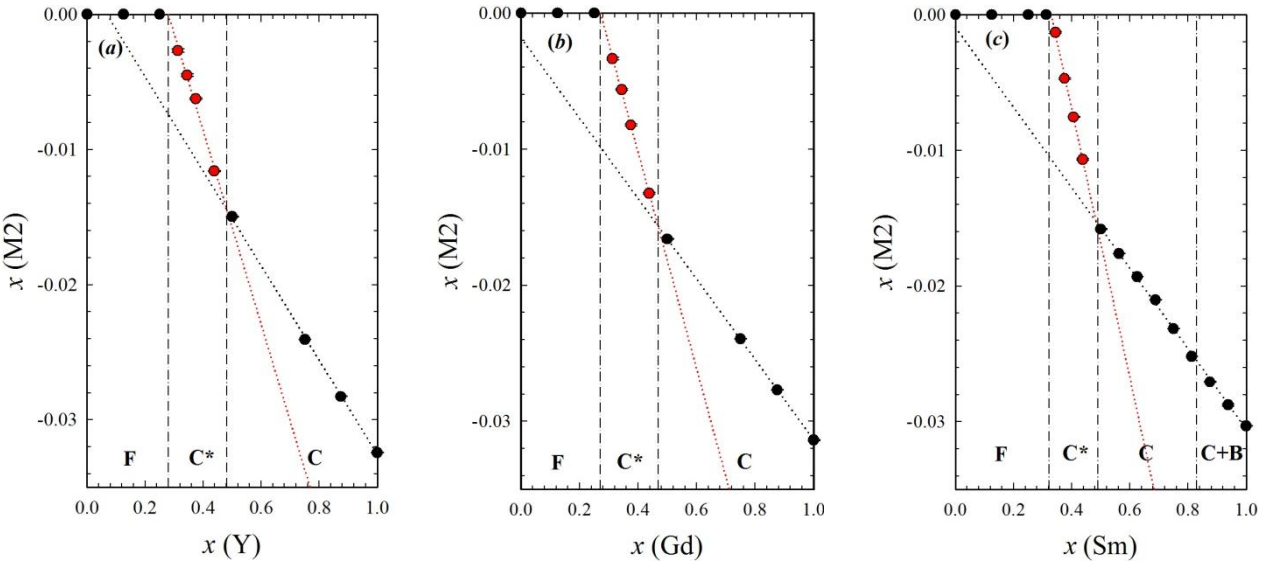

Fig. 4.2. *x*(M2) coordinate as determined from Rietveld refinements for Y (*a*), Gd (*b*) and Sm (*c*) doping.

A similar trend is observed for the three dopants: by adding Ce to pure RE_2O_3, *x*(*RE*2) increases linearly. A steep increase is observed in the C* region, depicted in red in Fig. 4.2. The dotted lines are the linear regressions of the two trends. The *x* coordinate of the interception of the two regressions was used to establish the boundary between C* and C-type regions. In the same way, the solubility limit of the *RE* dopant in the fluorite structure is determined by the interception with the *x* axis of the *x*(M2) trend in the C* region. The following *RE* solubility in CeO_2 were determined: *x*(Y) = 0.28, *x*(Gd) = 0.27 and *x*(Sm) = 0.32.

In spite of its very linear trends, the *x*(M2) behavior at high Sm doping rates remains unclear. As discussed in the former section, in the most doped samples the C-type phase coexists with the B-type. One could conceive that part of Sm ions are "trapped" into the B-type structure. To support this finding, the C-type cell parameter is nearly constant with doping in this region (see Fig. 4.1). If less Sm ions enter the C-type structure, then the number of oxygen vacancies introduced into the C-type structure is expected to be reduced. As a consequence *x*(M2) should not decrease with *RE* doping, as expected in a pure C-type structure. Somewhat at odds with the trend expected.

As discussed above, the *x*(M2) coordinate determines the M-M distance distribution. In Fig 4.3 the first two sets of metal-metal distances, to be taken as a reference for the PDF studies discussed below, are plotted for the three dopants. For sake of clearness, the ordinate scale in Fig. 4.3 is expanded above the break.

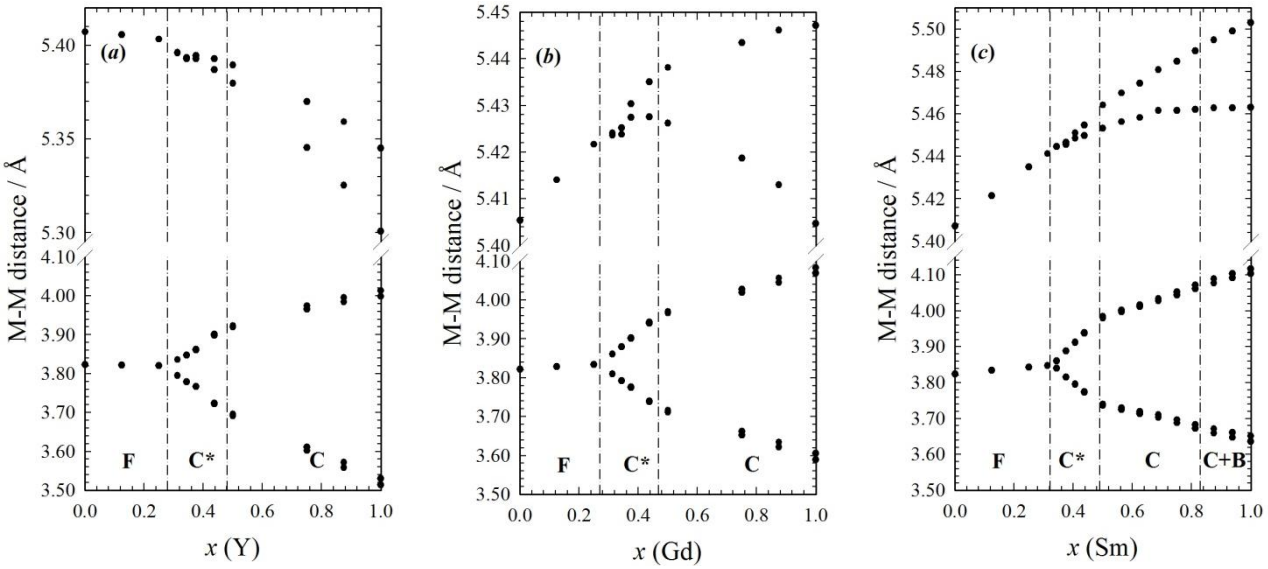

Fig. 4.3. M-M distances based on the results of Rietveld refinements for Y (*a*), Gd (*b*) and Sm (*c*) doping.

4.3.3. The C* region

The compositional range enclosed by dashed lines in Figs 4.1-4.3 is characterized by the anomalous broadening of C-type superstructure peaks. Fig. 4.4 (*left*) reports the observed 413 superstructure reflection (dotted line) together with the one calculated based on the structures' peaks profile (solid line) for different Y compositions. Just a strong diffuse scattering is observed for *x*(*RE*)=0.25. The same applies to Sm- and Gd-doped samples. In the right hand panel of Fig. 4.4 the 413 reflection is compared to the mean 222 peak in *x*(Y)=0.75, a sample not affected by superstructure peaks broadening.

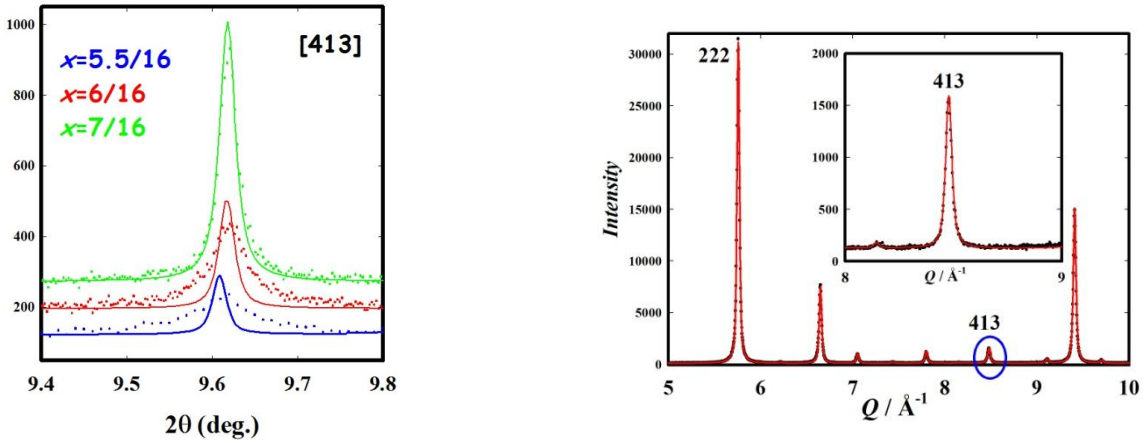

Fig 4.4. Left: observed (dotted lines) and calculated (solid lines) superstructure peaks, the latter based on the profile of structure peaks, for different Y-doping compositions. Similar results are observed for Gd- and Sm-doping. Right: comparison between the 413 reflection reported in the left panel and the 222 reflection, taken as a reference for normalizing FWHM. The pattern refers to *x*(Y)=0.75.

The anomalous broadening of the peaks can be treated quantitatively by determining their Full Width at Half Maximum (FWHM). The peaks were fitted with Pseudo-Voigt functions, as implemented in the software Winplotr [*Roisnel and Carvajal, 2001*]. The FWHM of the 413 reflection was then normalized to

the FWHM of the 222 reflection, taken as a reference. This is done to avoid that possible fluctuations of grain size with composition might affect the trend of the FWHM. The particle size indeed affects both structure and superstructure peaks.

The normalized FWHM (nFWHM) are plotted in Fig. 4.5. By taking the pure dopant oxide as a reference and adding Ce up to ~50% composition the peak broadening is not affected. The nFWHM steeply increases when reducing doping concentration (i.e. by increasing Ce) in the C* region.

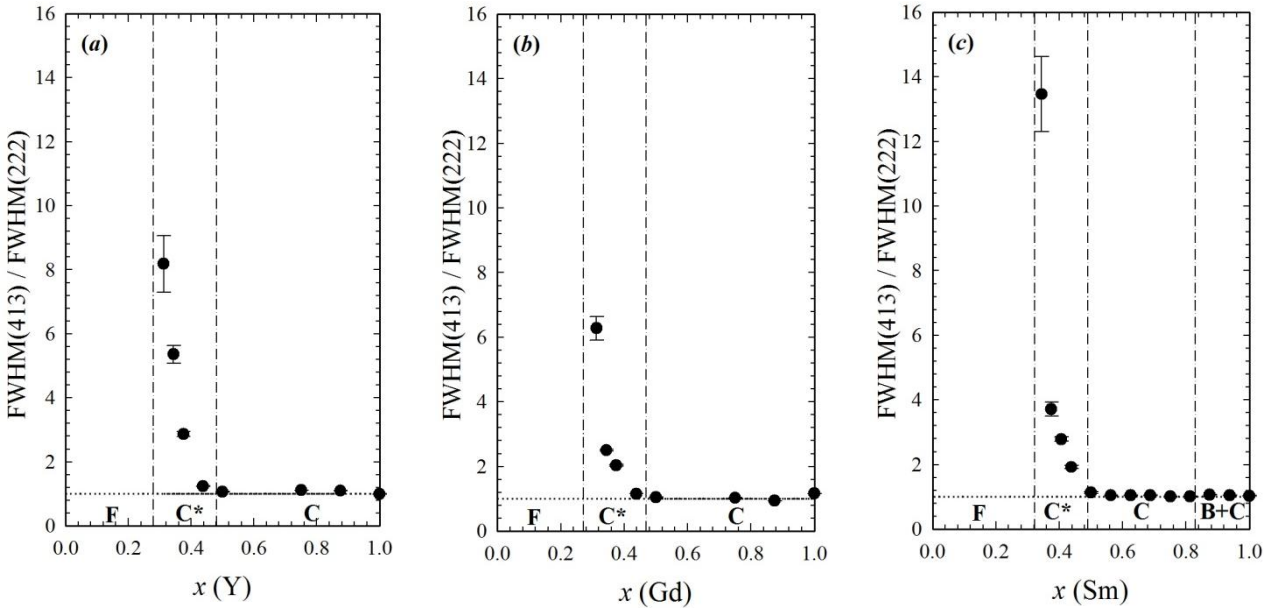

Fig. 4.5. nFWHM (see main text) for Y (*a*), Gd (*b*) and Sm (*c*) doping.

Note that the dashed lines in Fig. 4.5, which define the boundaries of the C* region, are taken from the trend of x(M2), as determined in Fig. 4.2. This means that the increasing peak broadening is accompanied by a continuous structural evolution, from C-type to fluorite. When the doping amount is further reduced, the average structure becomes fluorite and instead of superstructure peaks only diffuse scattering is observed.

The *hkl*-dependent broadening of superstructure peaks may have different origins which are [*Mittemeijer and Scardi, 2004*]: extended defects such as dislocations, antiphase boundaries, anisotropic particle size. Unfortunately, it was not possible to implement this modeling in Rietveld refinements. To overcome this problem, we exploit the Whole Powder Pattern Modeling (WPPM) approach implemented in the Pm2k software [*Leoni et al., 2006*]. Basically, the WPPM approach allows to discriminate the contributions of each broadening source based on their different broadening dependence on 2theta. We observed that the only way to fit the broaden superstructure peaks is to explicitly consider the presence of APB which are typically observed in alloys [*Scardi and Leoni, 2005*], but also in disordered oxides [*Moriga et al., 1989*]. The

software allows to try different models involving specific APB orientations, but none of them improved noteworthy the fit. We thus decided to consider a random distribution of APB as the origin of broad superstructure peaks. An example of a fit performed with Pm2k is shown in Fig. 4.6, with superstructure peaks magnified in the inset.

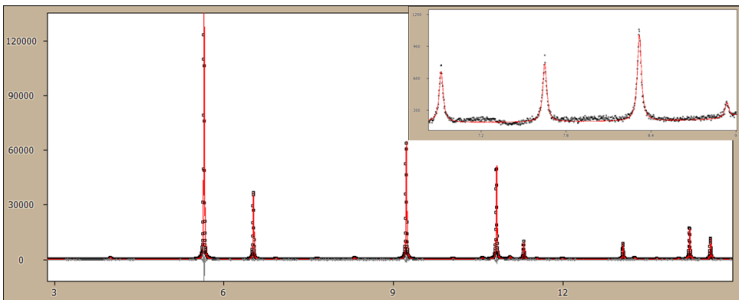

Fig. 4.6. Best fit performed using the WPPM approach on the *x*(Sm)=0.4375 sample. Superstructure peaks are highlighted in the inset.

4.3.4. The thermal parameters

As discussed in section 2.1, thermal parameters are a very sensitive tool for determining the presence of disorder. The doping induced disorder can be detected by monitoring the evolution of *msd* with doping. A first estimate about the spread of disorder with dopant concentration can be obtained by exploiting the overall intensity decay with 2theta. This is done in a Rietveld refinement by constraining all ions to the same *msd*, defined as U_{mean}. The U_{mean} values for *RE*=Y, Gd and Sm are plotted in Fig. 4.7 (*a*), (*b*) and (*c*), respectively.

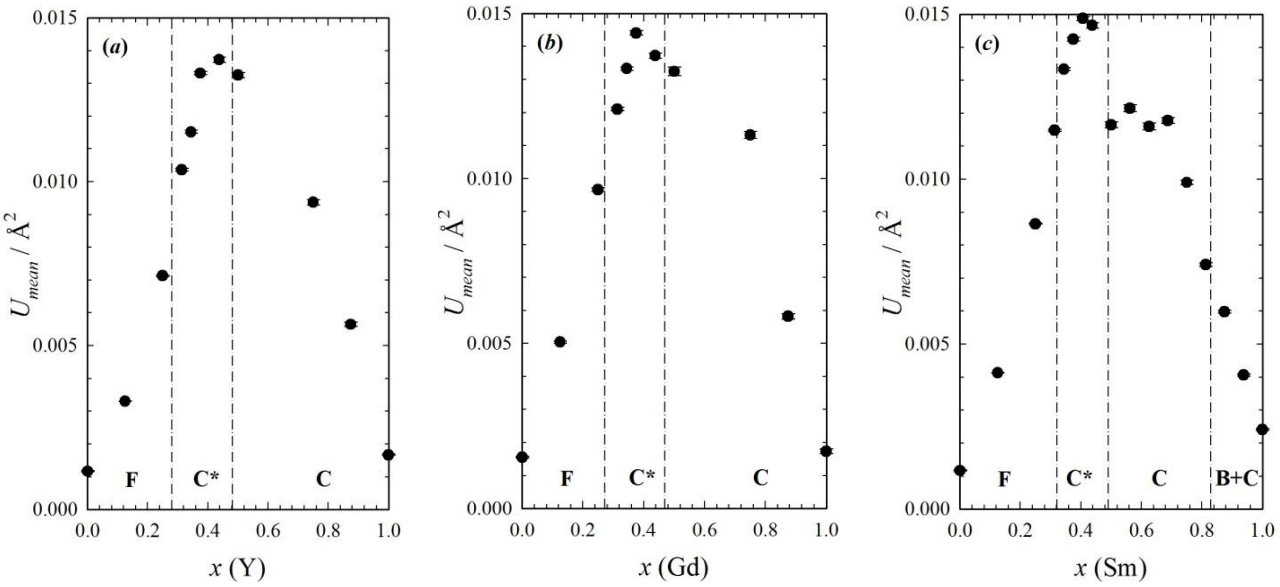

Fig. 4.7. Overall msd obtained by Rietveld refinements for Y (*a*), Gd (*b*) and Sm (*c*) doping.

The large increase of *msd* with doping is not consistent with the amplitude of vibration, but rather indicates the presence of static disorder. In the absence of disorder, at fixed temperature the *msd* is expected to be nearly constant with composition. In all cases the maximum disorder is observed in the C* region, at $x(RE)$~0.4. The U_{mean} does not provide any information about the spatial distribution of disorder. This can be gained by employing a different *msd* for each crystallographic site. This strategy, though, led to unphysical results when refining C-type structure parameters: negative O *msd* were obtained. This problem was overcome by considering anisotropic *msd* for cationic sites and the use of isotropic *msd* for the oxygen ions, i.e. the most light atoms, which less contribute to the scattered intensity.

As a consequence, a different approach is employed for each of the two structures under investigation. In fluorite, only the isotropic thermal parameter can be considered: the off-diagonal components of the *msd* tensor are fixed to zero and the diagonal ones are equal for symmetry constraints. In other words, no directional information can be gained by the study of the thermal parameter in fluorite, due to the high symmetry of the site involved.

This is not the case of the C-type structure. The refinement of the *anisotropic mean square displacements* (henceforth *Amsd*) for cations noteworthy improves the fit. This indicates that the disorder on M sites has a strong directional character.

As to O sites, *Amsd* were not implemented by reason of the low scattering length of O compared to those of cations.

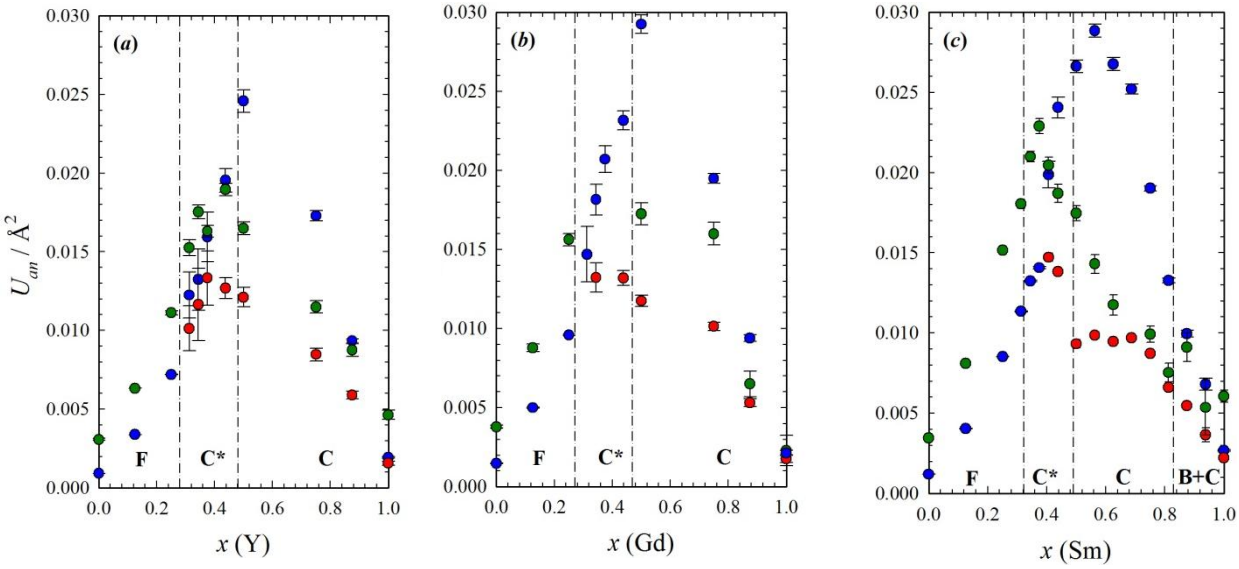

Fig. 4.8. *Uan* (see main text) for Y (*a*), Gd (*b*) and Sm (*c*) doping. Blue: M site in fluorite and M1 site in C-type; red: M2 site in C-type; green: O site in both fluorite and C-type.

The quadratic sum of the U11, U22, U33 components of the anisotropic tensor is here defined as U_{an}, which is reported in Fig. 4.8, together with the isotropic O *msd*. From Fig 4.8 it can be inferred that the most disordered site is the M1 in C-type. Moreover, the largest disorder on the M1 site occurs at larger doping amounts than M2 and O sites. The *Amsd* are easier to understand when graphically described in terms of ellipsoids. In Fig. 4.9 the ellipsoids (99.9% probability) for the *x*(Y)=0.50, hereafter taken as a reference, are shown. It should be noted that for this sample M1 and M2 are occupied 50% by Y and 50% by Ce, O1 sites are fully occupied, while O2 sites are 50% occupied, according to Ce concentration.

The shape of the *msd* of the two cations sites is different: M1 *msd* has a cigar like shape, while M2 *msd* is essentially flat. The ellipsoids are particularly elongated towards the nearby O2 sites. In pure RE_2O_3 every cation is surrounded by six O ions (O1 site) whilst two O sites (O2) are vacant. When Ce^{+4} is introduced into the C-type structure, O ions also enter the structure for charge balance. The cations in the center of the cuboids, highlighted in Fig 4.9 (*right*) are alternatively attracted towards the occupied O2 site. When both O2 sites are fully occupied, the cation lies in the center of the cuboid, resembling a fluorite structure.

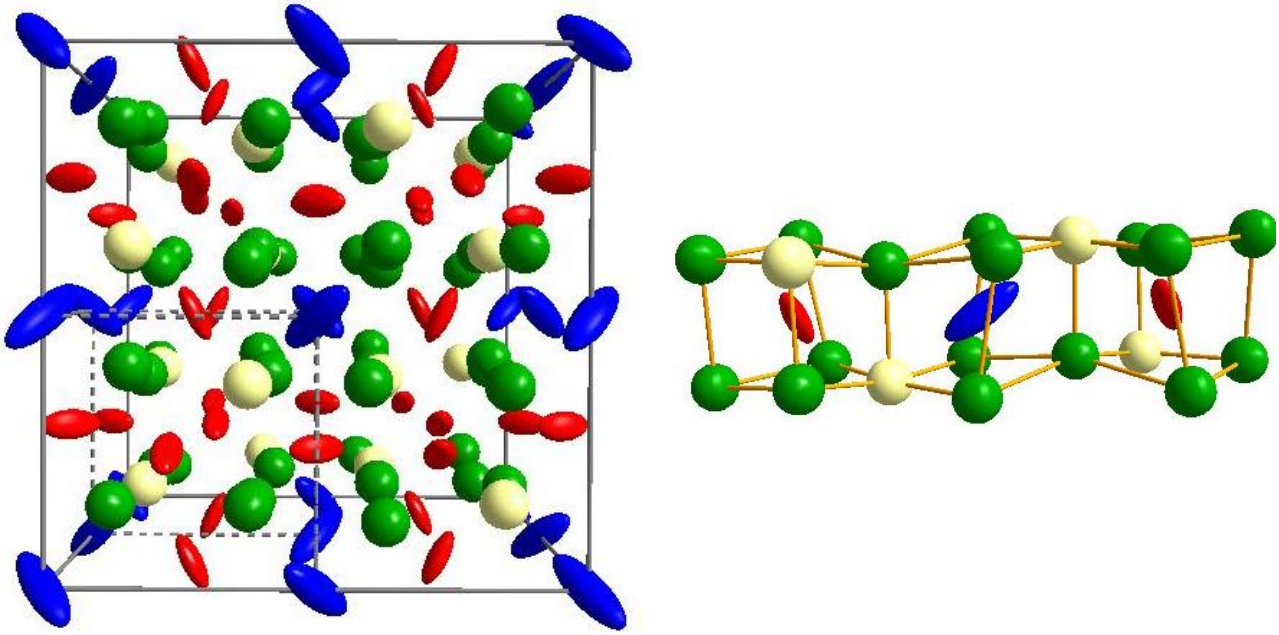

Fig. 4.9. Left: ellipsoids (99.9 % probability) for the *x*(Y)=0.50 sample. Blue: M1 site; red: M2 site; green: O1 site; white: O2 site. Right: M-M connectivity extracted from the left panel.

The mean crystallographic structure can be thus envisaged as the sum of different local configurations. The *x*(M2) coordinate is 0 in a fluorite structure and ~-0.03 in undoped sesquioxides. An intermediate value of the *x*(M2) coordinate could result from the average of different contributions: on one hand, when both O2 sites are locally occupied, the cation lies at the center of a fluorite-like cuboid; on the other hand, when at

least one of the O2 sites is empty, the cation is shifted away from the center of the cell. By increasing Ce amount, the fraction of full O2 sites increases, that is the fraction of fluorite-like cuboids. In this way the mean shift of the M2 ion from the center of the cuboid exhibits intermediate values, as observed in Fig 4.2.

In a fluorite structure, instead, the amount of vacancies is not enough to induce their long range ordering. Disorder is present, but the thermal parameter has no preferred orientation. A further insight into the local atomic arrangement can be gained by the PDF approach.

4.4. Real space analysis

The real space data analysis results are reported according to a multi-step approach: *first* the G(*r*) curves are subjected to *direct analysis* for the first coordination shells, *then* the *average* model is applied in different *r*-ranges of G(*r*) to determine the presence and the extent of the disorder, *finally* a model for mapping the very local structure is examined and compared with the *average* model.

4.4.1. Direct Analysis

The G(*r*) curves for all the samples investigated are shown in Fig 4.10. The peaks are assigned based on the fluorite and C-type structural models.

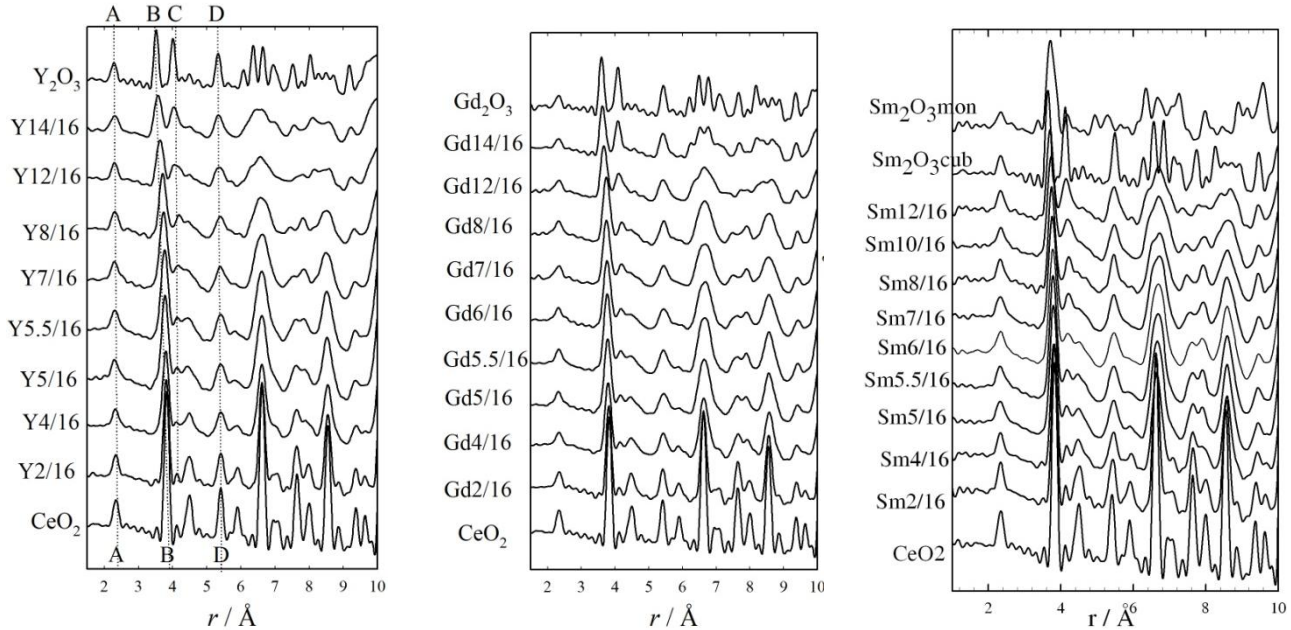

Fig. 4.10. G(*r*) curves for Y (*left*), Gd (*middle*) and Sm (*right*) doping. Labels are given in the left hand panel, based on the average fluorite and C-type structure of the end members of the solid solutions. As to Sm-doping, also the G(*r*) of pure Sm_2O_3 in its monoclinic form is displayed.

Here follows a list of the principle atom pairs that will be investigated later on in this thesis. Some peaks in the CeO_2-Y_2O_3 panel are labeled for simplicity. The labels apply to the other dopants as well. The first peak (A) corresponds to M-O pairs. In fluorite samples only one M-O pair is expected, whereas in C-type the observed peak corresponds to the average over a number of contributions. Being XRPD on doped ceria particularly sensitive to M contributions, beyond the first neighbor M-O pair, only M-M pairs are considered. The second peak (B) corresponds to M-M pairs: the single fluorite and the shorter C-type distance. The choice to join the two contributions into the single B peak is arbitrary and suggested by the trend as a function of composition, as discussed in the following. The third peak (C) is the second M-M pair in C-type.

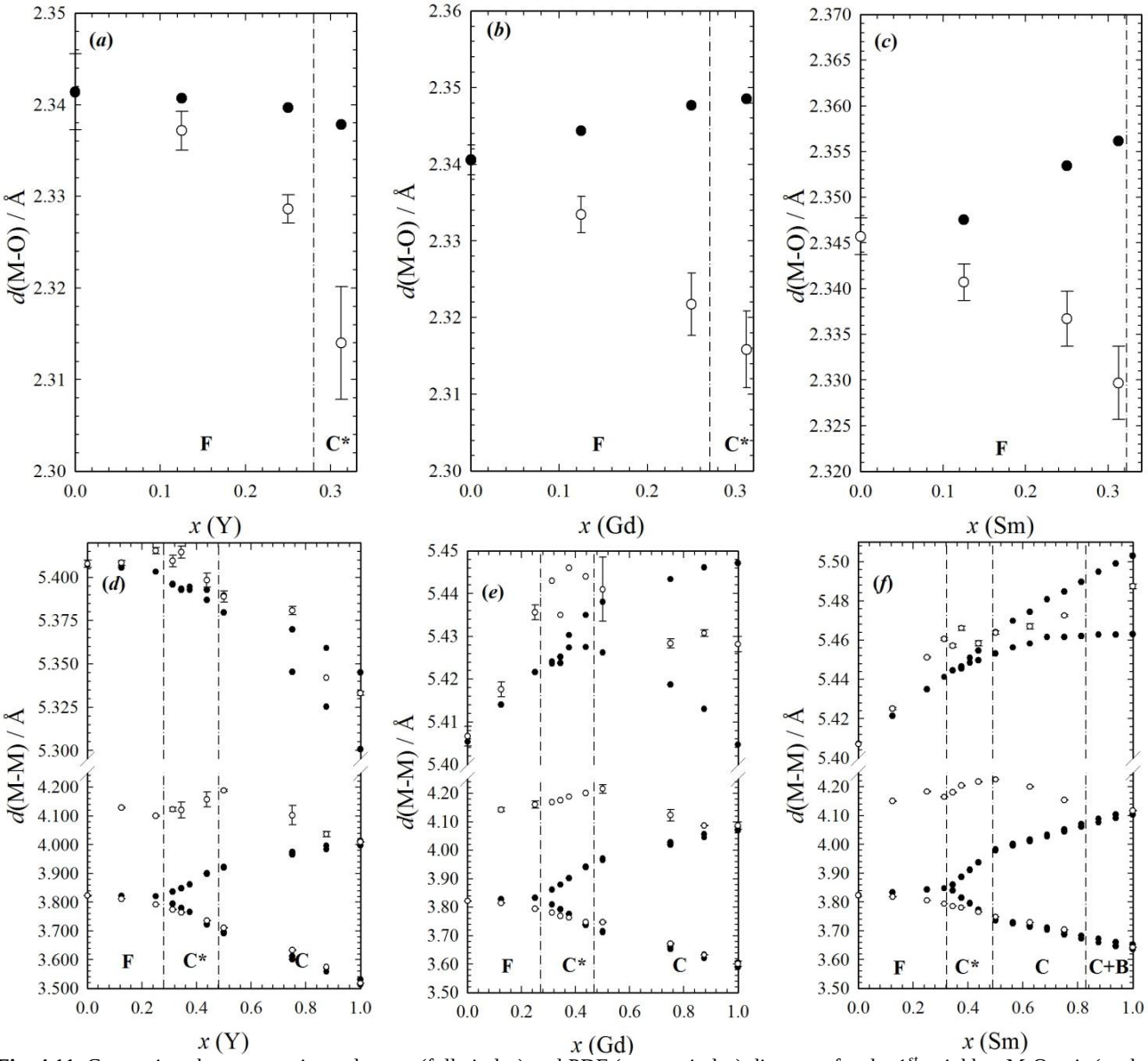

Fig. 4.11. Comparison between reciprocal space (full circles) and PDF (empty circles) distances for the 1st neighbor M-O pair (peak A, *top*) and the M-M pairs (peaks B, C and D, *bottom*) for Y (*left*), Gd (*middle*) and Sm (*right*) doping.

A fourth peak (D) is considered and it concerns to 2nd neighbor M-M pairs in fluorite, corresponding to the cell parameter length. In C-type this distance is split into two, too close to be resolved. In section 4.3 we saw that the transition from fluorite to C-type is accompanied by a continuous evolution of the average structure. The same is observed for the local structure. At a first glance, this is particularly true of M-M pairs: for Y, Gd and Sm, the single M-M peak of ceria splits into two with doping, giving rise to a continuum of structural evolution.

The position of a peak, as well as its width and its area, were determined after the so called *direct analysis* of the G(*r*) peaks, see section 2.2 for details. The corresponding peak positions for Y-, Gd- and Sm- doping are shown in Fig. 4.11 (*a*), (*b*) and (*c*), respectively. The shortening of the M-O distance is common to all of the three dopants, even when the average M-O distance increases, which is the case of *RE* = Gd and Sm.

The M-M distance distribution is shown in the (*d*), (*e*) and (*f*) panels of the same figure. Again some noteworthy differences with respect to the average structure are evident:

- the first neighbor M-M (B) behaves similarly to the above discussed M-O pair: it contracts with doping even when a neat expansion of the cell is observed.
- a peak observed at ~4.1 Å for $x(RE)$=0.125 and 0.250 was assigned to M-M pairs (C), based on the trend with composition of the second M-M pair in C-type. However, only one single M-M peak is expected in a long range fluorite structure.
- the composition dependence of the second M-M C-type peak (C) strongly differs from the average structure. By adding cerium to pure RE_2O_3, this distance increases instead to "converge" to the single M-M fluorite distance.
- for low doping concentration, the pair at ~5.4 Å (D) has a similar trend to the second M-M C-type distance. It increases when the average structure is fluorite, then slightly converges to its mean value when the structure is C-type. It should be noted that the lengthening of this pair is observed for all the three dopants, although for Y-doped ceria the cell is observed to contract upon doping.

Some remarks are due about the above findings.

First of all, different dopants seem to induce the same kind of distortions in the structure of ceria. By considering the fluorite structure as a reference, the shrinks of the first M-O and M-M pairs, the expansion of

the second M-M pairs and the presence of C-type-like M-M distance is observed regardless of the kind of dopant and of the average structure.

Particular attention should be devoted to the second M-M peak (C) observed in the fluorite structure. By looking at Fig. 4.11 the reader could argue that a second M-M peak in fluorite appears even in pure ceria. This would imply that the peak C is not induced by doping. Actually, the contribution at ~4.1 Å in pure ceria is due to a termination ripple arising from the combination of the Q_{max} truncation effect with very low *msd*. By increasing the *msd*, this effect reduces. Conversely, in doped samples the observed peak is expected to reflect some structural information. Anyhow, we cannot exclude the position of the peak to be somehow affected by the presence of some spurious oscillations, particularly for the $x(RE)$=0.125 composition. A more complete demonstration of the non-structural origin of this peak in pure ceria is given in Appendix, section A4.2.

The presence of the peak C even in fluorite samples can be deemed as the evidence that the local atomic arrangement in long range fluorite samples differs from that of a fluorite. It is evident from Fig 4.10 that the aforementioned peak C increases in intensity with doping, whereas the peak B reduces. This effect was quantified through direct analysis by determining the area of each peak. Fig. 4.12 reports the evolution with doping of the area of the peak C, normalized to the sum of the area of peaks B (A_B) and C (A_C). The value for pure CeO_2 was set to 0.

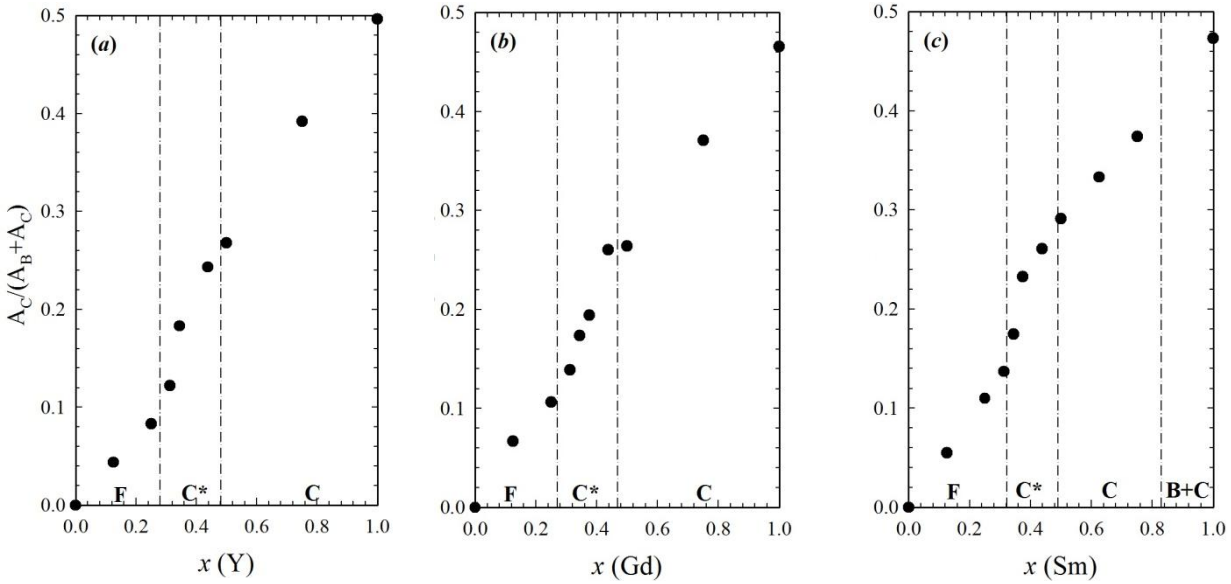

Fig 4.12. Area of peak C normalized to the sum of the area of peaks B and C for Y (*a*), Gd (*b*) and Sm (*c*) doping.

The normalized intensity of the peak C increases with doping and features a similar trend to the one of the x(M2) coordinate. It basically provides the same information in terms of structural evolution, but in the real

space. Without the constraint imposed by symmetry in the reciprocal space, a clear structure evolution can be appreciated even in long range fluorite samples. In the latter, a linear trend is observed, especially for *RE* = Sm. Only when entering the C* region the trend deviates and the intensity of the peak C steeply increases, as to indicate the growing of the C-type phase. In the C-type region a different linear trend is restored.

Finally, the peak width (not shown here) varies with doping with a bell-like shape very similar to the ones observed in Fig. 4.7, while discussing the way U_{mean} are affected by disorder. This finding could imply that disorder triggers a very broad distance distribution, not possible to resolve even at the very high Q_{max} of the experiments.

4.4.2. modeling

The first step of PDF modeling is to determine whether the long range structural model is apt to describe the low-*r* region of the PDF. If it is not the case, it is an indication of disorder. Its extent can be estimated by monitoring the fit residual R_w in different *r* ranges.

Two long range models, defined as *average*, were considered. A *fluorite* model was applied by varying the cell parameter, an overall scale factor, metal and oxygen *msd* and a parameter accounting for correlated motion. Five parameters in all. A *C-type* model was applied by varying the cell parameter, an overall scale factor, two metal and one oxygen *msd*, the *x*(M2) coordinate, three oxygen (O1) coordinates and a parameter accounting for correlated motion. Ten parameters in all. In both cases, the presence of two metal ions is taken into account by randomly populating the cation positions with Ce^{4+} and RE^{3+} ions in due proportions.

In Fig. 4.13, either the *fluorite* or *C-type* model was applied based on the long range structure on Gd-doped samples with different composition. The *average* model is consistent with PDF data only for distances larger than ~10 Å for all the three dopants investigated. The fit residual, shown below each plot, is evidently non-random mostly in correspondence of the first two M-M peaks (B and C). This is consistent with the trends observed through direct analysis. A more complex model for describing the short range structure in doped ceria is then required.

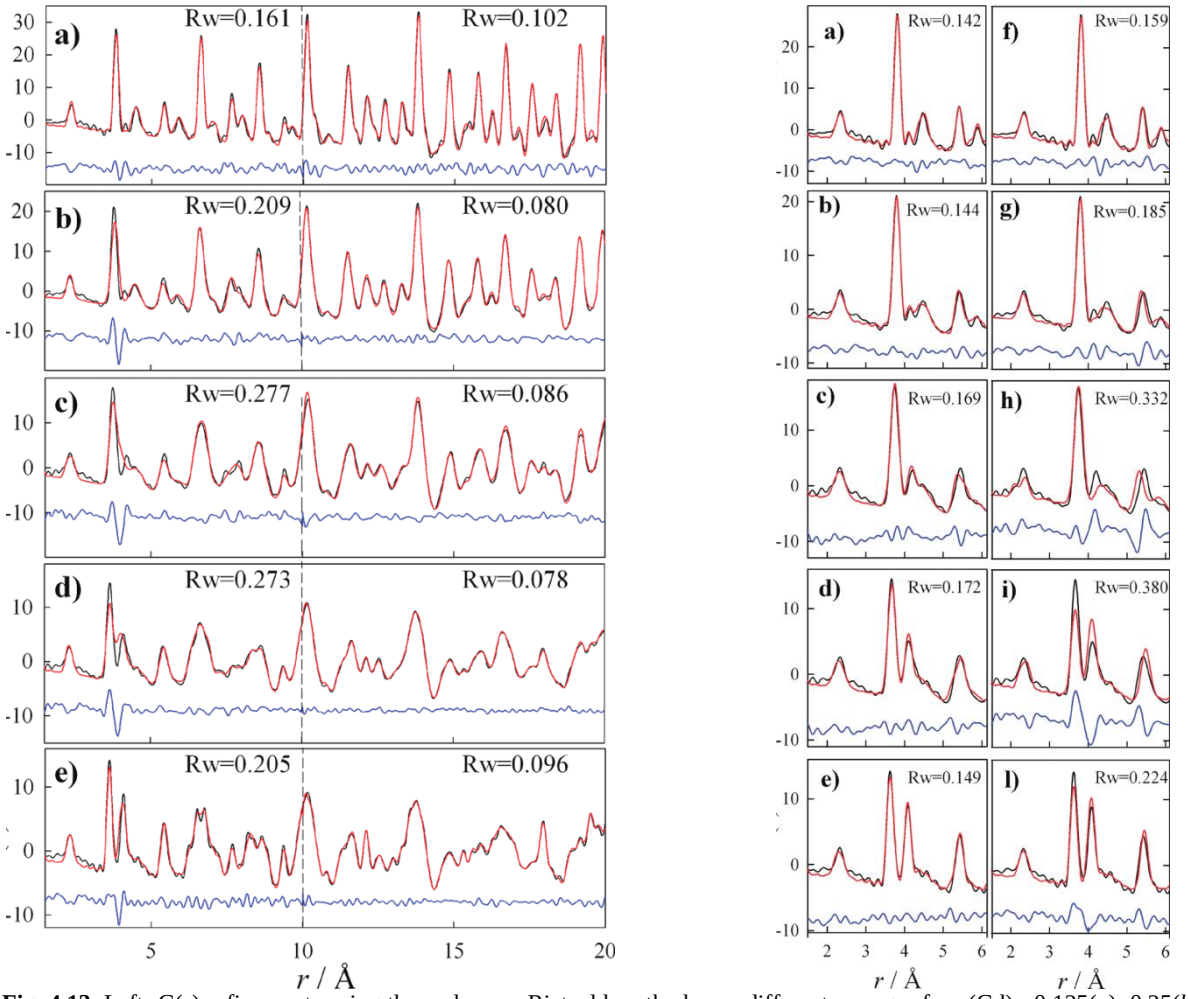

Fig. 4.13. Left: G(*r*) refinements using the real space Rietveld method over different *r* ranges for *x*(Gd)= 0.125(*a*), 0.25(*b*), 0.50(*c*), 0.75(*d*), 0.875(*e*). Observed (black crosses) and calculated (red curve) profiles are shown as well as residuals (blue curve). Right: G(*r*) refinements using the real space Rietveld method between 1.5 and 6 Å for *x*(Gd) = 0.125(*a-f*), 0.25(*b-g*), 0.50(*c-h*), 0.75(*d-i*), 0.875(*e-l*) . Results obtained using the *biphasic* model (from *a* to *e*) and the *average* model (from *f* to *l)*. See [*Scavini et al. 2012*] for other details.

4.4.2.1. The biphasic model

The presence of a long M-M pair even in long range fluorite samples, as well as its evolution with *RE* concentration in terms of peak position and area, can be viewed as an indication of C-type-like orderings. This can be modeled by considering the coexistence of two different phases at the nanoscale: one C-type, accounting for dopant and vacancies, and one fluorite, resembling the CeO_2 matrix. In order to reduce the total number of parameters, only one *msd* parameter for M ions and another one for O ions were considered. The resulting fits performed in the $1.5 < r < 6$ Å range for *RE* = Gd are shown in the right hand panel of Fig 4.13 and are compared to the *average* model applied to the same *r*-range. Similar results are obtained for *RE*= Y and Sm. Some residuals are observed, but the reader should be aware of the assumptions made when applying the *biphasic* model. To a first approximation, the two phases are considered in their pure form, even

though some vacancies and dopants are likely to form in the fluorite phase. The vice versa applies to some Ce and O ions in C-type. This is testified by the intermediate value of *x*(M2), which occurs when O ions enter the C-type structure. Only pure oxides were implemented in the fit in order to avoid overparametrization. Moreover, any possible interaction between the two phases is neglected. The C-type fraction and the *x* coordinate of the *RE*2 site are reported in the Appendix in section A4.3. By increasing doping concentration along the solid solution, the C-type fraction is observed to increase and *x*(*RE*2) exhibits more negative values.

When considering a long range fluorite structure, which is the one of interest for application, the *biphasic* model can be pictured as a set of C-type-like RE_2O_3-rich droplets embedded in a CeO_2-like matrix. Being the size of the droplets quite limited, rather than a true phase separation at the nanoscale, the *biphasic* model can be regarded as a strong indication that the cations tend to retain their local environment as in the pure oxides.

The attempts to extend the *biphasic* model to *r* ranges wider than ~6 Å produced unsatisfactory results. At the same time, the *average* models fit well the experimental G(*r*) curves only for $r > \sim 10$ Å for all the investigated compositions. This could suggest that interatomic vectors up to ~6 Å refer to mainly *intra*domain distances while for $r > \sim 10$ Å mainly to *inter*domain distances. In the intermediate *r* range ($\sim 6 < r < \sim 10$ Å) both *inter*- and *intra*domain vectors should be present. We can thus only estimate the correlation length of the droplets to be in the 6 ÷ 10 Å range. An alternative or complementary explanation would be that O vacancies and *RE* ions could order along preferred directions [*Ye et al., 2009*], forming droplets having different correlation lengths along different directions. To prove this idea, it is clear that a more complex approach (RMC, DISCUS, etc..) than the adopted real space refinement is required to understand the structural details over different scales.

The *biphasic* model is also in agreement with the HRTEM findings of C-type structured domains, except for their extent: a few nanometers large domains were observed by HRTEM, while the PDF analysis indicates that the disorder is mainly localized within ~1 nm. However, one should consider that the extent of disorder determined via PDF is somewhat arbitrary: it can be considered as the *r*-region in which it possible to resolve differences in PDF peaks, in terms of shape or position, by refining the experimental data against an average structural model. PDF and HRTEM results can be compared from a different point of view. As point out by Li *et al.* [*Li et al., 2011*], the spread of nano-sized domains with doping observed by

transmission microscopy implies that a larger part of the sample is occupied by the domains. This is consistent with the continuous increase of C-type fraction that we observed by increasing the *RE* amount along the solid solution.

4.5. Final remarks

The whole compositional range of the CeO_2-RE_2O_3 (*RE*=Y, Gd, Sm) systems was investigated through high resolution XRPD by combining the reciprocal and real space approaches. Except for $x(Sm) \geq 0.875$, all the investigated samples were single phase, either fluorite or C-type.

The x(M2) coordinate was taken as a reference to determine the phase composition. Three different regions were determined for each dopant. When $x(M2)=0$, the structure is fluorite. In the second region, defined as C*, the linear variation of x(M2) with composition is accompanied by the presence of broaden superstructure peaks, described in terms of antiphase boundaries. The limit of $x(M2) \rightarrow 0$ determines the onset of the C-type structure. The *RE*(Y, Sm, Gd) solubility limit in fluorite is around $x \sim 0.30$. In the third region a different linear trend of x(M2) with composition corresponds to a "standard" C-type phase without anomalous peak broadening.

The analysis of the thermal parameters indicates that the largest disorder occurs in correspondence with the boundary between the C and C* regions. The anisotropic thermal parameters indicate that disorder has a strong directional character. The M1 site, which is the one most affected by disorder, has a cigar-like shape ellipsoid while M2 is flat-shaped. The ellipsoids are mainly elongated towards the nearby O2 sites, which are partially filled, based on the actual Ce concentration. The elongated ellipsoids are evidence of static disorder in atomic positions: locally the cations occupy different positions based on which O sites are actually filled.

In view of the above considerations, the intermediate value of x(M2) observed by varying the doping concentration can be considered as the result of different configurations, such as fluorite-like (with $x(M2) = 0$) or C-type-like ($x(M2) \sim 0.03$). To support this finding, G(r) curves of doped samples are better described by considering the weighted contributions of fluorite- and C-type-like cuboids (*biphasic* model), rather than an average distribution (*C-type* model).

The investigation of highly doped systems helps the understanding of the mechanisms at works in lightly doped ceria, which is attractive for application. In this case the average structure is fluorite. Although the

doping-induced disorder is isotropic, some features of C-type like ordering are evident in the G(*r*) curves. By increasing the doping concentration, the local scale C-type ordering, indicated by the normalized area of peak C, increases linearly up to the dopant solubility limit. A further amount of dopant (i.e. of vacancies) produces the formation of broaden superstructure peaks in the XRPD pattern. The broadening, which can be an indication of the limited coherence length of vacancy orderings, decreases with doping.

The formation of superstructure peaks is not accompanied by any noteworthy transformation on the local scale. This confirms that a continuum of structural evolution occurs, from light to heavy doped systems. At the same time, the PDF peak C, deemed as a fingerprint of structural disorder, steeply increases in the C* region, as to indicate the develop of the C-type structure on a wider part of the sample.

References

[*Balasz and Glass, 1995*] G. B. Balasz and R. S. Glass, *Solid State Ionics* 1995, **76**, 155-162.

[*Burbano et al., 2012*] M. Burbano, S. T. Norberg, S. Hull, S. G. Eriksson, D. Marrocchelli, P. A. Madden and G. W. Watson. *Chem. Mater.* 2012, **24**, 222-229.

[*Chavan and Tyagi, 2005*] S. V. Chavan and A. K. Tyagi, *Materials Science and Engineering* 2005, **A 404**, 57–63.

[*Deguchi et al., 2005*] H. Deguchi, H. Yoshida, T. Inagaki and M. Horiuchi *Solid State Ionics* 2005, **176**, 1817-1825.

[*Hayashi et al., 2000*] H. Hayashi, R. Sagawa, H. Inaba and K. Kawamura, *Solid State Ionics* 2000, **131**, 281-290.

[*Kilner, 2000*] J. A. Kilner, *Solid State Ionics* 2000, **129**, 13–23.

[*Kim and Stebbins, 2007*] N. Kim and J. F. Stebbins, *Chem. Mater* 2007, **19**, 5742-5747.

[*Leoni et al., 2006*] M. Leoni, T. Confente and P. Scardi, *Z. Kryst. Suppl.* 2006, **23**, 249-254.

[*Li et al., 2011*] Z.-P. Li, T. Mori, F. Ye, D. R. Ou, J. Zou and J. Drennan, *Phys. Rev. B*, 2011, **84**, 180201.

[*Mittemeijer and Scardi, 2004*] E. J. Mittemeijer and P. Scard in *Diffraction Analysis of the Microstructure of Materials*, 2004, Springer.

[*Moriga et al., 1989*] T. Moriga, A. Yoshiasa, F. Kanamaru and K. Koto, *Solid State Ionics* 1989, **31**, 319-328.

[*Nakamura, 2010*] A. Nakamura, *Solid State Ionics*, 2010, **181**, 1543–1564.

[*Ou et al., 2008*] D. R. Ou, T. Mori, F. Ye, J. Zou, G. Auchterlonie, and J. Drennan, *Phisical Review B* 2008, **77**, 024108

[*Ou et al., 2006a*] D. R. Ou, T. Mori, F. Ye, M. Takahashi, J. Zou and J. Drennan, *Acta Materialia* 2006, **54**, 3737-3746.

[*Roisnel and Carvajal, 2001*] T. Roisnel and J. Rodriguez-Carvajal, *Materials Science Forum* 2001, **378-381**, 118-123.

[*Scardi and Leoni, 2005*] P. Scardi and M. Leoni, *Acta Materialia* 2005, **53**, 5229–5239.

[*Scavini et al., 2012*] M. Scavini, M. Coduri, M. Allieta, M. Brunelli and C. Ferrero, *Chem. Mater.* 2012, **29**, 1338-1345.

[*Wang et al., 2006*] Y. Wang, H. Kageyama, T. Mori, H. Yoshikawa and J. Drennan, *Solid State Ionics*, 2006, **177**, 1682-1685.

[*Ye et al., 2009*] F. Ye, T. Mori, D. R. Ou and A. N. Cormack, *Solid State Ionics* 2009, **180**, 1127-1132.

[*Ye et al., 2009b*] F. Ye, T. Mori, D. R. Ou, J. Zou and J. Drennan, *Solid State Ionics* 2009, **180**, 1414-1420.

5. The role of the dopant: combining X-Ray and Neutron Powder Diffraction

5.1. Introduction

As discussed above, in *RE*-doped ceria ionic conductivity occurs by oxygen diffusion through a vacancy mechanism [*Kilner, 2008*]:

$$RE_2O_3 \xrightarrow{CeO_2} 2RE'_{Ce} + 3O_O^x + V_O^{\cdot\cdot} \quad (5.1)$$

The isothermal ionic conductivity σ is then expected to increase monotonically upon doping, regardless of the dopant involved. It is well known that the performance of solid electrolytes in fuel cell devices strongly vary, depending on the selected *RE* dopant. Nevertheless, some phenomena are common to all doped ceria materials: i) a maximum of σ is generally observed at a critical *RE* concentration *x*, above which σ decreases [*Faber et al., 1989, Zhang et al., 2004, Jung et al., 2002*]; ii) local probes like EXAFS [*Deguchi et al., 2005, Ohashi et al., 1998, Yamazaki et al., 2000*] and NMR [*Kim and Stebbins, 2007, Heinmaa et al., 2010*], as well as atomistic simulations [*Hayashi et al., 2000, Minervini et al., 1999, Ye et al., 2009*] explain the conductivity drop in terms of defect clusters formed by substitutional cations and oxygen vacancies; iii) at high doping concentrations HRTEM [*Ou et al., 2006a, Ou et al., 2008*], SAED and EELS [*Ou et al., 2006b, Mori and Drennan, 2003*] measurements suggest that large domains of a few nanometers in size form and act as deeper traps for oxygen vacancies; iv) absorption spectroscopy measurements usually report Ce in the +4 state, with a coordination number of about 8, which decreases upon doping; conversely *RE* dopants are usually reported in the +3 state, with a coordination number around 7 [*Deguchi et al., 2005, Ohashi et al., 1998, Yamazaki et al., 2000*]. This is true for all the lanthanoids, except for Pr and Tb, which are characterized by a mixed valence state [*Nitani et al., 2004, Martìnez-Arias et al., 2005*]. The different fuel cells' performances upon varying *RE* dopant are explained by considering the size mismatch between the host and the dopant cation, which plays an important role in the activation energy of the migration process [*Kilner, 2008*]: dopants whose ionic radius strongly differs from that of Ce^{+4}(VIII), make the diffusion process more difficult. The nature of the dopant also affects the conformation of the defect clusters:

Minervini *et al.* [*Minervini et al., 1999*] showed that for cations smaller than Gd^{+3} it is energetically favorable for the vacancy to be in a first neighbor position with respect to the substitutional ion, while cations larger than Gd^{+3} prefer a second neighbor vacancy. However, this is in contradiction with 7-fold coordinated *RE* cations observed by the above mentioned EXAFS studies.

Finally, on the basis of EXAFS measurements, Deguchi *et al.* [*Deguchi et al., 2005*] suggested that while doping, the *RE*-dopant retains its chemical environment as in its pure oxide. At the same time, the relaxation of O and cations around a vacancy is detailed by Neder *et al.* [*Neder et al., 1992*] on a ceria parent compound.

Aim of this chapter is to elucidate how the local structure changes as a function of the different dopants. Five different dopants (Yb, Y, Tb, Nd, La) were chosen for: i) covering a wide range of ionic radii and ii) allowing a combined XRPD and Neutron Powder Diffraction (NPD) investigation. Actually, not all lanthanide elements in their natural isotopic composition are suitable for a NPD study, because of the large neutron absorption cross section of some isotopes. The employ of Gd and Sm as dopants in their natural isotopic composition is precluded.

XRPD and NPD can be seen as complementary probes for doped ceria materials: the X-ray intensity contribution is mainly dominated by the cations, while NPD is far more sensitive to oxygen. In Table 5.1 the neutron scattering lengths [*Sears, 2006*] together with the atomic numbers, the values of the RE^{+3} ionic radii in 8-fold and 7-fold coordination based on [*Shannon, 1976*] are shown for all the elements of interest in this study. Ionic radii are usually reported in 8-fold coordination, which is the cation-coordination in the fluorite structure. However, EXAFS results suggest that a 7-fold coordination should be more appropriate.

This chapter is divided into two main sections. *First* we give an overview of the structural information obtainable on doped ceria through NPD. Particular emphasis is placed on the case Y doping, in order to compare the results with XRPD. *Then* we combine NPD and XRPD to make clear the role of the dopant at fixed doping concentration, $x(RE)= 0.25$. Experimental data were analyzed using both the reciprocal space Rietveld analysis and the atomic Pair Distribution Function (PDF).

Part of the present work was published in [*Coduri et al., 2012*] and in [*Coduri et al., 2012b*].

Table 5.1. Neutron scattering length *b*(fm), neutron absorption cross section (barns), atomic number *z*, ionic radius in 7- and 8-fold coordination for the elements of interest in this study.

Element	*Yb*	*Y*	*Tb*	*Gd*	*Sm*	*Nd*	*La*	*Ce*	*O*
b / fm	12.43	7.75	7.38	6.5-13.82	0.8-1.65i	7.69	8.24	4.84	5.80
abs c.s	34.8	1.28	23.4	49700	5922	50.5	8.97	0.63	0.0002
z	70	39	65	64	62	60	57	58	8
(VII)/Å	0.925	0.96	0.98	1.00	1.02	1.04	1.10	1.07	-
(VIII)/Å	0.985	1.02	1.04	1.05	1.08	1.11	1.16	0.97[1]	-

[1] Ce^{+4} is considered.

5.2. Experimental section

A set of $Ce_{1-x}RE_xO_{2-x/2}$ (*RE* = La, Nd, Y, Tb, Yb; *x*= 0.125, 0.250, 0.375, 0.500) samples were prepared with the *Pechini* sol-gel method and fired at 900°C for 72 hours.

XRPD patterns on *x*(*RE*)=0.25 samples were collected at the ID31 beamline of the ESRF, Grenoble in the 2θ range $0<2\theta<120°$ up to Q_{max} = 29.4 $Å^{-1}$. Experimental data were collected at an incident X-ray wavelength λ=0.3541 Å. Additional data were collected also on CeO_2 (Aldrich ≥99.0%), empty capillary and air background. In order to attain XRPD data quality for the PDF, all patterns were obtained summing intensity counts over several scans performed at constant temperature (*T* = 90 K).

The NPD analysis was performed on all the $Ce_{1-x}RE_xO_{2-x/2}$ (*RE* = La, Nd, Y, Tb, Yb; *x*= 0.125, 0.250, 0.375, 0.500) samples. NPD patterns for reciprocal space analysis were collected at the D20 instrument of the ILL, Grenoble at an incident neutron wavelength λ=1.3595 Å in the 2θ range $13<2\theta<144°$. About 15 minutes acquisition time diffraction patterns were collected at different temperatures, warming the samples from 4 K to room temperature. The *RE*=Y sample as well as CeO_2 were measured during another experiment following a different collection strategy: after a long scan (20 minutes) at 4 K, 2 minutes acquisition time diffraction patterns were collected warming the sample at the rate of 0.75 K/min from 4 K to room temperature. An about 30 minutes acquisition scan was recorded at *T* = 90 K on the *x*(Y)=0.50 sample.

NPD patterns for real space analysis were collected at the D4c instrument of the ILL during two different experiments at incident neutron wavelengths λ_1=0.4975 Å and λ_2=0.4969 Å *T* = 90 K. The quality of the data is the same, as well as the covered *Q*-range, that is between 0.35 and 23.6 $Å^{-1}$. Empty cryostat, vanadium rod, empty cans and boron powder patterns were also measured in order to properly subtract the background and normalize the data. The backgrounds were measured periodically during the experiment in order to check

their stability. PDF quality patterns were collected for each sample within about 4 hours on samples of approximately 7 g mass.

5.3. Applying NPD to doped ceria

In this section we report on the results obtained through NPD, using Y as a reference dopant. After determining the long range structure of the samples, in the section dedicated to the reciprocal space analysis the *msd* evolution with temperature and composition is investigated. We shed light on O orderings by exploiting *Anisotropic mean square displacements* (*Amsd*). In the real space part *first* the effect of doping on the local structure is investigated; *then* an overview on direct analysis results is given.

5.3.1. Reciprocal space analysis

NPD data were processed as described in chapter 2. All the investigated samples exhibit CeO_2-like fluorite structure up to the $x(RE)$=0.375 doping composition, except for x(Y)=0.375, which has a C* structure (see chapter 4). The $x(RE)$=0.50 composition results in fluorite samples for *RE* = La and Tb, C-type for *RE* = Y and Nd (the latter being C*), while the Yb-doped sample is inhomogeneous. The cell parameters a_f collected at T = 90 K are displayed in Fig. 5.1. It is clear that the cell parameter reflects the size of the dopant: the larger the dopant, the larger the cell parameter.

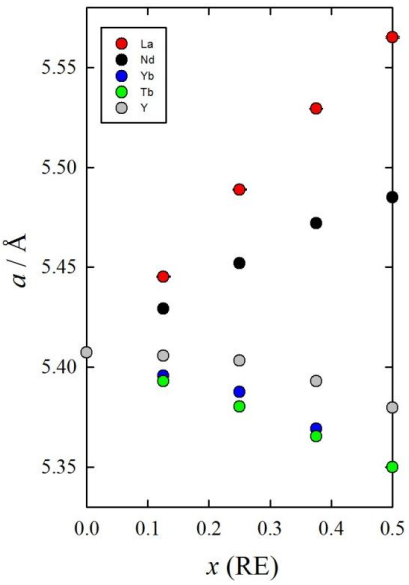

Fig. 5.1. Cell parameter a_f as a function of dopant concentration. Labels are reported in the inset.

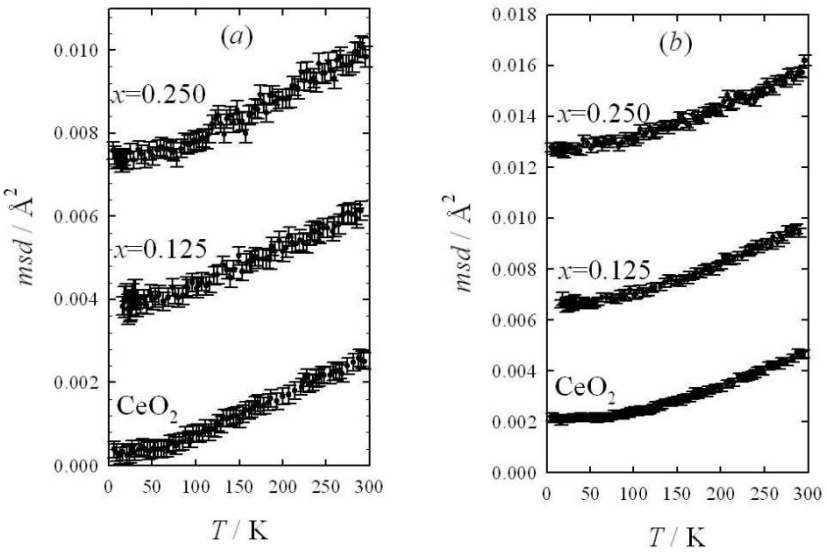

Fig. 5.2. *msd* in Y-doped ceria compared to pure ceria for the metal (*a*) and the oxygen (*b*) site. Note that the Y axis scales are different.

As described in the previous section, the doping induced disorder results in increased *msd*. In Fig. 5.2 the *msd* for M and O ions are shown for *x*(Y)=0.125 and *x*(Y)=0.250 and are compared to pure CeO_2. It is evident that doping produces an increase of *msd* compared to the reference CeO_2, without modifying the shape of the curve, a fingerprint of doping-induced disorder. The *msd* for all the samples having fluorite structure are reported in Fig. 5.3 for each single dopant investigated. Note that the scale is the same in all panels to facilitate comparisons. It is evident that the largest disorder occurs for *RE*=Nd and La, while smaller *msd* are detected for Tb.

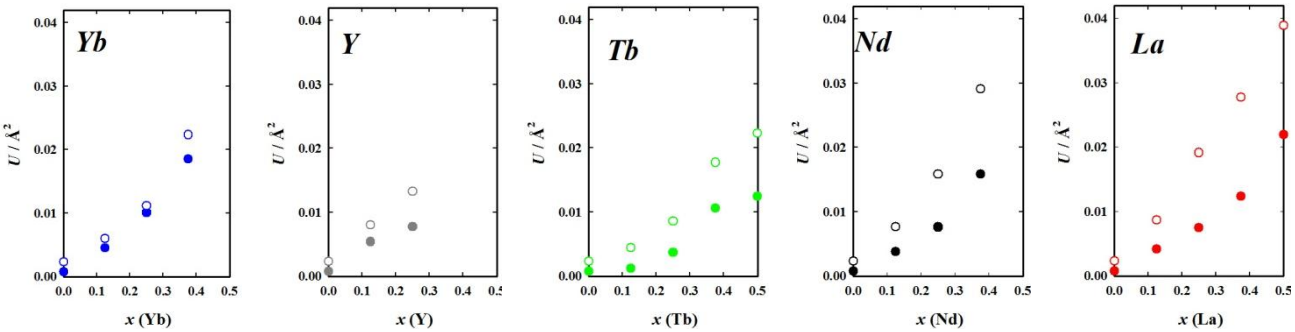

Fig 5.3. *msd* of *RE*-doped at different *RE* concentration. Full circles: metal site, empty circles: O site. The scale is the same in all panels to facilitate comparisons.

All the above *msd* are referred to long range fluorite samples. As discussed above, the *msd* in fluorite provide an indication of the amount of disorder, but lack of any directional information.

A more comprehensive structural information can be gained by exploiting the *Amsd* with NPD. Because of symmetry constraints, considered the present samples, *Amsd* can be accessed only when the structure is C-type. Among the investigated samples, the only one having C-type structure, without any anomalous superstructure peak broadening, corresponds to the *x*(Y)=0.50 composition. The NPD pattern collected at *T* = 90 K was refined in combination of the XRPD pattern collected at ID31 at the same temperature.

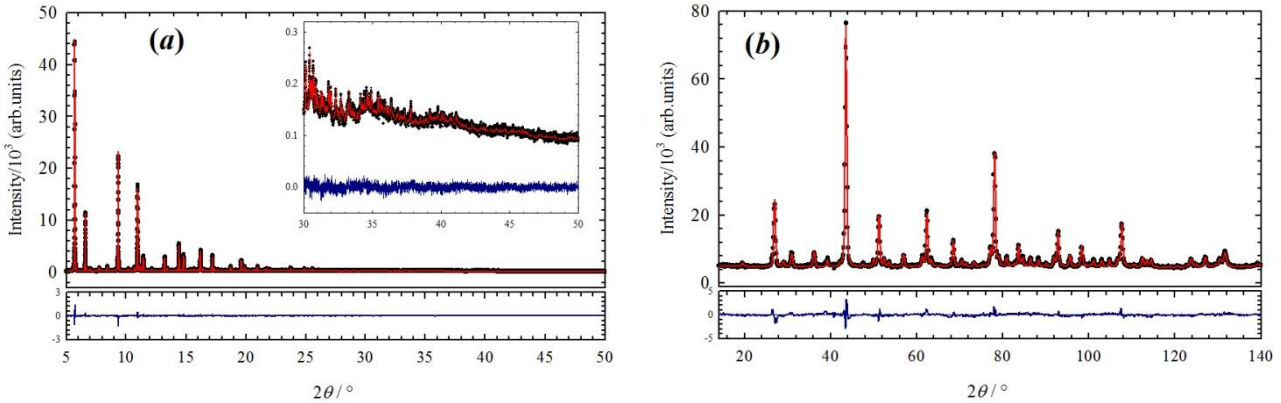

Fig. 5.4. Combined Rietveld refinement on *x*(Y)=0.50 on the XPRD (*a*) and NPD (*b*) datasets. Black points: experimental pattern, red line: calculated, blue line: difference curve. In both cases the difference curve is magnified.

The refined patterns are reported in Fig. 5.4 (*a*) for XRPD and (*b*) for NPD and the results in Appendix, section A5.1. As to cations, the results of the refinements are in line with those obtained employing only synchrotron data. Again a cigar-like shape is observed for the cation in the M1 site as well as a flat-shape for the cation in the M2 site. The corresponding ellipsoids (99.9% probability) are shown in Fig. 5.5.

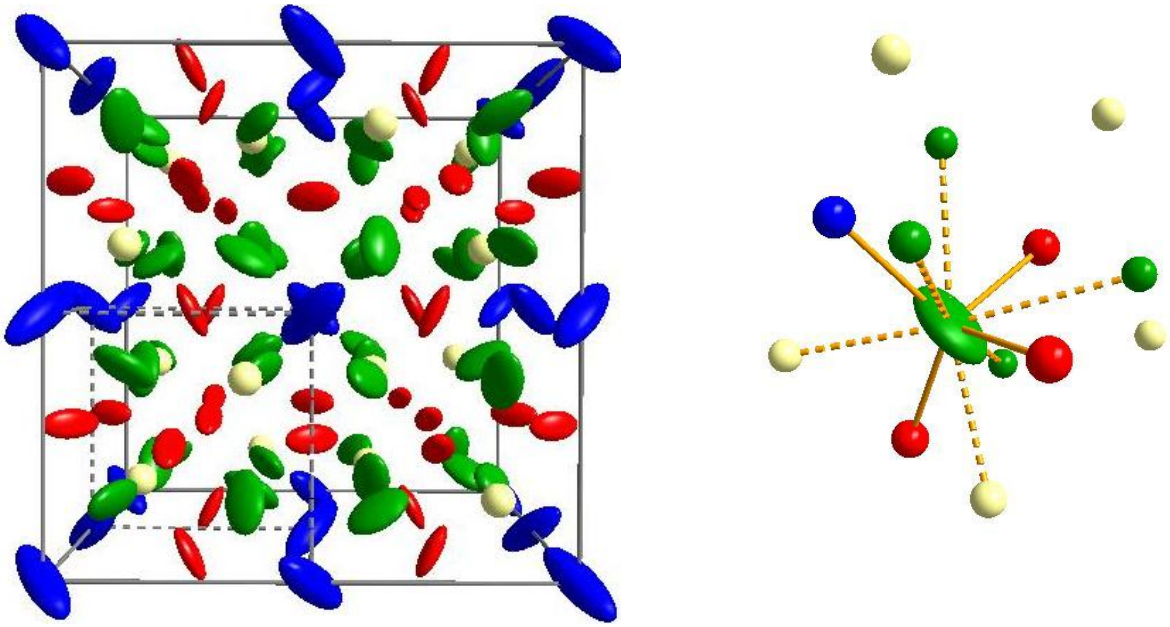

Fig. 5.5. Left: Ellipsoids with 99.9% probability (*left*) obtained from combined XRPD and NPD Rietveld refinements on *x*(Y)=0.50. Blue: M1 site, red: M2 site, green: O1 site, white: O2 site. Right: *Amsd* of the O1 site and its chemical environment. Solid lines: metals tetrahedrally coordinated; dashed lines: O in a distorted octahedral coordination.

The O1 site is tetrahedrally coordinated to three M2 and one M1 sites (~2.3 Å), whilst second neighbors are four O1 (~2.9 Å) and two O2 sites (~2.5Å) in a distorted octahedral environment. O1 has a flat shape similar to that of M1 site, with the flat part towards the partially empty O2 sites. This seems to be consistent with the mechanism of O relaxation towards the vacancy, proposed in [*Neder et al., 1992*, *Hayashi et al., 2000*]: the O in the O1 site is supposed to relax towards one of the two nearby O2 sites alternatively vacant. As proposed by Neder *et Al.* [*Neder et al., 1992*], even farther O2 sites could affect O relaxation.

5.3.2. Real space analysis

Again the use of NPD can provide a complementary information with respect to XRPD, especially in terms of O related parameters. The series of NPD G(*r*) curves of Y-doped samples is plotted in Fig 5.6 (*left*). The first peaks are labeled with the same marks used in Fig 4.10 for XRPD data. Thanks to the similar neutron scattering length of O, Ce and Y (see Table 5.1), a pair involving O-O ions is well resolved at ~2.7 Å. The corresponding peak in G(*r*) curves was labeled as "O". The large weight of O-O pairs is also a drawback for a correct direct analysis, since O-O pairs contribute to all M-M peaks in fluorite. It is then

impossible to resolve M-M to O-O contributions. Thus if the peak B shortens, it does not necessarily imply the shrinks of M-M pairs, but it could also indicate a different O redistribution. For this reason, more attention will be devoted to the first M-O and O-O pairs.

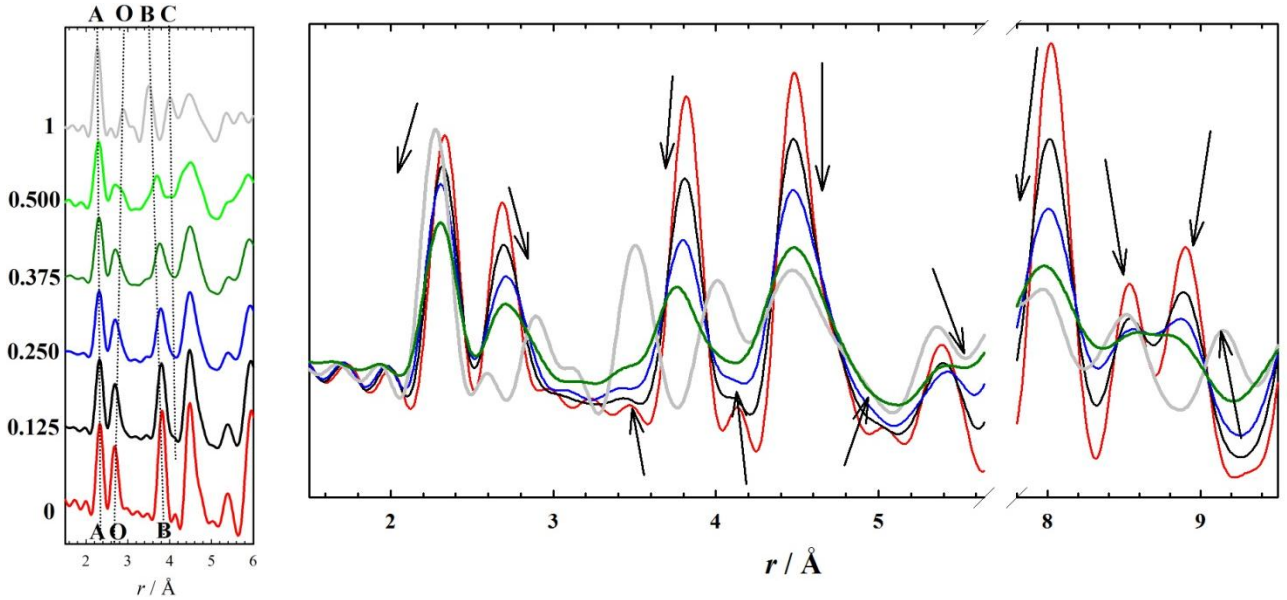

Fig. 5.6. Left: G(*r*) curves for Y-doped samples with different Y concentrations. Dotted lines assign peak to the labels above and below the plot. Right: The same G(*r*) curves plot superimposed. Colors are the same as in the left part, where dopant concentrations are indicated. Arrows are guides for the eye to highlight the effect of doping on peak positions and width.

At a first glance the PDF curves look invariant with concentration up to *x*(Y)=0.375, except for peak broadenings. The same curves are plotted on top of one other in Fig. 5.6 (*right*). The arrows are guides to the eye to indicate the intensity and position shifts of the different peaks by increasing Y concentration. According to a considerable local structural disorder, the G(*r*) peaks related to doped samples look broader than in pure ceria and in most cases Y doping causes the peak features to resemble those of Y_2O_3. In particular, the intensity of the signal at ~4 Å increases with doping. It could be ascribed to a similar effect to the one observed in XRPD.

Since the cell parameter decreases by increasing the doping concentration, all peaks are expected to shift toward lower distances. However, this is true only for the NN (Nearest Neighbors) M-O and the NN M-M distances, while the NN O-O distances increase as well as the peak at ~5.4 Å which in a fluorite structure corresponds to the cell parameter length. All these findings indicate that disorder affects not only the first coordination shells: shifts of peak positions are observed even at higher distances (as indicated after the breaks in Fig. 5.6, *right*). Such a widespread structural disorder cannot be detected with other techniques such as EXAFS, which is sensitive only to the first coordination shells. Besides, interatomic distances involving only light atoms, such as O-O, would be precluded.

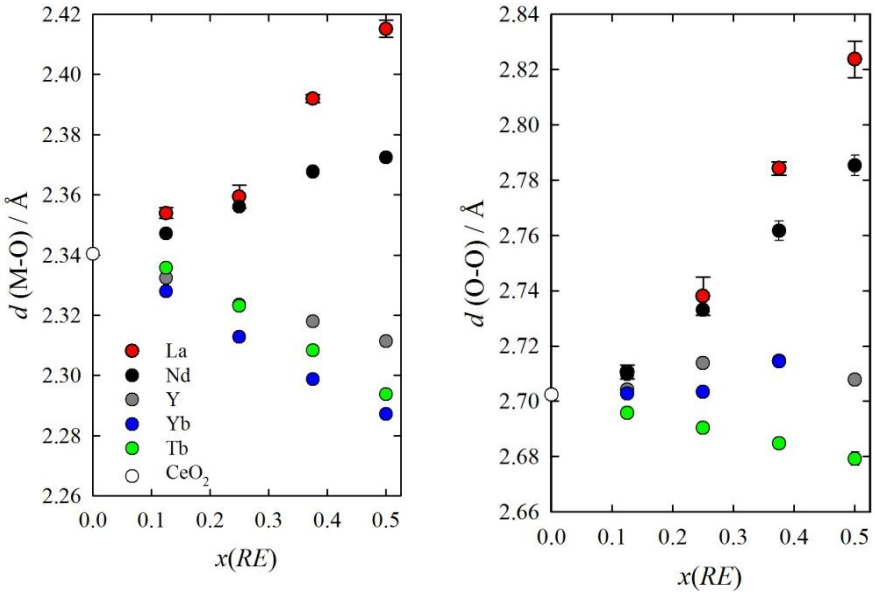

Fig. 5.7. Peak positions determined through the direct analysis of NPD G(*r*) curves for all the dopants investigated for M-O (*left*) and O-O (*right*) pairs. Labels are reported in the left-hand panel.

Let's now move the analysis of peak positions determined through the direct analysis of G(*r*) peaks. The corresponding distances are reported in Fig. 5.7, with reference to 1st neighbor M-O and O-O pairs. Although we saw in chapter 4 that the M-O pairs shrink with doping even when the average cell parameter expands (*RE* = Gd and Sm), this effect is not retained when dealing with larger dopants such as Nd and La. As to the O-O pairs, for all the dopants except for Tb, the O-O distance enlarges with doping, even when a tiny dopant, such as *RE* = Yb, is employed. The relevance of this findings will be discussed in the next section.

5.4. Combining XRPD and NPD

The present section is focused on the determination of the role of the *RE* dopant ion. The *x*(*RE*) = 0.25 composition was chosen for this task, since it guarantees a large amount of doping and is close to the actual doping concentration employed in SOFC devices. Except when explicitly indicated, all the results shown in this section were obtained by combining XRPD and NPD.

All the *x*(*RE*)=0.25 samples exhibit CeO_2-like fluorite structure. Examples of *combined* refinements for NPD and XRPD patterns collected at *T* = 90 K are reported in the Appendix, Figs. A5.1-A5.5. No noteworthy residual is observed in any of the Rietveld refinements. The Ce/*RE* site occupations were fixed based on the nominal compositions. The same applies for the oxygen site, except for *RE* = Tb, where a higher site occupation is observed. In Fig. 5.8 the plot of the cell parameters as a function of the ionic radius, considering 7-fold coordination, is reported. The same trend is observed when 8-fold coordination is

considered. The cell parameters vary linearly with the ionic radii, except for Tb. This could be ascribed to the presence of both Tb^{+3} and Tb^{+4} species, as reported XANES measurements [*Martìnez-Arias et al., 2005*].

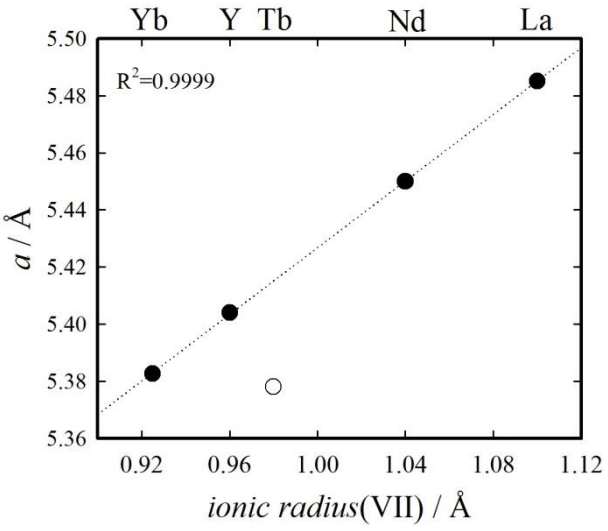

Fig. 5.8. Cell parameters as a function of the RE^{+3} ionic radius. Error bars are obscured by data markers.

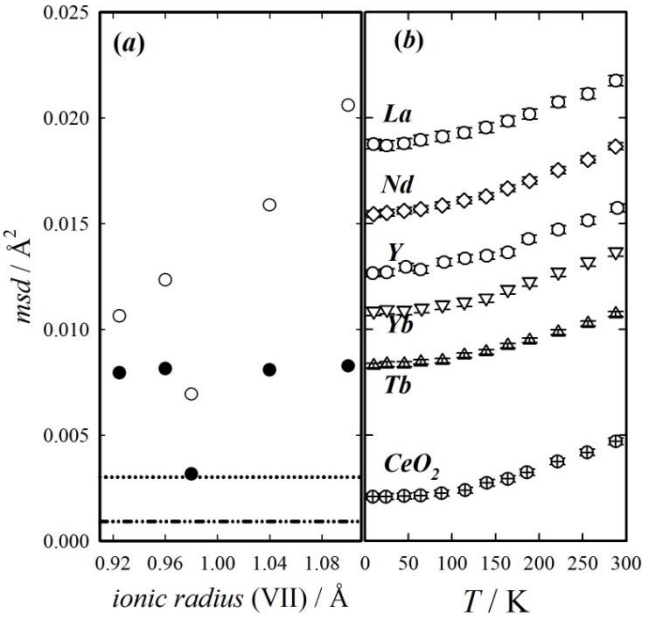

Fig. 5.9. (a) *msd* for cations (full circles) and anions (empty circles) obtained through *combined* XRPD and NPD refinements at T=90K. Cerium and Oxygen in CeO_2 are reported as a reference with a dashed and a dotted line, respectively. Error bars are obscured by data markers. (*b*) Oxygen NPD isotropic *msd* as a function of temperature.

Based on the linear regression in Fig. 5.8, the observed Tb-doped ceria cell parameter corresponds to the ionic radius 0.92 Å, which lies in between the Tb^{+3}(VII) and the Tb^{4+}(VIII) ionic radii (0.98 Å and 0.88 Å, respectively). By considering the interpolated Tb ionic radius (0.92 Å) as a combination of Tb^{+3}(VII) and Tb^{4+}(VIII), an average oxidation number of ~3.6 is obtained. Tb-doping in CeO_2 is reported to inhibit the formation of Ce^{+3}[*Martìnez-Arias et al., 2005*]. If Ce retains a +4 state and by considering an average $Tb^{+3.6}$ state, the overall O occupation fraction turns out to be 0.975, which is in agreement with that obtained through the XRPD and NPD *combined* Rietveld refinement (0.976(2)). By considering the general formula $Ce_{1-x}RE_xO_{2-x/2}$, the amount of vacancies in x(Tb)=0.25 is the same that would be introduced by a completely trivalent RE cation with concentration x(*RE*)=0.10.

The *msd* obtained through the *combined* XRPD and NPD refinements are shown in Fig. 5.9 (*a*); *msd* values for CeO_2 are also reported as a reference. For all *RE* ions except for *RE*=Tb, thermal parameters of cations (full circles) appear to change smoothly with the ionic radii. Conversely, O *msd* (empty circles) strongly increase by enhancing the ionic radius of the dopant. In Fig. 5.9 (*b*) the O *msd* observed through only NPD for all the investigated samples are shown. In all cases, doping causes a rigid shift of *msd* towards

higher values, thus indicating the presence of static disorder: atoms in different cells may occupy different positions. For *RE* = Tb, *msd* are smaller than those of other *RE* ions, thus indicating a lower amount of disorder, in accordance with the lower vacancy content.

As to PDF data, the direct analysis was applied to both XRPD and NPD datasets for 1st neighbors M-O and O-O. Its application to further distances becomes problematic because of the presence of overlapping peaks.

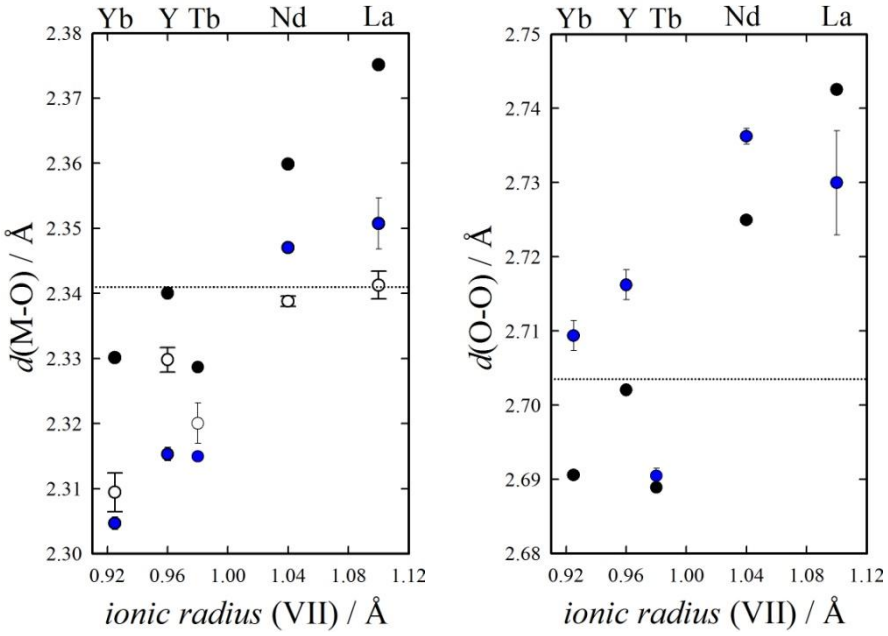

Fig. 5.10. M-O (*left*) and O-O (*right*) distances as determined through NPD (empty circles) and XRPD (black circles) direct analysis and through XRPD reciprocal space analysis (crossed circles). Dotted lines refer to the distance in CeO_2 as a reference.

Fig. 5.10 shows the interatomic distance values as determined by direct analysis of NPD (blue circles) and XRPD real space data (empty circles) and from XRPD reciprocal space analysis, as a reference (full circles) for the M-O (*left*) and O-O (*right*) pairs. Hereafter, reciprocal space data will be referred to as *average* data. The experimental G(*r*) curves are reported in Fig. 5.11 as empty circles (left hand side for NPD and right hand side for XRPD). The peaks were attributed to the corresponding atom pairs with reference to the CeO_2-like fluorite structure, as done in Fig. 5.6.

The first peak observed in both XRPD and NPD datasets at ~2.3 Å concerns M-O pairs. For all the investigated *RE*-doped samples, the M-O distance increases by enhancing the ionic radius, except for *RE* = Tb. All PDF data are consistent with the shrinking of the 1st M-O pair, confirming the XRPD results reported in chapter 4.

NPD distances, though, are not consistent with those detected through XRPD. This finding can be understood by considering the observed distances as an average over Ce-O and *RE*-O pairs, weighted on the scattering lengths of the elements involved. Indeed, as reported by EXAFS measurements, the Ce-O distance is observed to contract upon doping, even for large cations such as La^{+3} and Nd^{+3} [*Nitani et al., 2004*, *Deguchi et al., 2005*], while the trend of the *RE*-O distance depends on the single dopant. Let's consider, as an example, the case of *RE* = Y. Since XRPD data are more sensitive to Ce, while NPD data are more sensitive to Y, the shorter distance probed by NPD could indicate that the Y-O pairs are shorter than Ce-O. This finding is in agreement with EXAFS measurements [*Deguchi et al., 2005*] and theoretical calculations [*Hayashi et al., 2000*]. The same reasoning works out well for all the other *RE* dopants, even for *RE* = (Nd, La) which are characterized by longer *RE*-O distances than Ce-O [*Deguchi et al., 2005, Nitani et al., 2004*].

The second peak observed in NPD data at ~2.7 Å refers to O-O pairs. Due to the very low X-Ray scattering length of O, compared to that of cations, O-O pairs are not detectable through XRPD PDF. In Fig. 5.10 (*right*), NPD real space distances are thus compared with the *average* ones. In the fluorite structure, the O-O distance is just half of the cell parameter. Although *RE*=(Yb, Y) doping induces the contraction of the fluorite cell, the O-O pairs detected via direct analysis are larger than in ceria. For *RE* = Tb real and reciprocal space data give quite similar results, in agreement with a lower disorder. The O-O expansion is consistent with the oxygen relaxation around the vacancies. Indeed, considering an O vacancy at the center of a cube composed of O ions, when the six O nearest neighbors move towards the vacancy, the mean O-O distance increases. This effect will be discussed later on in detail.

An estimate of the spread of disorder is obtained by applying the long range *fluorite* structural model in different interatomic distance ranges. This procedure is generally referred to as "*r*-series refinement". XRPD patterns from ID31 were chosen for this purpose since they don't suffer from limited reciprocal space resolution effects [*Fitch, 2004*].

Table 5.2. Residuals R_w from the *r*-series refinements. The *r*-ranges are in Å units.

sample	1.5<r<10	5<r<15	10<r<20	20<r<30	30<r<40	40<r<50
RE=La	0.241	0.075	0.056	0.049	0.041	0.044
RE=Nd	0.213	0.081	0.082	0.061	0.048	0.057
RE=Tb	0.144	0.119	0.108	0.114	0.105	0.094
RE=Y	0.166	0.105	0.091	0.096	0.073	0.089
RE=Yb	0.170	0.098	0.108	0.094	0.085	0.109
CeO_2	0.111	0.094	0.084	0.087	0.087	0.068

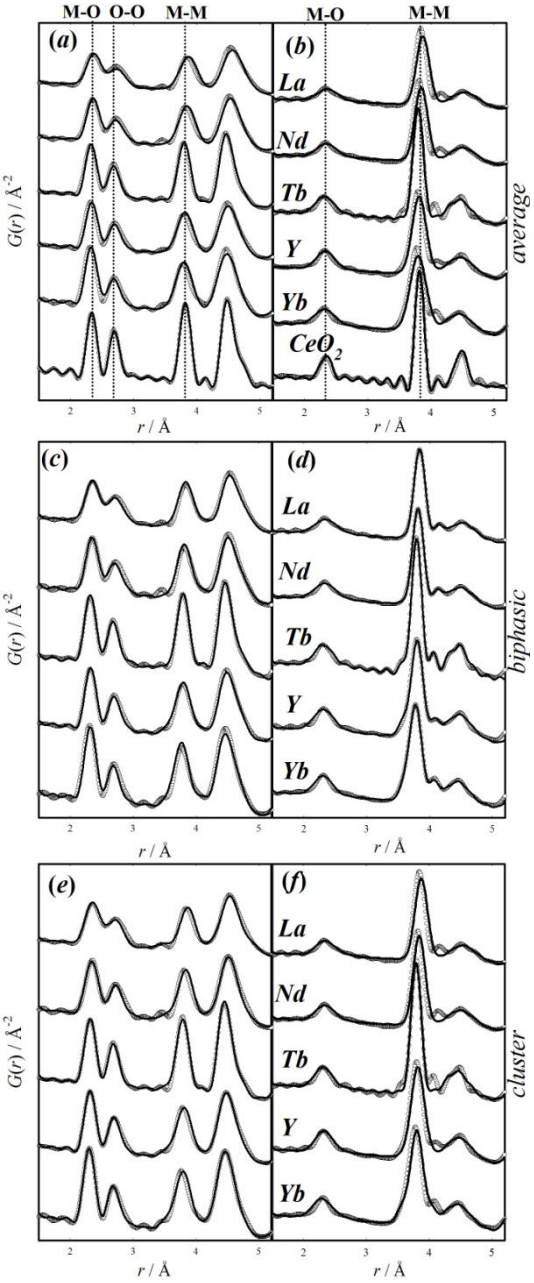

Fig 5.11. Short range real space refinements in the 1.5<*r*<5.2 Å range. Empty circles: observed G(*r*); black line: calculated. (*a*), (*c*) and (*e*) stand for NPD data; (*b*), (*d*) and (*f*) stand for XRPD data. (*a*) and (*b*) indicate the *average* model, (*c*) and (*d*) the *biphasic* model, (*e*) and (*f*) the *cluster* model. R_w residuals are listed in Table 5.4.

tested and discussed.

Conversely, oscillations in NPD G(*r*) curves are subjected to damping with increasing *r*, due to the lower resolution of the D4c instrument. The fits are found to become worse for r < ~10 Å, except for pure CeO_2, while for higher *r*-values the fits are rather good. Low residuals are observed also for *RE* = Tb. The fit residuals are reported in Table 5.2.In Fig. 5.11 the refinements of the average *fluorite* model are shown against NPD (*a*) and XRPD (*b*) data in the 1.5<*r*<5.2 Å range. As to the first coordination shells, the *average* model is clearly poor for all the doped samples: the short range structure in doped ceria differs from the average fluorite structure regardless of the dopant. Similarly to the XRPD PDF shown in the previous chapter, the fit of low-*r* interatomic distances is principally made poor by the incorrect description of the M-M pairs, especially the peak C. All the above findings indicate two concomitant mechanisms of local scale ordering: on the one hand, based on metal *Amsd* and on the occurrence of the PDF peak C, a C-type ordering could be expected; on the other hand the oxygen *Amsd* and the increase of the mean O-O distance probed by PDF suggest that locally O ions are attracted by the O vacancies. In the following the two models will be

5.4.1. Modeling

We saw in chapter 4 that the occurrence of peak C in long range fluorite samples is an evidence that locally the atomic arrangement differs from that of fluorite. The normalized area of the peak C was then investigated over the whole compositional range of the solid solutions to determine its evolution with doping. The same procedure can be applied to samples sharing the same dopant concentration, but with a different dopant ion.

Table 5.3. Normalized area of the peak C detected through XRPD, compared to the C-type fraction and the x(*RE*2) coordinated detected employing the biphasic model..

	Tb	*Yb*	*Y*	*Gd*	*Sm*	*Nd*	*La*
$A_C/(A_B+A_C)$	0.060(6)	0.106(7)	0.083(5)	0.106(7)	0.109(2)	0.099(8)	0.107(1)
C-frac	0.221(2)	0.305(3)	0.259(2)	0.199(1)	0.225(3)	0.239(3)	0.245(3)
x(*RE2*)	-0.0250(1)	-0.0288(1)	-0.0282(1)	-0.0262(3)	-0.0264(4)	-0.0257(2)	-0.0249(2)

The area of the peak C, normalized to the sum of peak C and B, is reported in Table 5.3 for all the dopants investigated. Since this peak is clearly observed only in XRPD data, *RE* = Gd and Sm were also included. With the exception of *RE* = Tb, the lowest normalized intensity of the peak C is recorded for *RE* = Y. By recalling that the area of a XRPD PDF peak, considering the same multiplicity, is proportional to the number of electrons of the elements involved in the pair, the lowest intensity determined with *RE* = Y is a further evidence that the *RE* dopant contribute to this peak.

The peak C can be then deemed as a fingerprint of disorder in all doped ceria materials regardless of the dopant involved. It is worth noting that the peak C in the PDF curves is not the only deviation from a well ordered fluorite atomic arrangement. In Fig 5.12 the direct analysis fits on XRPD (*a*) and NPD (*b*) data are shown for the *x*(La)=0.25 sample. It is evident that some bumps in the PDF are also observed for the 1st M-O pairs. These findings are consistent with NPD results, but due to the lower real space resolution of the d4c instrument, coupled to the large neutron scattering length of O, a contribution to the PDF at ~4.1 Å is evident, but not resolved from the adjacent large peak accounting for the 2nd M-O pair.

The presence of the peak C was successfully modeled in chapter 4 by introducing the *biphasic* model. It is equivalent to supposing that *RE* and Ce ions retain the local structure of the pure oxides. The refinements were performed in two steps: a limited number of parameters were *first* refined against the NPD G(*r*) curves to accurately determine the O-related parameters, *then* against XRPD G(*r*) curves keeping fixed the O site coordinates.

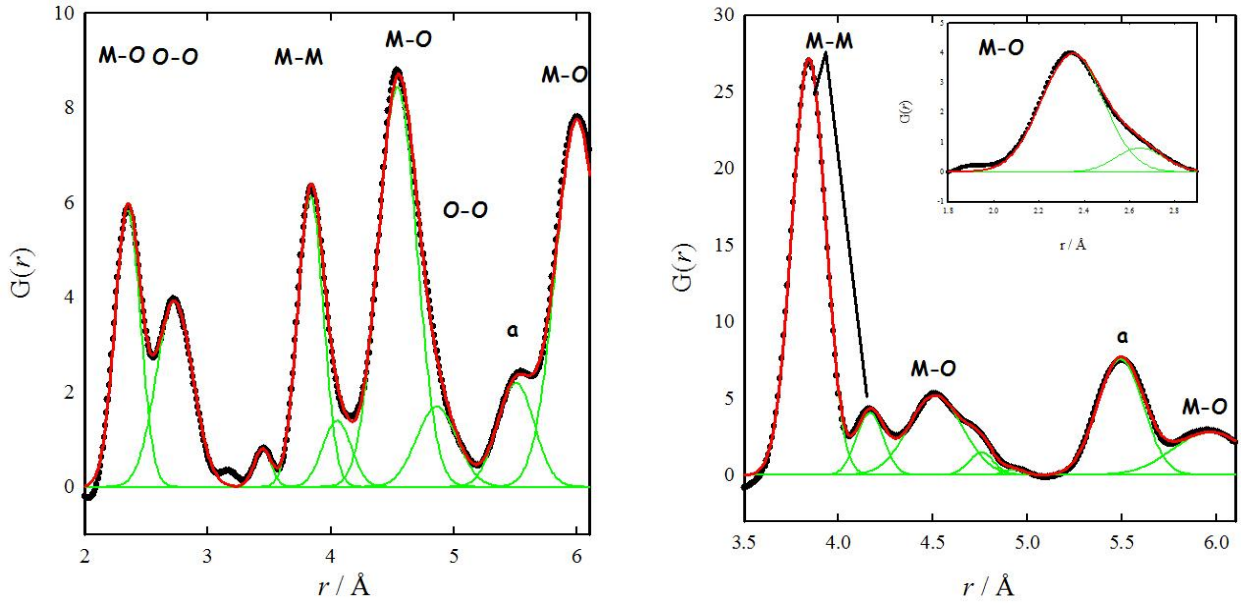

Fig. 5.12. Direct analysis of the NPD (left) and XRPD (right) G(*r*) for *RE*=La. Black dots: observed G(*r*); green solid line: calculated single Gaussian; red solid line: total calculated (sum of all the Gaussians). Labels indicate which couple of atoms contribute to the main G(*r*) peaks. In the inset of XRPD the nearest neighbor M-O distance is highlighted. A high-*r* anisotropy is clearly evident.

In Fig. 5.11 the fits of the *biphasic* model are shown against NPD (*c*) and XRPD (*d*) data. When the results of the NPD *biphasic* model are applied to the XRPD G(*r*) curves, the peak C is well fitted. As stated above, Nd_2O_3 and La_2O_3 are also reported to exhibit hexagonal A-type structure. However, the *biphasic* model involving A-type hexagonal structure fits poor the experimental G(*r*), especially against NPD data. The *biphasic* model works well with all the considered *RE* dopants.

A further structural information from the present model can be gained by considering the fraction of C-type phase and the *x*(*RE*2) coordinate. Note that here we refer to *RE*2 instead of M2, since the C-type phase is supposed to be in its pure form, thus only *RE* ions are present. C-type fraction and *x*(M2) are reported in Table 5.3, together with the normalized area of the peak C. The former is also plotted in Fig. 5.13 as a function of the ionic radius of the dopant.

The C-type fraction varies with the ionic radius of the dopant, the minimum corresponding to Gd and Sm doping, which in turn are the dopants that guarantee the best performance in a SOFC. A correlation is then observed between the local structure and the transport properties of doped ceria. When the dopant (thus the vacancies) is randomly dispersed into the ceria lattice, oxygen vacancies are easily available for O migration. Conversely, when O vacancies form clusters or any kind of aggregate, an additive contribution to the activation energy of O migration is provided. This produces the damping of ionic conductivity, especially when a larger part of the sample exhibits locally C-type structure.

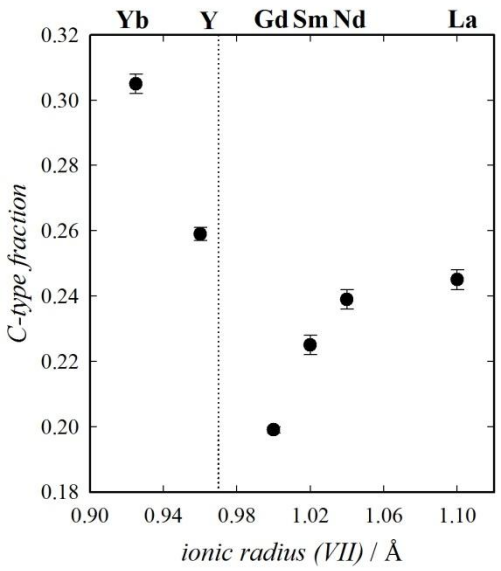

Fig. 5.13. C-type fraction as determined after refinements of XRPD PDF in the 1.5 < *r* < 5.2 Å range employing the *biphasic* model.

Also the *x*(*RE*2) coordinate was observed to depend on the size of the dopant. We saw in chapter 4 that a smaller (less negative) value of *x*(*RE*2), compared to the one of the pure oxide, indicates a non zero occupation of the O2 site. *x*(M2) becomes less negative by changing the dopant across the lanthanide series from Yb to La, thus indicating enhanced affinity of larger dopants for O ions.

This partially goes in the direction of the results of theoretical calculations [*Minervini et al., 1999*, *Andersson et al., 2006*] that suggested that large dopants prefer a second neighbor position with respect to the vacancy. This condition implies a 8-fold coordinated *RE* ion, which was not observed in any of the above EXAFS reports. We can say rather that all the dopants share a similar local structure. However, at fixed doping concentration, the larger the dopant, the larger the amount of oxygen vacancies surrounded by Ce ions.

Another remark is due about the meaning of *x*(M2). A larger (more negative) value implies that the structure of the dopant-rich droplets resembles the one of pure C-type, while a value close to zero indicates a distorted fluorite-like structure. By increasing doping concentration from fluorite to C-type, *x*(M2) becomes more negative up to the formation of C-type phase.

Our data show that when the *x*(M2) coordinate is close to the value of pure C-type (in general ~ -0.03), a transition from fluorite to C-type is likely to occur by slightly increasing the dopant concentration. For example, since *x*(La2) is ~0.024, far from its limit value (-0.030) [*Hirosaki et al., 2003*], a large amount of dopant can be introduced into the structure before reaching the *x*(*RE*) solubility limit in fluorite. This is in keeping with the average structure observed when *x*(RE)=0.50.

Indeed, even for 50% dopant concentration, La-doped ceria exhibits fluorite structure. For Nd doping, which has a slightly larger value of *x*(M2), a C-type structure with broad superstructure peaks is observed. Following this trend, Sm, Gd and Y have C-type structure, with Sm having the larger solubility limit. Finally, Yb produces different C-type phases.

Table 5.4. Residuals of the real space refinements in the 1.5<r<5.2 Å range with the different models involved.

RE	*average*		*cluster*		*biphasic*	
	XRPD	NPD	XRPD	NPD	XRPD	NPD
Yb	0.246	0.202	0.209	0.102	0.076	0.163
Y	0.225	0.191	0.200	0.103	0.113	0.128
Tb	0.152	0.116	0.136	0.075	0.076	0.096
Nd	0.302	0.178	0.235	0.118	0.067	0.146
La	0.304	0.209	0.280	0.153	0.068	0.172

An alternative model to describe the local structure is to consider vacancy-dopants clusters (hereafter *cluster* model). The *cluster* model is schematically drawn in Fig. 5.14. A fluorite cell with the origin shifted in (¼ , ¼ , ¼), i.e. the O site, is considered. When a vacancy is introduced into the cell, the adjacent O ions relax towards the vacancy along the <100> direction.

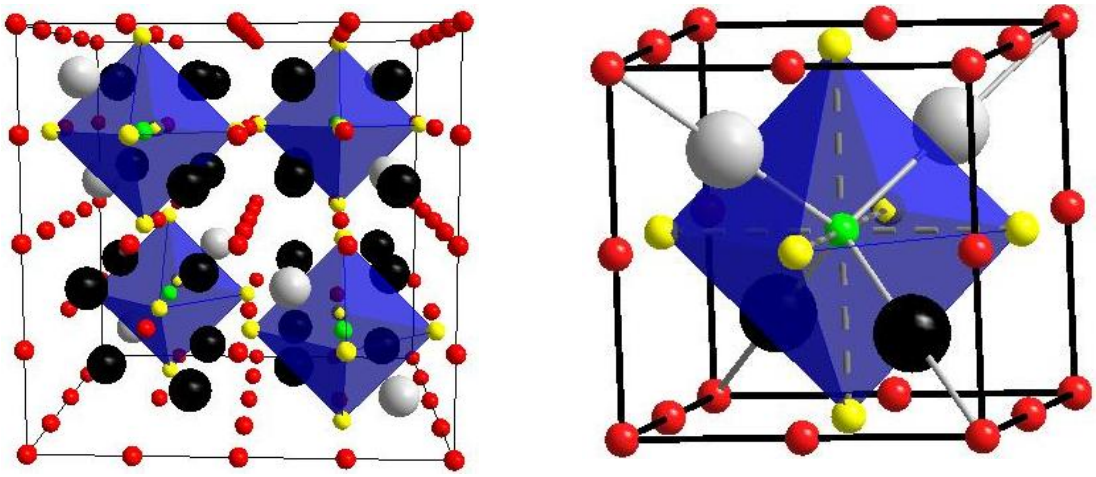

Fig. 5.14. Description of the *cluster* model. Grey: *RE*, black: Ce, red: O, yellow: relaxed O, green: O vacancy. The O vacancy lies in the center of the cell. O ions relax towards the vacancy along the <100> direction (dashed lines) and cations move along the <111> direction (solid lines).

At the same time, the cations coordinated to the vacancy move, to a lesser extent, along the <111> direction. The x=0.25 composition is achieved by introducing 8 *RE* doping ions for Ce and 4 O vacancies in a 2a x 2a x 2a supercell, where a is the fluorite cell parameter. In this way every vacancy is surrounded by two *RE* ions and all dopant ions gain a 7-fold coordination. Every cluster of atoms surrounding a vacancy is not affected by other vacancies and can be considered to be independent of the others. The *cluster* model was first applied to NPD G(r) curves, which are more sensitive to O contribution. In Fig. 5.11 (*e*) the fit of the *cluster* model against NPD G(r) curves is shown. When compared to the *fluorite* (Fig. 5.11 (*a*)) and *biphasic* (Fig. 5.11 (*c*) models the fit strongly improves, particularly in the case of O-related distances. The only r-region which is not well fitted is around 3-4 Å, where M-M pairs are expected. The results of the NPD fits were then applied to XRPD G(r) curves, which are far more sensitive to cations, but the related fit appears to be rather poor, as

shown in Fig. 5.11 (*f*). This implies that the description of M arrangement through this model is too simplistic. The results are then discussed only with reference to the O-related distances.

Indeed we were able to correctly fit the distances involving O ions only employing the *cluster* model. When O ions move towards the vacancy, the distance between the relaxed and the other O ions increase. In Fig. 5.14 this corresponds to the distance between red (unrelaxed) and yellow (relaxed) balls. This can explain the elongation of the O-O pairs observed even when the long range cell parameter contacts, which is the case of *RE*= Yb and Y. Nevertheless the O-O peaks become anisotropic towards higher r-values. This could be related to a weaker relaxation of O-O second neighbors towards the vacancy along the <110> direction, which is neglected in the *cluster* model for sake of simplicity. Very good fits are obtained by adding only two parameters to the *fluorite* model. We did not add further parameters to avoid correlations. In addition to that, one should consider that the approximation underlying the *cluster* model, that is that oxygen ions are not affected by more than one vacancy, is valid only up to the *x*(*RE*)=0.25 limit concentration. For larger doping concentration, some O ions are forced to have two O vacancies in the first O coordination shell. Still for the *x*(*RE*)=0.25 composition, implementing a second order O relaxation is not possible, since each one of the O ions not involved in the relaxation process (red balls in Fig 5.14) is shared by two different oxygen vacancies. On the other hand, by introducing a smaller amount of doping, the induced disorder is limited and difficult to be appreciated with the present NPD data.

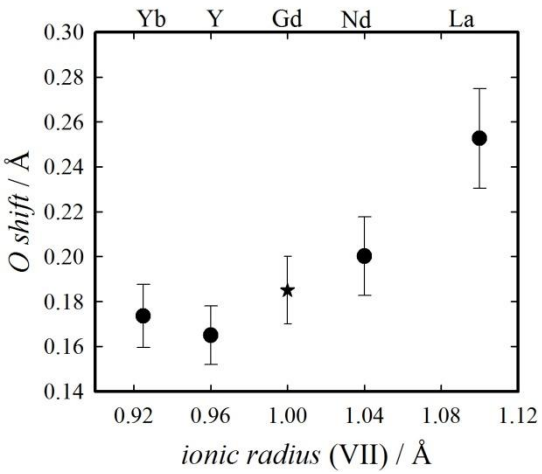

Fig. 5.15. O shift induced by the vacancy as a function of the ionic radius of the dopant. Circles: Measured samples. Star: Calculated *RE*=Gd from [**51**].

The *cluster* model works better for smaller cations, while for *RE*=Nd and particularly *RE*=La it performs less satisfactorily. The residuals of the short range PDF fits for all the models proposed are listed in Table 5.4. It should be noted that this model describes well the electrostatic dopants-vacancy interaction, but neglects any strain effect induced by the size mismatch between host and dopant cations, except the overall cell parameter. The latter is found to be quite close to the average value for all the *RE* dopants. Finally, the magnitude of the O shift from its average crystallographic position appears to be strongly dependent on the size of the dopant. In Fig. 5.15 the magnitude of the O shifts are plotted as a

function of the ionic radius of the dopant. The larger the size mismatch with the host Ce site, the greater the induced O shift. Apart from *RE* = Tb, not shown here, the smallest shift among the investigated samples is observed for *RE* = Y, which guarantees, according to literature reports, the best performance in fuel cell devices among the dopants subjected to NPD. A similar O shift (~0.17-0.20 Å) was determined for *RE* = Gd via DFT calculations [*Dholabhai et al., 2010*]. The main limitation of the *cluster* model approach is that it poorly describe the disorder on cation sites, thus missing the peak C observed in XRPD data.

Finally, a remark is due about the experimental condition of the present investigation. A low temperature was chosen to get rid of strong thermal broadening effects which would occur at high temperatures. In this way a fingerprint of disorder was observed. This does not imply, though, that the same local structure is retained at high temperature. In the next chapter we try to fill the gap between the investigations reported so far, performed at low temperature and the real operating conditions of a fuel cell device.

5.5. Conclusions

In this chapter we have shown that NPD allows to access complementary structural information to XRPD, especially regarding O-related parameters. *RE*-O distances were found to be different from Ce-O, while the study of O-O pairs highlights the attraction exerted by O vacancies to the nearby O ions.

Different dopants affect in a very similar way the local structure of cerium oxide. Different probes, though, give apparently contradictory indication on the way the local structure rearranges after doping.

XRPD PDF data can be correctly interpreted only considering the presence of dopant-rich droplets, the structure of which resembles that of the C-type form of the pure RE_2O_3, embedded in a fluorite-like matrix.

NPD PDF data were better described considering O relaxations towards the vacancy.

Both models propose an explanation of the different performance of the dopants. After NPD PDF, different dopants induce a different distortion on O sites, which in turn lies at the basis of the observed conductivity. XRPD PDF data probe instead a different spread of the dopant rich droplets. In both cases, dopants having a larger size mismatch with respect to the host Ce^{+4} ion, affect to a larger extent the original structure of CeO_2. This distortion is probed either as an O relaxation process or a complex cation ordering.

Actually the two models can be considered as two pictures of the same object, taken with different magnifications. If one focuses on the O local distortions, then misses the more complex metal rearrangement. On the other hand, an accurate description of metal distribution would lose the details of O disorder.

References

[*Andersson et al., 2006*] D. A. Andersson, S. I. Simak, N. V. Skorodumova, I. A. Abrikosov, B. Johansson, *PNAS* 2006, **103**, 3518–352.

[*Coduri et al., 2012*] M. Coduri, M. Scavini, M. Allieta, M. Brunelli and C. Ferrero, *Journal of Physics: Conference Series* 2012, **340**, 012056.

[*Coduri et al., 2012b*] M. Coduri, M. Brunelli, M. Scavini, M. Allieta, P. Masala, L.Capogna, H.E. Fischer and C. Ferrero, *Zeitschrift für Kristallographie* 2012, **227**, 272-279.

[*Deguchi et al., 2005*] H. Deguchi, H. Yoshida, T. Inagaki and M. Horiuchi *Solid State Ionics* 2005, 176, 1817-1825

[*Dholabhai et al., 2010*] P. P. Dholabhai, J. B. Adams., P. Crozier and R. Sharma, *Phys. Chem. Chem. Phys.* 2010, **12**, 7904-7910.

[*Faber et al., 1989*] J. Faber, C. Geoffroy, A. Roux, A. Sylvestre, and P. Abelard, *Appl. Phys.* 1989, **A49**, 225-232.

[*Fitch, 2004*] A. N. Fitch, *J. Res. Natl. Inst. Stand. Technol.* 2004, **109**, 133-142.

[*Hayashi et al., 2000*] H. Hayashi, R. Sagawa, H. Inaba and K. Kawamura, *Solid State Ionics* 2000, **131**, 281-290.

[*Heinmaa et al., 2010*] I. Heinmaa, T. Joon, H. Kooskora, J. Pahapill and J. Subbi, *Solid State Ionics* 2010, **181**, 1309-1315.

[*Hirosaki et al., 2003*] N. Hirosaki, S. Ogata and C. Kocer, *Journal of Alloys and Compounds* 2003, **351**, 31–34.

[*Jung et al., 2002*] G. B. Jung, T. J., Huang and C. L. Chang. *Journal of the Electrochemical Society* 2002, **6**, 225-230.

[*Kilner, 2008*] J. A. Kilner, *Chemistry Letters* 2008, **37**, 1012-1015.

[*Kim and Stebbins, 2007*] N. Kim and J. F. Stebbins, *Chem. Mater* 2007, **19**, 5742-5747.

[*Martìnez-Arias et al., 2005*] A. Martìnez-Arias, A. B. Hungrìa, M. Fernàndez-Garcìa, A. Iglesias-Juez, J. C. Conesa, G. C. Mather and G. Munuera, *Journal of Power Sources* 2005, **151**, 43-51.

[*Minervini et al., 1999*] L. Minervini, M. O. Zacate and R. W. Grimes, *Solid State Ionics* 1999, **116**, 339-349.

[*Mori and Drennan, 2003*] T. Mori and J. Drennan, *J Electroceram* **2006**, *17*, 749–757.

[*Neder et al., 1992*] R. B. Neder, F. Frey and H. Schulz, *Acta Cryst.*, 1990, **A46**, 799-809.

[*Nitani et al., 2004*] H. Nitani, T. Nakagawa, M. Yamanouchi, T. Osuki, M. Yuya and T. A. Yamamoto, *Materials Letters* 2004, **58**, 2076-2081.

[*Ohashi et al., 1998*] T. Ohashi, S. Yamazaki, T. Tokunaga, Y. Arita, T. Matsui, T. Harami and K. *Solid State Ionics* 1998, **113-115**, 559–564.

[*Ou et al., 2006a*] D. R. Ou, T. Mori, F. Ye, M. Takahashi, J. Zou and J. Drennan, *Acta Materialia* 2006, **54**, 3737-3746.

[*Ou et al., 2006b*] D. R. Ou, T. Mori, F. Ye and T. Kobayashi, *Appl. Phys. Lett.* 2006, **89**, 171911.

[*Ou et al., 2008*] D. R. Ou, T. Mori, F. Ye, J. Zou, G. Auchterlonie, and J. Drennan, *Phisical Review B* 2008, **77**, 024108

[*Sears, 2006*] V. F. Sears, *Neutron News* 1992, **3**, 26-37.

[*Shannon, 1976*] R. D. Shannon, *Acta Cryst.* 1976,**A32**, 751-767.

[*Yamazaki et al., 2000*] S. Yamazaki, T. Matsui, T. Ohashi and Y. Arita, *Solid State Ionics* 2000, **136-137**, 913-920.

[*Ye et al., 2009*] F. Ye, T. Mori, D. R. Ou and A. N. Cormack, *Solid State Ionics* 2009, **180**, 1127-1132.

[*Zhang et al., 2004*] T. S. Zhang, J. Ma, L. B. Kong, S. H. Chan and J. A. Kilner, *Solid State Ionics* 2004, **170**, 209–217.

6. Doped ceria under fuel cell operating conditions

6.1. Introduction

The fluorite structure of cerium oxide is stable over a large oxygen non-stoichiometry δ, that is it can afford the presence of high amount of oxygen vacancies. These can be induced either thermally

$$O_O \leftrightarrows \frac{1}{2}O_2 + V_O^{\cdot\cdot} + 2e' \quad (6.1)$$

or by doping with a lower valent cation. In the case of a trivalent cation *RE*, the dopant substitutes for the host Ce^{+4} ions and ionic conductivity occurs by oxygen diffusion through the doping-induced oxygen vacancies:

$$RE_2O_3 \xrightarrow{CeO_2} 2RE'_{Ce} + 3O_O^x + V_O^{\cdot\cdot} \quad (6.2)$$

In spite of the high temperature required for achieving suitable ionic conductivity, most of literature reports are performed at low temperature. In general this is due to i) the need for complex experimental setups for high temperature measurements and ii) the damping of diffraction signal at high temperature. However, the local structure under fuel cells' operating conditions may strongly differ from the one observed at low temperature. For example, pure CeO_2 is reported to undergo cubic to lower symmetry phases transition by increasing oxygen the non-stoichiometry δ in $CeO_{2-\delta}$ under δ=0.178 [*Kümmerle and Heger, 1999*]. For this reasons, we decided to perform a comprehensive crystallographic study of doped ceria under operating conditions. We chose lanthanum as a dopant, since among the lanthanide series, it guarantees the larger size mismatch with the host Ce^{+4} ion [*Shannon, 1976*]. This is expected to highlight the doping induced disorder, particularly in terms of interatomic distances.

The average structure was investigated by collecting NPD patterns over a wide *T* range, in order to evaluate the high temperature stability of the fluorite structure and to perform a comprehensive crystallographic study. NPD is particularly suitable for this task, since the O neutron scattering length is similar to that of Ce (see chapters 2 and 5), while using XRPD the diffracted intensity is dominated by Ce(La) contributions.

In the case of doped ceria electrolytes, the data collection under a controlled atmosphere is of utmost importance since the stability under both oxidizing and reducing atmospheres is an essential requirement for candidates for solid electrolyte materials. In order to simulate the fuel cells' operating conditions, we performed a PDF study under both static air and a H_2/Ar mixture. Details are reported in the experimental section. In this case XRPD was preferred to NPD because of the large incoherent neutron cross section of Hydrogen.

In the following, after the description of experimental setups and data collection strategy, the results of the reciprocal space analysis will be *first* reported and *then* discussed in the framework of the PDF analysis.

6.2. Experimental section

A $Ce_{0.75}La_{0.25}O_{1.875}$ sample was prepared after the *Pechini* sol-gel method and fired at 900°C for 72 hours.

NPD patterns for reciprocal space analysis were collected at the D20 instrument of the ILL, Grenoble at an incident neutron wavelength λ=1.3593 Å in the $13<2\theta<130°$ 2θ range. The samples were loaded in a vanadium can of ~7 mm diameter. About 15 minutes acquisition time diffraction patterns were collected every ~50°C, warming the samples from room temperature (RT) up to about 850°C using a furnace. The same data collection strategy was applied to a CeO_2 (≥99.0%) sample purchased by Aldrich.

XRPD patterns for PDF analysis were collected at the ID11 beamline of the ESRF, Grenoble using a CCD (FReLoN) camera placed perpendicular to the incident beam 110 mm behind the sample. Data were collected at an incident X-ray wavelength λ=0.1232 Å reaching Q_{max} = 30 $Å^{-1}$. The powdered samples were loaded in a quartz capillary of 0.6 mm diameter mounted on a gas rig cell. The samples were heated with a hot blower furnace. Further details about the sample environment are reported elsewhere [*Brunelli and Fitch, 2003*].

The empty quartz capillary was measured in order to properly subtract the background. Frames were integrated over 20 minutes to improve statistical significance. Owing to the low thermal expansion of quartz, we recorded data at RT and considered negligible any modification with temperature. To properly subtract the background, dark current was collected on the detector between measurements.

A $Ce_{0.75}La_{0.25}O_{1.875}$ sample was measured in static air from 50°C up to 750°C with a 2°C/min ramp, and then cooled down to RT. Another $Ce_{0.75}La_{0.25}O_{1.875}$ sample from the same batch was measured under reducing

atmosphere, using a H_2(7%)/Ar mixture. The gas mixture was not fluxed continuously into the cell, but rather it filled the capillary at ~10 bar pressure; it was purged and refilled every 30 minutes, that is about 12 times upon warming. The sample was warmed from 50°C up to 750°C with a 2°C/min ramp. Once reached T=750°C, the temperature has been kept fixed for 3 hours. Hereafter, the $Ce_{0.75}La_{0.25}O_{1.875}$ samples will be referred to as La25air and La25H2, for data collected under air and reducing atmosphere, respectively. A CeO_2 sample was measured in static air at RT and then while warming from 450°C to 750°C at 3°C/min.

For all the samples, frames were recorded every 10 seconds and then merged together every 5 acquisitions, for 50 seconds total exposure time, corresponding to about 1 °C temperature variation.

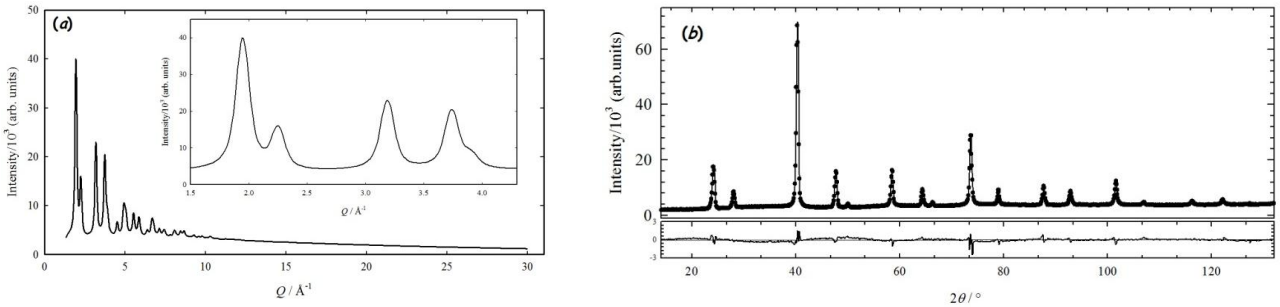

Fig. 6.1. (*a*) XRPD pattern collected at T = 750 °C at ID11 for La25H2. In the inset the low Q region is highlighted. (*b*) NPD Rietveld refinement of La25air collected at T = 750°C. Points: experimental data; solid line: calculated based on a fluorite model. Note that the difference curve in the lower panel is magnified.

6.3. Reciprocal space analysis

The XRPD frames collected at ID11 were processed using the software fit2D [*Hammersley et al., 1996*] to produce intensity against 2θ patterns. The CCD camera was placed close to the sample to increase the investigated angular range (i.e. Q_{max}) at the expense of the angular resolution. An example of a pattern collected at T=750°C on La25H2 is shown in Fig. 6.1 (*a*). No superstructure peaks, fingerprint of lower symmetry, are detected. However, they can be easily too broad to be observed, by reason of the low resolution.

In order to deepen the average structure investigation, we decided to use higher resolution diffraction data suitable to perform Rietveld refinements. The La25air sample exhibits CeO_2-like fluorite structure over the whole investigated temperature range. In Fig. 6.1 (*b*) the refinement of La25air is shown. No noteworthy residual is observed. The Ce/La site occupation was fixed on the base of the nominal compositions. In Fig. 6.2 (*a*) the *msd* observed for La25air are plotted as a function of temperature and compared to the ones of pure CeO_2, taken as a reference.

As discussed in chapter 2, the static contribution to the thermal parameter can be quantified by subtracting the *msd* of undoped ceria to the overall *msd* observed for the doped samples [*Argyriou, 1994*, *Scavini et al., 2010*], provided that pure CeO_2 is free of disorder. In particular, the static disorder was 0.0063(3) $Å^2$ and 0.0176(6) $Å^2$ for metal (henceforth M) and O sites respectively. This in turn corresponds to a mean doping-induced atomic shift position of 0.079(8) Å for M and 0.132(12) Å for O. The disorder on O site is almost double than the one on metal site.

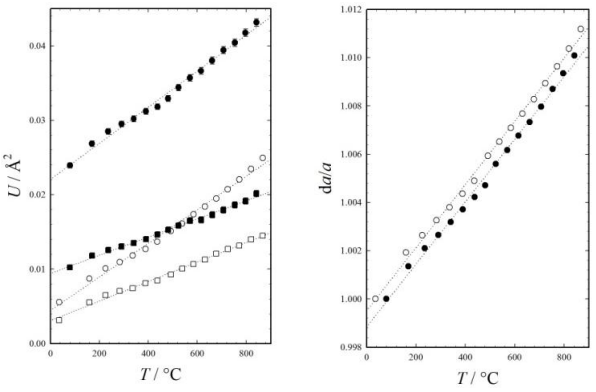

Fig. 6.2. (*a*) *msd* related cations (empty symbols) and anions (full symbols) for CeO_2 (squares) and La25air (circles) determined through NPD Rietveld refinements in the RT < *T* < 850°C range. Error bars are obscured by data markers. (*b*) Cell parameter variation as a function of temperature for CeO_2 (empty circles) and La25air (full circles).

In Fig. 6.2 (*b*) the cell parameter evolution as a function of temperature is displayed. The linear thermal expansion coefficients *a*, expressed as:

$$\frac{dL}{L} = a_0 + aT \qquad (6.3)$$

were calculated to be used as a reference later on in this work. In equation 6.3 L is the cell parameter determined experimentally. We calculated a linear coefficient of 1.31(2) x 10^5 for pure CeO_2, similar to the value reported in [*Chavan and Tyagi, 2005*] and 1.29(3) x 10^5 for La25air. The reciprocal space analysis showed that the fluorite structure of $Ce_{0.75}La_{0.25}O_{1.875}$ is stable even at high temperature and under reducing atmosphere. In the following, we will investigate whether the fluorite structure is retained at the local scale and how the local structure evolves as a function of temperature and under controlled atmosphere.

6.4. Real space analysis

XRPD real space data were processed using PDFgetX3 [*Billinge and Farrow, 2012*] in the 1.4 < *Q* < 27 $Å^{-1}$ range. The G(*r*) curves were calibrated to correct for an aberration that produces an increasing shift of peak positions with the interatomic distance *r*. Details are reported in the Appendix, section A6.1. The calibrated G(*r*) curves are plotted in Fig. 6.3. At a first glance, one can observe that the broadening of the first peak with temperature is not accompanied by the increase of its *r*-position. In other words, it does not expand with temperature. In order to gain insight into this phenomenon, we decided to monitor the thermal expansion of different atom pairs, with particular reference to the comparison between doped samples.

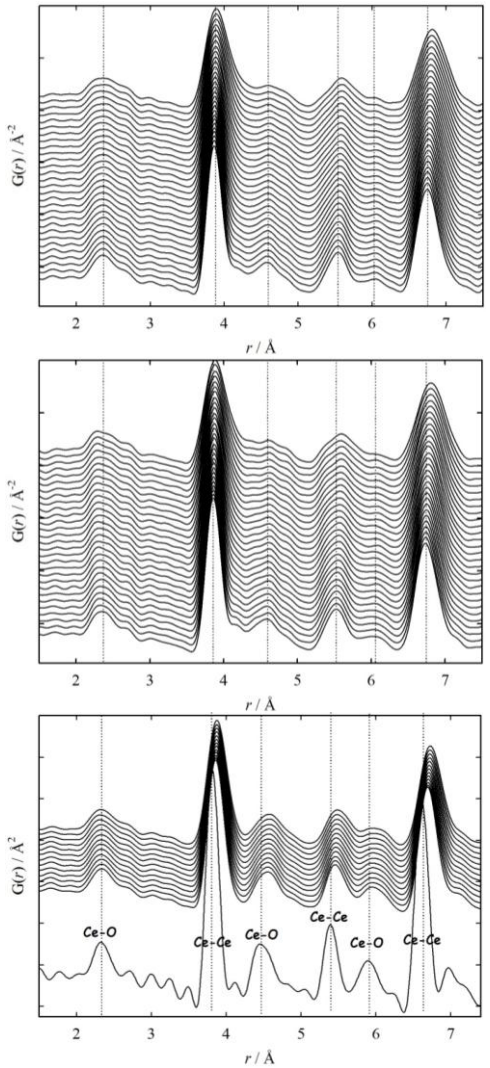

Fig. 6.3. G(*r*) curves for La25air (top), La25H2 (middle) and CeO_2 (bottom) every 25°C from the lower collected temperature (bottom, see experimental section) to 750°C (top). Dotted lines are a guide to the eye and indicate the peak *r*-position at the lowest temperature. In the bottom panel, the atom pairs contributing to each peak in pure CeO_2 are indicated, with reference to the G(*r*) collected at RT.

In principle, the peak position should be determined by fitting a G(*r*) peak with a convolution between a Gaussian function (which accounts for the thermal vibration of the atoms involved) and a *sinc* function, arising from the truncation of the Fourier summation [*Toby and Egami 1992*]. The latter gives rise to ringing on both sides of the G(*r*) peaks, especially at low *r*-values. The amplitude of the ripples reduces by increasing the Debye-Waller factor at a given Q_{max} [*Toby and Egami 1992*]. For this reason, some ripples are well apparent in the RT PDF of pure CeO_2, whilst they strongly reduce at high temperature. As reported later on in this work, some G(*r*) peaks feature anisotropies which make unsuitable a Gaussian fit. For this reason, here we define the peak position as the *r*-value corresponding to the maximum intensity of a peak. In this way the peak positions can be readily determined for a number of G(*r*) curves, even in case of strongly asymmetric peaks.

In the following, the temperature evolution of the first G(*r*) peaks will be discussed, together with deviations from a Gaussian distribution of distances.

6.4.1. Thermal expansion

1st M-O pair. Let's consider the first peak in the G(*r*) curves, corresponding to the M-O first neighbours. In pure ceria at RT a single, fairly symmetric peak is observed, whilst a high-*r* shoulder (~2.65 Å) appears at higher temperatures. A wrong subtraction of the quartz capillary contribution would result in peaks at ~1.65 Å and 3.10 Å, corresponding to Si-O and Si-Si distances, respectively; but no contribution is expected around 2.6 Å. The presence of ripples should in principle be discarded, since their magnitude decreases with Debye-Waller, that is with temperature, whereas the relative intensity of the hump increases with temperature, the opposite expected for a termination ripple. We thus propose to tentatively assign this

shoulder to Ce(III)-O pairs. We cannot exclude, though, the presence of a small ripple contribution, which could affect the actual position of the shoulder. Anyhow, it is clear that even in pure CeO_2 the temperature produces some local distortions. Based on equation 6.1, oxygen vacancies are expected to be introduced into the fluorite structure upon heating. As discussed in chapter 5, this is reported to trigger the relaxation of adjacent oxygen ions, which in turn results in the shrinking of the average M-O distance and in the expansion of the O-O one. This is also consistent with the results reported in chapter 5 of the present thesis. Hence we propose that the shrinking with temperature of the 1st neighbor Ce-O pair in CeO_2 is consistent with the introduction of oxygen vacancies into the fluorite structure. As to the doped samples, a high-*r* shoulder is observed even at low temperature. Since in doped samples the reduction of Ce^{+4} to Ce^{+3} is unlikely to happen at low temperature, this shoulder was attributed to La-O pairs, which are supposed to be larger than Ce(IV)-O by virtue of the different ionic radius of the cations. It should be noted that this shoulder was also observed on data collected at T = 90 K on La-doped ceria (see chapter 5, Fig 5.14). The temperature evolution of the M-O distance is displayed in Fig. 6.4 (*a*), (*d*) and (*g*) for La25air, La25H2 and CeO_2, respectively. For La25air, the peak remains symmetric (except for the above mentioned shoulder) and the *r*-position does not change much with temperature. The shrinking observed in pure CeO_2 does not occur. Indeed in heavy doped samples, the equilibrium 6.1 is expected to be shifted leftwards and a smaller amount of vacancies is created. The shrinking induced by the oxygen vacancies is counterbalanced by thermal expansion. Compared to ambient conditions, when $Ce_{0.75}La_{0.25}O_{1.875}$ is annealed under reducing atmosphere, further O vacancies are introduced. The first peak splits with temperature into two (plus the shoulder), the highest intensity corresponding to the shorter distance contribution. As a result of the split, the *r*-value corresponding to the maximum intensity is observed to reduce with temperature. An overview of the peak position evolution of doped samples is given in the panel (*a*) of Fig. 6.5. The data are much scattered, particularly at high temperature, due the very large broadening of the peak, which is probably the result of a wide distribution of interatomic distances. In order to reduce the data dispersion observed in Fig. 6.5 (*a*), we multiplied the S(*Q*) function with a modification function, as proposed in [*Lorch, 1969*]. This facilitates the high-*Q* normalization of S(*Q*) and minimizes the possible contribution of ripples, at the expense of an additional peak broadening. The corresponding peak positions collected every 50°C are plotted in the inset of Fig. 6.5 (*a*).

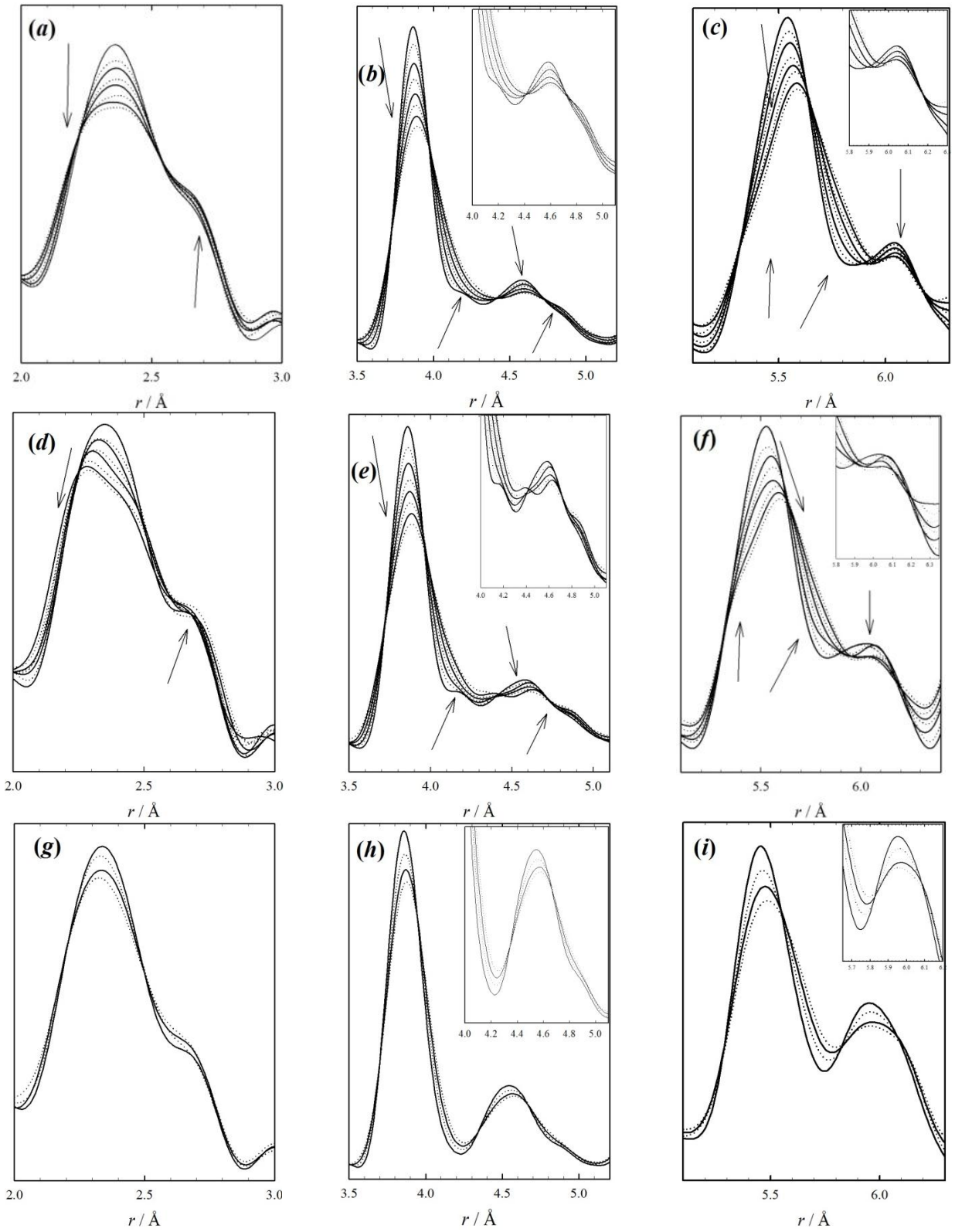

Fig. 6.4. G(*r*) curves for La25air (*a*), (*b*) and (*c*); La25H2 (*d*), (*e*) and (*f*) and CeO2 (*g*), (*h*) and (*i*) collected every 100°C and referring to different *r*-ranges. Arrows indicate variations of peak position with increasing temperature.

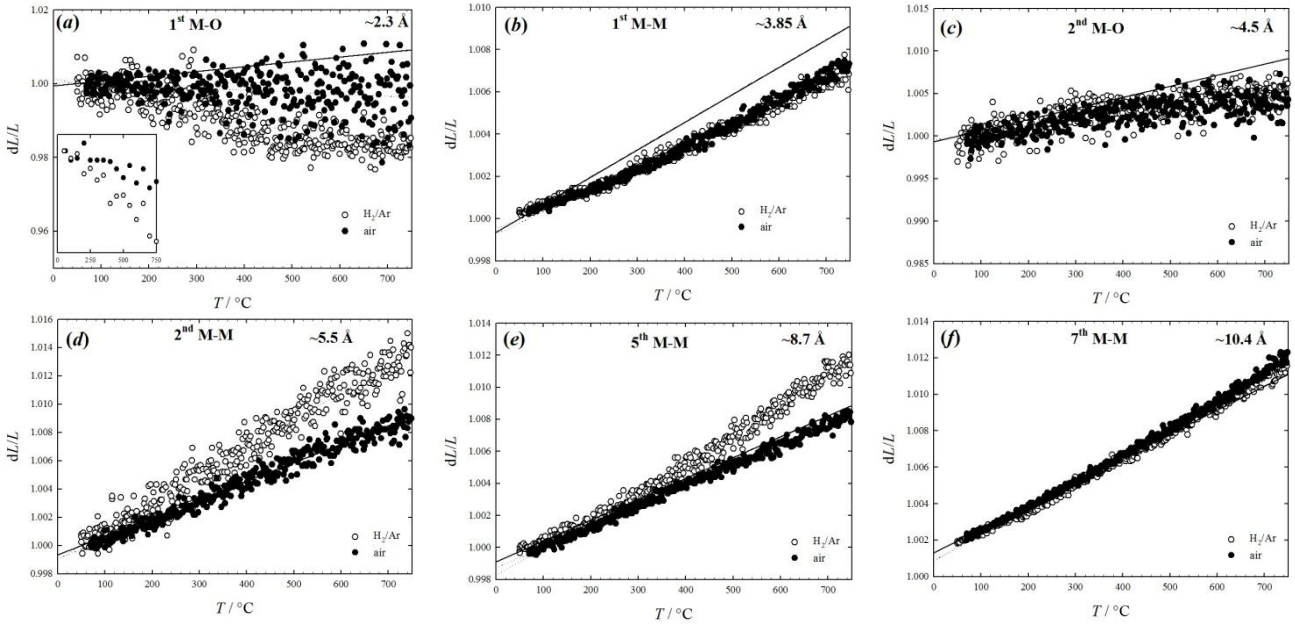

Fig. 6.5. *r*-position corresponding to the maximum intensity of different G(*r*) peaks as a function of temperature. Full circles: La25air; empty circles: La25H2; solid line: thermal expansion determined via reciprocal space analysis. The atom pair to which every peak is referred to is indicated in each panel, together with a rough estimate of the low temperature distance.

The M-O *r*-position is confirmed to be almost unaffected by temperature for La25air, whereas when collecting data under reducing atmosphere it clearly shrinks.

1st M-M and 2nd M-O pairs. The second and third peaks observed in the G(*r*) curves concern nearest neighbor M-M pairs and next nearest neighbors M-O pairs, respectively. Their temperature evolution is displayed in Fig. 6.4 (*b*), (*e*) and (*h*). A high-*r* shoulder is again observed aside both peaks. The one around 4.2 Å is evident only at low temperature, whilst it is no more resolved with increasing temperature. This could be due to either dynamical effects or a broader distance distribution. This peak was assigned in the previous chapters to a M-M pair, corresponding to a larger distance of a C-type structure. The main M-M peak is not particularly affected by reduction, whereas a wider distribution of distances is observed for the M-O peak. In particular, for La25H2 a peak at ~4.4 Å is resolved at around T = 650°C, but it is no more evident at higher temperature. In Fig. 6.5 (*b*) and (*c*) the corresponding peak positions trend with temperature are reported. Both trends are very similar and looked almost superimposed, within the limit of data dispersion. The thermal expansion is much smaller compared to that of the average structure. For M-O this is true particularly from ~400°C on, for both datasets.

The 2nd neighbor M-M pairs G(*r*) peaks, together with the 3rd neighbor M-O pairs are plotted in panels (*c*), (*f*) and (*i*) of Fig. 6.4. As for the data collected in air, heating causes the broadening of the peaks and no noteworthy anisotropy is observed. This is not the case of the La25H2 sample: the M-M peak, which

corresponds to two M^{+3} ions at the vertexes of the fluorite cell, gains a strong anisotropy character, consistent with the presence of two distinct contributions. Something similar is observed even for the 3rd M-O neighbor. This rebounds on the temperature evolution of the 2nd M-M peak position, displayed in panel (*d*) of Fig. 6.5.

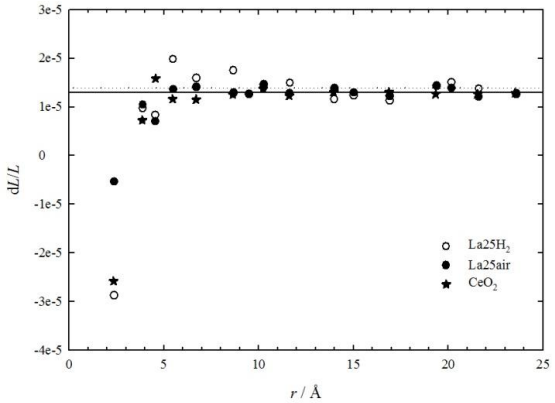

Fig. 6.6. Thermal expansion as a function of the interatomic distance *r* as determined by PDF analysis. Stars: CeO_2, empty circles: La25H2, full circles: La25air. Dotted and solid lines indicate the thermal expansion derived from the average structure for CeO_2 and $Ce_{0.75}La_{0.25}O_{1.875}$, respectively.

Whereas La25air shares the same trend as the average structure, it is clear that La25H2 strongly deviates, as a result of a more complex cations distribution. The corresponding M-O peak position is not plotted in Fig. 6.5 because at high temperature the peak transforms into a shoulder of the adjacent M-M signal: no peak position is obtainable with the present method. In order to confirm that a reducing atmosphere enlarges disorder, in panels (*e*) and (*f*) of Fig. 6.5 the thermal expansion derived from PDF analysis is shown for larger interatomic distances, i.e. for the peaks at ~8.5 and ~10 Å. These can be assigned to the 5th and 7th M-M pairs, respectively; although both peaks have satellites corresponding to M-O pairs. Whereas for the La25air sample the thermal expansion is consistent with the average one, under reducing atmosphere the peak at ~8.5 Å has a very similar behavior to the peak at ~5.5 Å. It is worth noting that in both cases the deviations arise above *T*~400°C. A similar effect is observed for the 2nd M-O pair, where both doped specimens deviate from the trend of the average structure. The differences between La25air and La25H2 reduce while increasing *r* and after 10 Å (Fig. 6.5 (*f*)) the data collected under different atmospheres look similar. The linear thermal expansion of the PDF peaks is plotted in Fig. 6.6 as a function of the interatomic distance *r*. In the limit of large *r* interatomic distances, the peak thermal expansions tend to the value observed for the average structure. This confirms that PDF data were properly calibrated and suggests that a deviation from the thermal expansion of the average structure can be deemed as a fingerprint of disorder. Some disorder, probably arising from thermally induced oxygen vacancies, is present even in pure CeO_2, but it is basically limited to the first Ce-O coordination shell. It is clear from Fig. 6.5 and 6.6 that both doped specimens share a similar dependence with temperature within ~5 Å. The deviation from the trend of average structure reflects the distortion of the first coordination shells. For further interatomic distances, large deviations are registered for La25H2 up to ~10 Å, whilst La25air is consistent with the trend of the

average structure. With reference to Fig. 6.6, we should remind that here the peak position is referred to the *r*-interatomic distance corresponding to the maximum intensity. If the peak position, then, is the same as expected by average structure, it does not necessarily imply that no disorder is present, but rather that the induced distortion does not affect the maximum intensity of the peak. Thus disorder spreads at least to 5 Å for La25air and to 10 Å for La25H2. This will be thoroughly investigated in the next section, placing emphasis on deviations from a Gaussian distribution of interatomic distances.

6.4.2. Short range modeling

The above results reflect the presence of short range deviations from a fluorite structure. Such deviations are expressed in terms of unexpected or anisotropic peaks. The generally employed method to verify whether a structural model is apt to describe PDF data is the real space refinement.

As a first attempt, a fluorite model was refined against the G(*r*) curves, by varying the cell parameter, an overall scale factor, metal and oxygen *msd* and a parameter accounting for correlated motion. Five parameters in all. Dealing with high temperature PDF, the broadening of G(*r*) peaks improves the fit quality, particularly in doped samples. The list of residual R_W related to refinements in the $1.5 < r < 6$ Å range is reported in Table 6.1. In the previous chapters local deviations from a fluorite atomic arrangement were monitored through the evolution, in terms of peak position and area, of the peak C. This was done first as a function of the dopant concentration (chapter 4), then with the ionic radii (chapter 5). Unfortunately at high temperature the peak C is no more resolved: a different procedure is then required. Here we propose to highlight the deviations from the fluorite structure by superposing Gaussian functions to the experimental G(*r*) curves.

Table 6.1. Residuals Rw for the refinements performed employing the *fluorite* model. See the main text for further details

T / °C	***CeO_2***	***La25air***	***La25H2***
50	-	0.153	0.146
150	-	0.151	0.148
250	-	0.146	0.146
350	-	0.144	0.140
450	0.127	0.139	0.139
550	0.122	0.139	0.136
650	0.122	0.135	0.141
750	0.118	0.134	0.142

A Gaussian function is considered for each expected peak foreseen by a fluorite structure. In principle, this is similar to performing a real space refinement, except that every peak is considered separately from each other, without any constrain deriving from a structural model. The Gaussian functions are not fitted to the experimental data, but rather they are a guide to the eye for highlighting the reliability of a fluorite structural model. The results of this approach are reported in Fig. 6.7 in the $3.5 < r < 6.3$ Å range, considering datasets collected at 50 (RT for CeO_2), 450 and 750°C. The $5 < r < 6.3$ Å region is magnified to help the reader examining the details. The contribution of O-O pairs is considered negligible.

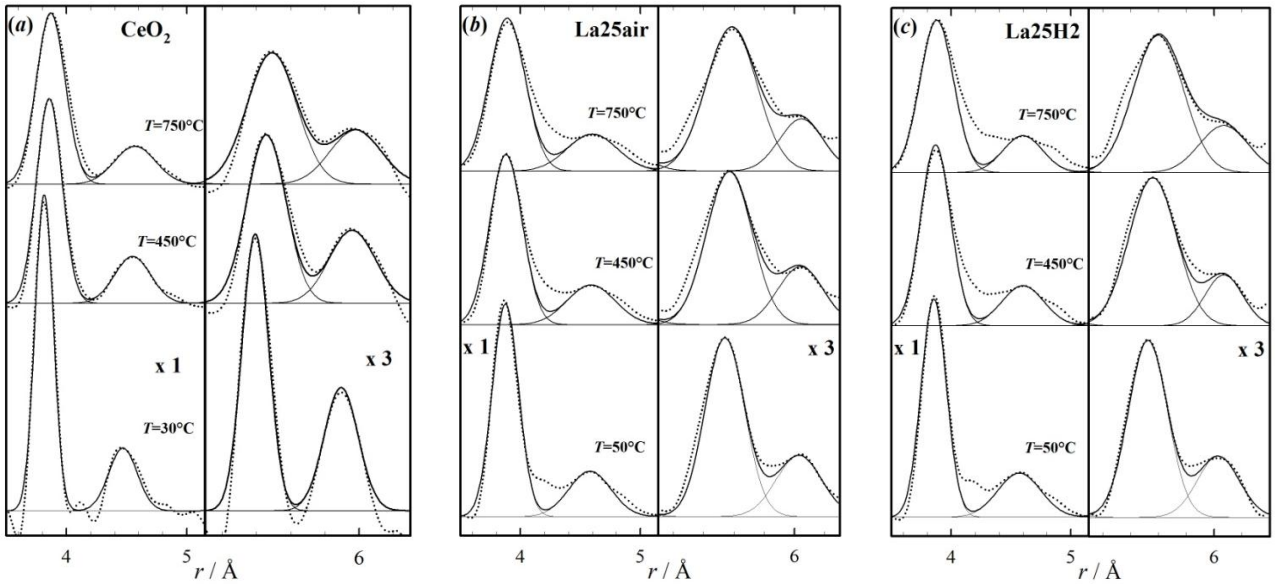

Fig. 6.7. G(*r*) curves related to pure CeO_2 (*a*), La25air (*b*) and La25H2 (*c*) at low temperature (different for each sample) and then at 450 and 750°C. Dots: experimental G(*r*) curves, light solid lines: Gaussian functions; bold solid lines: sum of Gaussian functions. The $5<r<6.4$ Å range is magnified (x3) in order to highlight details.

The first M-O G(*r*) peak is not reported here since it is clear from Fig. 6.4 (*a*-*b*) that, being a doublet, it is not consistent with a fluorite structure. The Gaussian fits to CeO_2 G(*r*) curves are shown in the panel (*a*) of Fig. 6.7. Apart some ripples at RT, the G(*r*) peaks are consistent with the fluorite model. Some high-*r* tails differ from the Gaussian distribution, but we cannot state that this is due to some local ordering, rather than residual ripples.

Let's now face the case of La-doped samples, displayed in panels (*b*) and (*c*) of Fig. 6.7 for La25air and La25H2, respectively. In both cases, at low temperature a peak not foreseen by the fluorite distance distribution is evident at around 4.2 Å. Although it becomes unresolved when heating, a contribution to the G(*r*) curve not consistent with a fluorite structure is retained even at high temperature. Similar deviations, though to a lesser extent, are observed even for the other peaks. In particular, a high *r*-shoulder appears for

the 2nd neighbor M-O peak (~4.55 Å) and it increases with temperature. This effect is larger under reducing atmosphere. The same applies to the low *r*-shoulder of the 2nd M-M neighbors and, to a lesser extent, to its high-*r* shoulder. The large anisotropy of the peaks seems to indicate that all the M-O and M-M pairs affected by disorder split at least into three different interatomic distances, that is one smaller and one larger with respect to the average one. Further *r*-interatomic distances were not investigated, because of peak overlaps. It is worth noting that even the 2nd M-M peak of La25air at high temperature has a clear low-*r* anisotropy, thus indicating the contributions of different atom pairs not foreseen in the reference fluorite structure. This effect is smaller than under reducing atmosphere and was not detected when monitoring the peak position as a function of temperature. Disorder in La25air is not limited within 5 Å.

The above approach makes clear that the *fluorite* model is unsuitable to describe the local structure of doped ceria even at high temperature. The PDF refinements performed with the *fluorite* model are shown in Fig 6.8 for La25air (*a*) and La25H2 (*b*). It is clear that the at low temperature the model is wrong, whilst it is more difficult, at a first glance, to verify the quality of the fit at high temperature.

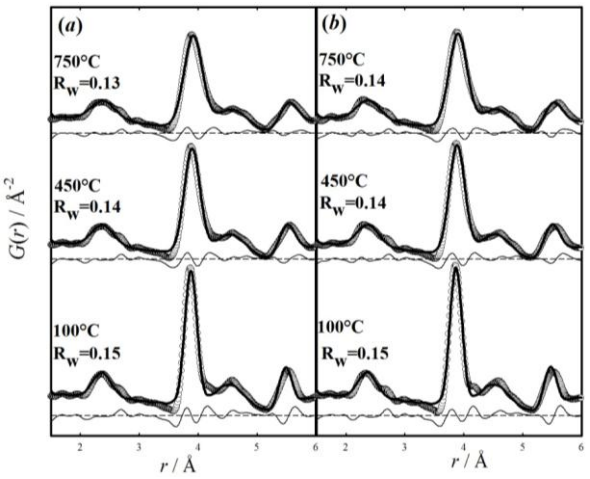

Fig. 6.8. *Fluorite* model applied to (*a*) La25air and (*b*) La25H2 at *T*= 100, 450 and 750°C. Empty circles: observed G(*r*) curves, solid line: calculated. The residual (calculated - observed) is reported below each curve.

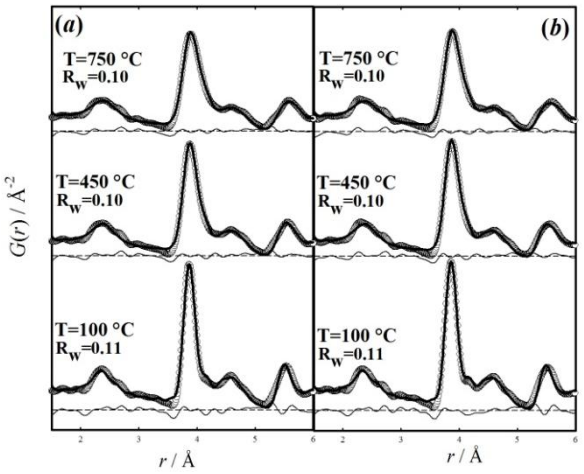

Fig. 6.9. *Biphasic* model applied to (*a*) La25air and (*b*) La25H2 at *T*= 100, 450 and 750°C. Empty circles: observed G(*r*) curves, solid line: calculated. The residual (calculated - observed) is reported below each curve.

Based on the satisfying results obtained in low temperature investigations, in the following the *biphasic* model will be tested against the doped samples G(*r*) at different temperatures. The refinements were performed in the $1.5 < r < 6$ Å range, i.e. by considering the first five atom pairs (O-O pairs excluded) foreseen by an undistorted fluorite structure. These are the pairs mostly affected by disorder, as highlighted in Figs. 6.4 and 6.5. Since the real space refinements are carried out on a limited *r* range, the number of independent data points is small. As a consequence, in order to avoid parameters correlation, the number of

refined parameters should be reduced as much as possible. To this purpose, on a first stage we decided to refine an overall scale factor, two cell parameters for fluorite and C-type phases, an overall thermal parameter for cations and another one for oxygen ions, the *x* coordinate of the La2 C-type cation site and a parameter accounting for correlated motion. Seven parameters were in all refined, against five for the *fluorite* model. Owing to the low contribution of O ions to the XRPD G(*r*), the O site in C-type was kept fixed to the position occupied in the fluorite structure (0.375, 0.125, 0.375). It should be noted that even fixing the O coordinates to the values of the pure C-type form, the residual R_w are basically the same. This approximation is needed in order to reduce the total number of parameters It implies that disorder on oxygen site is accounted for only by an overall thermal parameter. Compared to fluorite, the number of M-O pairs increases reflecting the distribution of cation sites. This is, though, a very poor approximation of the real oxygen distribution and the results of the *biphasic* model will be discussed only in terms of cation displacements.

The fits of the *biphasic* model against the G(*r*) curves are reported in Fig. 6.9 for La25air (*a*) and La25H2 (*b*) and can be compared to the application of the fluorite model, reported in Fig. 6.8. At low temperature, the *biphasic* model clearly improves the fit of G(*r*) curves, particularly for M-M pairs, the contribution at ~4.2 Å included. Conversely, the *fluorite* model fails.

By increasing temperature, some fine features are lost: the peak broadening improves the fit quality of the *fluorite* model, but it is still wrong even at high temperature, because, as discussed in the main text (see Fig. 6.7), a G(*r*) contribution, hidden by an excessive peak broadening, is still present. Moreover, a closer look to Fig. 6.8 would reveal that the main M-M peak at ~3.8 Å is poorly fitted. This confirms that the dopant retains its chemical environment even at high temperature.

The C-type phase fraction for the two doped samples is reported in Table 6.2 together with the *x* coordinate of La2 site in C-type and the residual R_W. In Table 6.2, it is evident that the *estimated standard deviations* (*esd*) of the refined parameters are quite high. This could arise from unreliable *esd* extracted when processing data from a 2D detector. To support this finding, the refinement of the same structural model against the PDF collected on the very same sample (the same shown in chapter 5) at T = 90 K with a point detector provided no evident correlation between parameters. At high temperature, though, larger

correlations can easily occur because of peak broadenings. Anyhow, in the following we will mostly refer to the trends of the refined parameters, rather than their absolute values.

Table 6.2. Results of the refinements performed with a *biphasic* model.

T/°C	*C-type fraction*		*x(M2)*		R_W	
	air	***H_2***	***air***	***H_2***	***air***	***H_2***
100	**0.25(8)**	**0.22(8)**	**-0.0185(56)**	**-0.0199(58)**	**0.108**	**0.109**
150	**0.25(9)**	**0.24(9)**	**-0.0184(58)**	**-0.0181(62)**	**0.108**	**0.108**
200	**0.27(12)**	**0.23(9)**	**-0.0168(62)**	**-0.0191(64)**	**0.106**	**0.105**
250	**0.29(15)**	**0.26(12)**	**-0.0158(64)**	**-0.0170(65)**	**0.105**	**0.107**
300	**0.31(16)**	**0.29(16)**	**-0.0154(64)**	**-0.0155(67)**	**0.104**	**0.107**
350	**0.36(19)**	**0.29(17)**	**-0.0136(55)**	**-0.0156(70)**	**0.102**	**0.107**
400	**0.37(21)**	**0.36(19)**	**-0.0139(57)**	**-0.0134(55)**	**0.100**	**0.106**
450	**0.37(22)**	**0.39(20)**	**-0.0141(60)**	**-0.0129(50)**	**0.099**	**0.101**
500	**0.41(23)**	**0.39(21)**	**-0.0134(54)**	**-0.0128(51)**	**0.098**	**0.103**
550	**0.42(24)**	**0.43(20)**	**-0.0137(55)**	**-0.0122(44)**	**0.098**	**0.100**
600	**0.42(24)**	**0.42(21)**	**-0.0136(55)**	**-0.0122(47)**	**0.098**	**0.101**
650	**0.42(25)**	**0.43(22)**	**-0.0139(59)**	**-0.0133(51)**	**0.096**	**0.104**
700	**0.43(25)**	**0.44(22)**	**-0.0140(60)**	**-0.0134(53)**	**0.096**	**0.106**
750	**0.44(27)**	**0.45(22)**	**-0.0144(63)**	**-0.0134(53)**	**0.097**	**0.104**

6.4.3. Effect of temperature

The C-type phase fraction is ~0.25 (0.245(3) at T = 90 K), then it increases with temperature and reaches ~0.45 at T=750°C for both specimens. At the same time the x(La2) coordinate decreases from ~0.019-0.020 to 0.013-0.014. This is consistent with the x(La2) = -0.0249(2) observed at T=90 K.

The role of the C-type phase in the fit is to account for any deviations from a fluorite arrangement: C-type fraction and x(La2) are related to the asymmetries, which increase with temperature, observed in M-M distances. Rather than a true chemical separation between pure lanthanum- and cerium oxides, the biphasic model should be envisaged after a crystallographic point of view. Vacancy-rich droplets arrange with a C-type structure, while vacancy-poor regions retain a fluorite structure. Thus the increase in C-type does not, obviously, correspond to the increase of the La_2O_3 fraction, but rather to the spread of cations having C-type-

like ordering. On one hand, our biphasic model assumes that the two phases are in their pure chemical form. If, as indicated by the intermediate *x*(La2), they contain a fraction of dopant, that is La in CeO_2 and Ce in La_2O_3, this is expected to produce further distortions in the phases. Such distortions were neglected within the present model in order to reduce the number of parameters. On the other hand, by increasing temperature, oxygen vacancies could be produced and/or redistributed between the two phases, at least on a nanometric scale. This is highlighted by the less negative value of *x*(La2), that implies a larger content of O ions into the C-type local arrangements.

6.4.4. Effect of reduction

Being aware of the large uncertainties of the refined parameters, the C-type phase fractions observed for La25air and La25H2 are basically the same. This is in contrast with the apparent larger amount of oxygen vacancies introduced into La25H2, which results from i) the larger induced distortion compared to La25air (see Figs. 6.4-6.6) and ii) the shrink induced on the 1st M-O distance with temperature, which is only partially observed in La25air. Although we cannot exclude that a non negligible amount of oxygen vacancies form in La25air at high temperature; according to equation 6.1 we expect their concentration to be much smaller than in La25H2, as suggested by conductivity measurements [*Shimonosono et al., 2005*]. Moreover, at low $p(O_2)$ the reduction of Ce^{+4} to Ce^{+3} is reported to be favored in doped samples, particularly in the case of large dopants [*Balducci et al., 2003*]. In Y-doped samples the effective Ce reduction under flowing hydrogen was observed at ~500°C [*Li et al., 2011*] through EELS spectra. The different trends of PDF thermal expansion observed between the two doped samples above *T*~450°C could be then ascribed to Ce reduction. Moreover, the similar ionic radii of Ce^{+3} (1.01 Å) and La^{+3} (1.03 Å) in 6-fold coordination [*Shannon, 1976*] make reliable their coexistence in a C-type phase.

We have to remind the reader, though, that dealing with X-rays the results obtained in the present study are mostly sensitive to cation displacements. On the other hand, oxygen vacancies are expected to directly affect O ions, whilst the disorder on cation site, as described in the reciprocal space analysis section, is much smaller. This is consistent with Fig. 6.5 (*a-b*): the different atmosphere strongly affects the 1st M-O pair, whilst the temperature trend of the 1st M-M neighbor is basically the same. The effect of reducing atmosphere is more evident for larger interatomic distances, that is between 5 and 10 Å. In particular, the 2nd

M-M neighbor at around 5.5 Å is clearly affected by the controlled atmosphere. Unfortunately, it is characterized by a lower multiplicity than the 1st M-M peak, thus featuring a less intensity and a lower contribution to the refined parameters. The *biphasic* model is not particularly sensitive to the differences induced by the controlled atmosphere, whilst it probes easily the effect of temperature.

A final remark is due on the experimental conditions employed to guarantee a reducing atmosphere. The reader could argue that the reducing conditions were too mild to effectively reduce the sample. When taking the powder off the capillary, we observed that it was black, confirming that Ce reduction occurred, at least on the surface. This was not the case of the La25air powder.

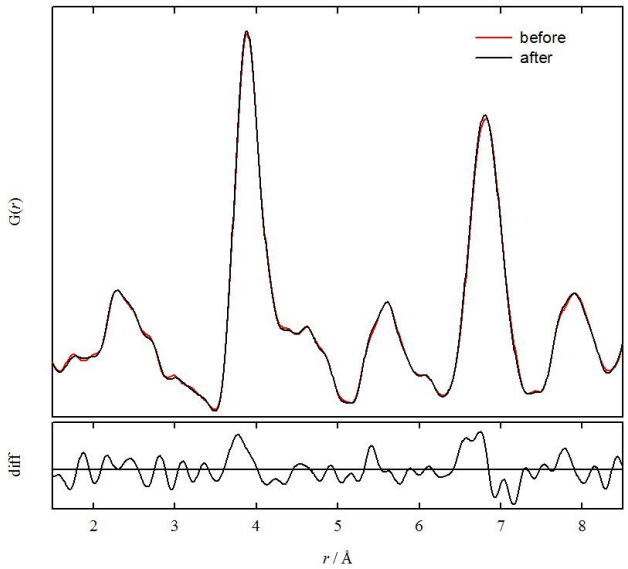

Fig. 6.10. Comparisons between PDF collected on La25H2 before (red) and after (black) 3 hours at *T*=750°C. Below: magnified (x4) difference curve. Positive not random difference observed before each of the M-M distances (~3.7, ~5.4, ~6.6 and ~7.9 Å).

In view of the above results, it is evident that the local structure further distorts under the effect of reducing atmosphere. Both doped samples feature similar deviations from the fluorite structure, the magnitude of the distortion being larger under reducing atmosphere. This could be probably ascribed to a larger amount of oxygen vacancies. The ageing of La25H2 at 750°C for 3 hours under H_2/Ar did not modify the average structure of the sample, at least within the resolution limit of the XRPD pattern. As to the local structure, the G(*r*) curves collected before and after the 3 hours ageing process at *T*=750°C are very similar. Small not random differences are detected in the low-*r* part of the M-M G(*r*) peaks, as shown in the magnified bottom panel of Fig. 6.10. However, the G(*r*) curves look almost superimposed, to testify that the local structure does not further distort by ageing in reducing atmosphere. We thus demonstrated that the fluorite structure of $Ce_{0.75}La_{0.25}O_{1.875}$ is stable up to *T* = 750°C even under reducing atmosphere. Distortions are induced by doping into the fluorite structure and are retained over temperature. The effect of the reducing atmosphere is then to amplify the magnitude of local distortions, without affecting the long range fluorite ordering. The main limit of the *biphasic* model is the neglect of any O ordering. Both the need of reducing the number of parameters and the low X-ray scattering power of O compared to lanthanides make unreliable the study of O

displacements with the present data. Nevertheless, we plan to gain further insights into the high temperature oxygen orderings in doped ceria, through a NPD experiment already scheduled at the D4c instrument of the ILL.

6.5. Conclusions

In this chapter we provided a thorough investigation of the local structure evolution of La-doped ceria in fuel cells' operating conditions. The fluorite structure of La doped ceria is retained at high temperature, and within the resolution of our data, even under reducing atmosphere. A strong doping induced disorder is observed on both metal and oxygen sites, the latter being almost double after NPD measurements. This affects the local scale, which becomes different from that of fluorite. The magnitude of such distortions, expressed in terms of unexpected or anisotropy PDF peaks, is larger under reducing atmosphere. This effect could be ascribed to Ce reduction, which could induce the degradation of SOFC performance. The extent of the distortions is as large as 1 nm and does not affect the long range fluorite ordering. Such distortion cannot be accounted for by simple dopant-vacancy-dopant clusters. Confirming the results of low temperature investigations, we were able to fit the PDF curves considering Ce and La cations retaining the chemical environment that they exhibit in the pure oxides. The fraction of C-type phase increases with temperature to indicate that vacancy ordering occurs in a larger part of the sample. At the same time, the increase of the *x* coordinate of the La2 site suggests O redistribution between the two phases at the nanoscale.

References

[*Argyriou, 1994*] D. N. Argyriou, *J. Appl. Cryst.* 1994, **27**, 155-158.

[*Balducci et al., 2003*] G. Balducci, M. S. Islam, J. Kaspar, P. Fornasiero and M. Graziani, *Chem. Mater.* 2003, **15**, 3781-3785.

[*Billinge and Farrow, 2012*] S. J. L. Billinge and C. L. Farrow, 2012, arXiv:1211.4284.

[*Brunelli and Fitch, 2003*] M. Brunelli and A. N. Fitch, *J. Synchrotron Rad.* 2003, **10**, 337-339.

[*Chavan and Tyagi, 2005*] S. V. Chavan and A. K. Tyagi, *Materials Science and Engineering A* 2005, **404**, 57–63

[*Hammersley et al., 1996*] A. P. Hammersley, S. O. Svensson, M. Hanfland, A. N. Fitch and D. Hausermann, *High Pressure Research* 1996, **14**, 235-248.

[*Li et al., 2011*] Z.-P. Li, T. Mori, F. Ye, D. Ou, G. J. Auchterlonie, J. Zou and J. Drennan, *J. Phys. Chem. C* 2012, **116**, 5435-5443.

[*Lorch, 1969*] E. Lorch, *J. Phys. C* 1969, **2**, 229-237.

[*Kümmerle and Heger, 1999*] E.A. Kümmerle and G. Heger, *J.Sol.State. Chem.* 1999, **147**, 485-500.

[*Scavini et al., 2010*] M. Scavini, M. Coduri, M. Allieta, L. Mollica, M. Brunelli, L. Malavasi and A. Lascialfari, C. Ferrero, *The Journal of Physical Chemistry C*, 2010, **114**, 19509-20.

[*Shannon, 1976*] R. D. Shannon, *Acta Cryst.* 1976,**A32**, 751-767.

[*Shimonosono et al., 2005*] T. Shimonosono, Y. Hirata, S. Sameshima and T. Horita, *J. Am. Ceram. Soc*. 2005, **88**, 2114-2120.

[*Toby and Egami 1992*] B. H. Toby and T. Egami, *Acta cryst.* 1992, **A48**, 336-346.

7. Final remarks

In this final section we sum up the results shown in the previous chapters.

The investigations reported in chapters 4 and 5 were all performed at low temperature. Even though this is an extremely different condition compared to that of application, low temperature has been of utmost importance in order to probe local deviations from the average structure and, most important, to determine a fingerprint of disorder. The occurrence of a clear unexpected peak in the PDF (the peak "C") of long range fluorite samples is our compass in unveiling the doping induced disorder.

A number of samples were prepared and investigated, but for sake of simplicity not all of them were shown in this thesis. This was done in order to strictly relate each chapter to a different thematic of interest in doped ceria.

Chapter 4 was introduced to establish what accompanies, from a structural point of view, the conductivity drop in doped ceria. By changing the doping concentration along the whole compositional range of the CeO_2-RE_2O_3 solid solutions, we observed a continuum of structural evolution, both locally and on average. The presence of the peak C in PDF was successfully modeled only considering the presence of RE_2O_3-rich droplets embedded in a ceria matrix. The part of the sample having such a local scale C-type ordering increases with doping along the whole solid solutions.

In the framework of the formation of C-type-like orderings with doping, the peak in conductivity can be viewed as the results of two competing effects: on the one hand, doping increases the number of oxygen vacancies available for oxygen migration; on the other hand, the continuous growing of C-type structure traps increasingly more oxygen vacancies with doping. The evolution of the C-type structure with doping is testified by the steep increase of the area of the peak C and by the formation of superstructure peaks in XRPD patterns. Note that a signal resembling the peak C was also observed in NPD PDF, but it was not possible resolve it from the adjacent peaks.

In chapter 5, we deal with the issue of the different performance of doped ceria when changing the nature of the dopant. In principle, the same amount of each trivalent dopant is expected to introduce the same amount of vacancies. Again we have to think in terms of the fraction of oxygen vacancies that are free for

oxygen migration. Based on our local scale modeling, this is determined by the part of the sample that locally arranges with a C-type structure, defined as C-type fraction. This is observed to depend on the ionic radius of the dopant and features a similar trend to the one observed in the literature for transport properties: the maximum conductivity, as well the smallest C-type fraction, is observed upon Gd and Sm-doping.

The combination of two different probes was fundamental to gain a comprehensive view of local orderings in doped ceria. The use of only XRPD doesn't allow an accurate description of O-related parameters. This is not the case of NPD, which provides evidence of O relaxation towards the doping induced vacancies. The magnitude of such relaxation can be considered as an index of the structural distortion induced by the dopant. Again its dependence on the dopant ionic radius resembles the one observed for transport properties. The use of a single probe, either X-rays or Neutrons, would lead to an incomplete description of the local scale disorder.

From low temperature investigations, we gained insight into the local structure of doped ceria. They provided the necessary background to face the investigation of the high temperature behavior of this material, which is the one really interesting from the applicative point of view.

This was done in chapter 6, by collecting PDF at high temperature and under controlled atmosphere. Compared to low temperature studies, we observed that at high temperature a similar, though more complex, local ordering occurs. The part of the sample having locally C-type structure increases with temperature, and O redistribution at the nanoscale was observed. The long range fluorite structure is retained even under reducing atmosphere, which induces larger distortions at the local scale. This is turn is consistent with the partial reduction of Ce^{+4} to Ce^{+3}. The study of high temperature NPD-PDF will provide a more direct information about O orderings.

The investigations reported so far were all of crystallographic nature.

In this work we match the transport properties of our samples with reference to literature data. However, a number of parameters can affect the actual performance of a doped ceria compound. The comparison with the transport properties probed on the very same samples of this study would be a more persuasive evidence of the interplay between the local disorder we mapped and the actual transport properties. As to the future development of the present project, we recently started an investigation of Electrochemical Impedance Spectroscopy spectra on our samples in collaborations with the University of Montpellier. These

investigations are also aimed at determining how the local structure, with reference to the transport properties, is affected by different synthesis routes.

Appendix

A4.1 Results of Rietveld refinements

Here follows a set of tables reporting the results of the Rietveld refinements of XRPD patterns discussed in chapter 4.

***x*(Sm)**	**0**	**0.125**	**0.250**	**0.3125**
phase	F	F	F	F
a	5.407196(2)	5.42136(1)	5.43504(5)	5.44129(2)
U(M)	0.00120(1)	0.00405(1)	0.00854(2)	0.01135(3)
U(O)	0.00347(3)	0.0081(1)	0.0152(2)	0.0180(3)
***R*(F^2)**	0.0281	0.0230	0.0337	0.0891
R_{wp}	0.0574	0.0514	0.0499	0.0595

***x*(Sm)**	**0. 34375**	**0.375**	**0. 40625**	**0. 4375**
phase	C*	C*	C*	C*
a	10.88899(9)	10.89125(6)	10.89691(5)	10.89954(5)
x(M2)	-0.00131(7)	-0.00471(6)	-0.00755(5)	-0.01067(5)
x(O1)	0.375	0.375	0.3798(7)	0.3802(7)
y(O1)	0.125	0.125	0.1348(6)	0.1384(7)
z(O1)	0.375	0.375	0.3779(10)	0.3802(8)
x(O2)	0.375	0.375	0.375	0.3794(14)
U11(M1)	-	-	0.0199(8)	0.0241(7)
U12(M1)	-	-	0.0172(5)	0.0212(5)
U11(M2)	-	-	-	-
U22(M2)	-	-	-	-
U33(M2)	-	-	-	-
U23(M2)	-	-	-	-
Uan(M1)	0.01325(4)**	0.01407(6)**	0.0199(8)	0.0241(7)
Uan(M2)	0.01325(4)**	0.01407(6)**	0.0147(3)	0.0138(2)
U(O)	0.0210(3)	0.0229(5)	0.0205(5)	0.0187(6)
***R*(F^2)**	0.0530	0.1338	0.0827	0.0936
R_{wp}	0.0716	0.0876	0.0961	0.0792

**U(M1) and UM(2) constrained to the same value.

***x*(Sm)**	**0. 500**	**0. 5625**	**0. 625**	**0.6875**	**0.750**	**0. 8125**
phase	C	C	C	C	C	C
a	10.90639(4)	10.91253(2)	10.9164(2)	10.92300(2)	10.92294(3)	10.92402(2)
x(M2)	-0.01582(3)	-0.01762(3)	-0.01932(2)	-0.02103(2)	-0.02315(1)	-0.02519(2)
x(O1)	0.3845(3)	0.3810(3)	0.3825(3)	0.3830(3)	0.3835(3)	0.3859(2)
y(O1)	0.1392(3)	0.1444(3)	0.1452(3)	0.1470(2)	0.1469(3)	0.1471(2)
z(O1)	0.3841(4)	0.3781(5)	0.3783(4)	0.3791(3)	0.3786(4)	0.3802(3)
x(O2)	0.3817(9)	0.382(11)	0.3848(10)	0.380(2)	0.3841(11)	0.3865(9)
U11(M1)	0.0266(4)	0.0289(4)	0.02678(4)	0.0252(3)	0.0190(2)	0.01328(14)
U12(M1)	0.0192(4)	0.0202(4)	0.0188(4)	0.0172(3)	0.0136(2)	0.0098(2)
U11(M2)	0.00418(12)	0.0042(10)	0.00463(10)	0.00557(10)	0.00546(7)	0.00449(8)
U22(M2)	0.0138(3)	0.0124(2)	0.0103(2)	0.01052(16)	0.00895(11)	0.00669(12)
U33(M2)	0.0100(3)	0.0130(3)	0.0135(3)	0.0130(3)	0.0118(2)	0.0086(2)
U23(M2)	-0.0101(2)	-0.0110(2)	-0.00982(15)	-0.00858(14)	-0.00650(11)	-0.00420(12)
Uan(M1)	0.0266(4)	0.0289(4)	0.0268(4)	0.0252(3)	0.0190(2)	0.01328(14)
Uan(M2)	0.0093(3)	0.0099(2)	0.0095(2)	0.0097(2)	0.00872(13)	0.00660(13)
Uan(O)	0.0175(5)	0.0143(6)	0.0118(6)	0.0176(5)	0.0099(5)	0.0076(6)
***R*(F^2)**	0.0672	0.0500	0.0435	0.0340	0.0358	0.0212
R_{wp}	0.0807	0.0524	0.0577	0.0459	0.0441	0.0540

***x*(Sm)**	**0. 875*** **	**0. 9375** **	**1**
phase	C+B	C+B	C
a	10.9256(8)	10.9255(2)	10.92595(5)
x(M2)	-0.02707(4)	-0.02876(7)	-0.03031(1)
x(O1)	0.3871(2)	0.3884(2)	0.3902(2)
y(O1)	0.1475(2)	0.1483(2)	0.1509(2)
z(O1)	0.3801(3)	0.3809(3)	0.3804(2)
x(O2)	0.3873(14)	0.383(2)	-
U11(M1)	0.0100(2)	0.0068(4)	0.00268(4)
U12(M1)	0.0091(4)	0.00757)	0.00095(9)
U11(M2)	0.00424(15)	0.0031(3)	0.00237(5)
U22(M2)	0.0054(2)	0.0037(4)	0.00219(8)
U33(M2)	0.0068(3)	0.0042(6)	0.00214(10)
U23(M2)	-0.0027(2)	-0.0014(4)	-0.00040(7)
Uan(M1)	0.0100(2)	0.0068(4)	0.00268(4)
Uan(M2)	0.0055(2)	0.0037(4)	0.00223(8)
Uan(O)	0.0091(9)	0.0054(17)	0.0061(4)
***R*(F^2)**	0.0196	0.0150	0.0209
R_{wp}	0.0476	0.0498	0.0515

19.3(1) weight fraction of B-type phase;*6.5(1) weight fraction of B-type phase

***x*(Y)**	**0.125**	**0.250**
phase	F	F
a	5.405631(5)	5.403207(9)
U(M)	0.00338(1)	0.00721(2)
U(O)	0.00633(7)	0.01112(14)
$R(F^2)$	0.0396	0.0466
R_{wp}	0.0489	0.0509

***x*(Y)**	**0.3125**	**0. 34375**	**0. 375**	**0.4375**
phase	C*	C*	C*	C*
a	10.79171(5)	10.7853(6)	10.78575(2)	10.77380(5)
xM2	-0.00267(12)	-0.00449(9)	-0.00623(5)	-0.01159(3)
x(O1)	0.3697(10)	0.3716(16)	0.3773(8)	0.3785(3)
y(O1)	0.1264(11)	0.1286(18)	0.1353(7)	0.1406(3)
z(O1)	0.377(2)	0.377(3)	0.3781(9)	0.3785(5)
x(O2)	0.379(3)	0.379(3)	0.3762(15)	0.3759(11)
U11(M1)	0.0123(15)	0.013(2)	0.0159(16)	0.0195(8)
U12(M1)	0.0076(9)	0.0097(10)	0.0112(6)	0.0127(5)
U11(M2)	0.0127(6)	0.0131(1)	0.0070(6)	0.0072(2)
U22(M2)	0.0057(5)	0.00880(10)	0.0176(12)	0.0078(3)
U33(M2)	0.012(2)	0.013(2)	0.015(2)	0.0231(8)
U23(M2)	-0.0029(8)	-0.0045(7)	-0.0035(5)	-0.0082(3)
Uan(M1)	0.0122(15)	0.013(2)	0.0159(16)	0.0195(8)
Uan(M2)	0.0101(14)	0.0117(23)	0.0133(17)	0.0127(7)
U(O)	0.0153(5)	0.0175(4)	0.0163(4)	0.0190(4)
$R(F^2)$	0.0745	0.0896	0.0436	0.0410
R_{wp}	0.0795	0.0863	0.0652	0.0703

***x*(Y)**	**0. 500**	**0.750**	**0. 875**	**1**
phase	C	C	C	C
a	10.75948(8)	10.69048(6)	10.65044(4)	10.601548(8)
xM2	-0.01497(4)	-0.02406(3)	-0.02828(2)	-0.03243(2)
x(O1)	0.3809(4)	0.3849(3)	0.3892(2)	0.3910(1)
y(O1)	0.1425(4)	0.1493(2)	0.1504(2)	0.15140(14)
z(O1)	0.3809(4)	0.3794(3)	0.3805(2)	0.38013(14)
x(O2)	0.3766(12)	0.3834(14)	0.3856(18)	-
U11(M1)	0.0246(7)	0.0173(3)	0.00933(13)	0.00192(5)
U12(M1)	0.0169(5)	0.0154(4)	0.0063(2)	0.00039(11)
U11(M2)	0.0066(2)	0.0060(2)	0.00463(10)	0.00146(6)
U22(M2)	0.0079(3)	0.0074(2)	0.00578(14)	0.00161(9)
U33(M2)	0.0218(8)	0.0120(4)	0.0073(2)	0.00163(10)
U23(M2)	-0.0094(2)	-0.0071(2)	-0.00329(15)	-0.00019(8)
Uan(M1)	0.0246(7)	0.0173(3)	0.00933(13)	0.00192(5)
Uan(M2)	0.0121(6)	0.0085(4)	0.0059(2)	0.00157(13)
U(O)	0.0165(4)	0.0115(4)	0.0088(4)	0.00464(3)
$R(F^2)$	0.0521	0.0392	0.0223	0.0183
R_{wp}	0.0485	0.0475	0.0635	0.0656

***x*(Gd)**	**0.125**	**0.250**
phase	F	F
a	5.41406(2)	5.42165(4)
U(M)	0.00500(3)	0.00959(5)
U(O)	0.0088(2)	0.0156(4)
$R(F^2)$	0.0883	0.0982
R_{wp}	0.0568	0.0598

***x*(Gd)**	**0.3125**	**0. 34375**	**0. 375**	**0.4375**
phase	C*	C*	C*	C*
a	10.84729(5)	10.84760(4)	10.85482(6)	10.85488(4)
xM2	-0.00336(10)	-0.00564(6)	-0.00823(6)	-0.01325(4)
x(O1)	0.375	0.375	0.375	0.3805(5)
y(O1)	0.125	0.125	0.125	0.1375(4)
z(O1)	0.375	0.375	0.375	0.3828(4)
x(O2)	0.375	0.375	0.375	0.375
U11(M1)	0.015(2)	0.0182(10)	0.0207(8)	0.0232(6)
U12(M1)	0.0089(7)	0.0088(11)	0.0177(6)	0.0133(5)
U11(M2)	-	0.0075(6)	-	0.0144(2)
U22(M2)	-	0.0200(14)	-	0.0087(5)
U33(M2)	-	0.0122(8)	-	0.0166(8)
U23(M2)	-	-0.0074(7)	-	-0.0110(3)
Uan(M1)	0.015(2)	0.0182(10)	0.0207(8)	0.0232(6)
Uan(M2)	0.0120(5)	0.0132(9)	0.0145(2)	0.0132(5)
U(O)	0.0121**	0.0133**	0.0144**	0.0137**
$R(F^2)$	0.0975	0.0995	0.1046	0.0922
R_{wp}	0.0889	0.0923	0.0899	0.781

** *U*(O) was fixed equal to the average *msd*.

***x*(Gd)**	**0. 500**	**0.750**	**0. 875**	**1**
phase	C	C	C	C
a	10.85240(7)	10.83741(9)	10.82602(11)	10.80931(13)
xM2	-0.01661(5)	-0.02395(3)	-0.02769(3)	-0.03138(4)
x(O1)	0.3831(6)	0.3848(4)	0.3874(4)	0.3919(5)
y(O1)	0.1403(6)	0.1479(4)	0.1511(4)	0.1518(5)
z(O1)	0.3842(8)	0.3821(5)	0.3811(5)	0.3822(5)
x(O2)	0.382(2)	0.383(2)	0.388(2)	-
U11(M1)	0.0293(6)	0.0195(3)	0.0094(2)	0.00214(16)
U12(M1)	0.0191(6)	0.0135(4)	0.0085(3)	0.0012(3)
U11(M2)	0.0063(2)	0.0070(2)	0.0042(2)	0.0011(2)
U22(M2)	0.0178(5)	0.0104(2)	0.0053(2)	0.0023(3)
U33(M2)	0.0112(4)	0.0130(4)	0.0065(4)	0.0019(3)
U23(M2)	-0.0126(3)	-0.0068(2)	-0.0026(2)	-0.00015(25)
Uan(M1)	0.0293(6)	0.0195(3)	0.0094(2)	0.0021(2)
Uan(M2)	0.0118(4)	0.0101(3)	0.0053(2)	0.0018(3)
U(O)	0.0173(7)	0.0160(7)	0.0065(8)	0.0023(10)
$R(F^2)$	0.0939	0.0599	0.0500	0.0439
R_{wp}	0.0574	0.0497	0.0498	0.0853

A4.2 Discussion on the peak "C" observed in X-ray PDF at ~4.1 Å

For all the present investigation, see section 2.1 and references therein for further details.

The appearance of ripples in the low *r* region of a given G(*r*) curve can be due to different reasons. Since the G(*r*) is obtained as the Fourier transform (FT) from Q_{min}~0 to Q_{max} of the *S*(*Q*), the finite Q_{max} value at which the experiment is performed, leads to the formation of the so called termination ripples. In this case, the ideal G(*r*) is convoluted with a *sinc* function which gives rise to the ringing on both sides of the peaks especially at low r values. From the experimental point of view this effect can be reduced by collecting data at high Q_{max} values, whereas in the modeling process the effect can be easily taken into account by a suitable convolution operation.

Basically, at high *Q* the signal is damped owing to the Debye-Waller effect as well as the broadening due to the instrumental resolution. For this reason, in order to increase the signal to noise ratio, data have to be collected for longer times at high *Q*. By considering that the total FT of the data includes the signal from noise, the latter introduces both oscillations and PDF peak broadening in the real space. In addition, the magnitude of this effect does not decrease with *r* and given its random origin it cannot be taken into account in the structural refinement. Hence, the Q_{max} value has to be evaluated by taking into account the termination effect, which requires high Q_{max} in order to be reduced, as well as the noise, which increases upon increasing *Q*.

Although all the XRPD patterns were collected in very similar experimental conditions (Q_{max} = 28.0 Å^{-1}, same acquisition time, *T* = 90 K), pure CeO_2 and lightly doped samples show stronger ripples than the other samples. To show clearly how the Debye-Waller and the instrumental resolution cause the presence of ripples in the *G*(*r*) pattern, in the following we report simulations related to CeO_2 short range PDF taken as a reference sample.

Reciprocal space analysis on CeO_2 at 90 K yielded very low *msd*: *U*(Ce) = 0.00091(1) Å^2; *U*(O) = 0.00302(6) Å^2. The *S*(*Q*) related to this sample (not reported) shows that the Ce structure factor significantly contributes to the scattering even at *Q* ~ 30 Å^{-1}. The presence of strong Bragg scattering at high *Q* introduces difficulties into the normalization process since the condition S(*Q*) → 1 is not fulfilled. If the high *Q* region of S(*Q*) is not properly normalized the S(*Q*) will have a step at the termination at Q_{max} and produces strong

ripples in G(r). It can be easily demonstrated that in such a case a much higher Q_{max} would be required. In particular, the amplitude of the ripples reduces by increasing the Debye-Waller factor at a given Q_{max}. In Fig.A4.1 the calculated G(r) for CeO_2 are reported using different Q_{max} values. At Q=50 Å^{-1} some minor oscillations are still present. When the *msd* are increased up to U(Ce/*RE*) = 0.004 Å^2; U(O) = 0.008 Å^2, which are far lower than those observed in the doped samples, ripples are no longer visible. This is shown in the right-hand panel of Fig. A4.1.

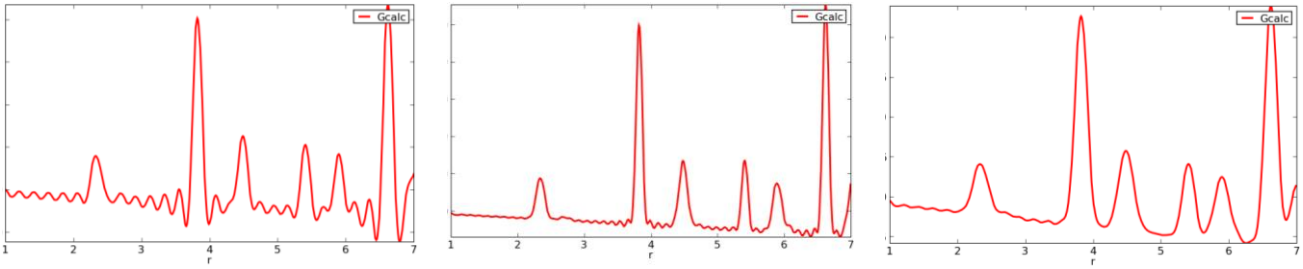

Fig. A4.1. Calculated G(r) for CeO_2, considering Q_{max}=29.4 (left) and 50 Å^{-1} (middle) using Q_{damp} =0.004, Q_{broad} 0.008, U(Ce) = 0.00091 Å^2; U(O) = 0.00302 Å^2 in the 1 < r < 7 Å range. In the rightmost panel *msd* are risen up to U(Ce/*RE*) = 0.004 Å^2; U(O) = 0.008 Å^2, considering Q_{max} = 29.4 Å^{-1}.

The doped samples are characterized by a large amount of disorder, which in turn induces a strong increase of the observed *msd* parameters, the structure factor is thus damped at lower Q values than in pure CeO_2 and at Q=28 Å^{-1} the S(Q) is well normalized.

When the long range structure is still fluorite, the *msd* are quite small and the sample behaves, though to a lesser extent, like CeO_2.

Finally, the instrumental resolution function can cause the damping of the signal at high Q, owing to the induced broadening of the Bragg peaks in the reciprocal space. Nevertheless the ID31 diffractometer is characterized by an extremely high resolution and this effect is almost negligible. On the other hand, this is not the case of the D4c instrument (Q_{damp} ~0.04), since at 23.6 Å^{-1} the intensity of CeO_2 is damped by the instrument resolution.

In Fig. A4.2 the experimental short range PDF of CeO_2 is shown. In this pattern a feature at about 4.1 Å is present. Since this r-value is not too much different from the small peak not accounted for by the fluorite model, the reader could argue that it can be the same observed in the doped samples.

In Fig. A4.2 also the real space refinement of the low-r CeO_2 G(r) is shown (solid line). This is reported also in the main text in chapter 5 in Fig. 5.11 for XRPD and NPD. The observed pattern is correctly described by the fluorite model and the ripple at ~4.1 Å is correctly fitted by including the truncation effect

due to the Q_{max} in our model. Since the peak at ~4.1 Å is not predicted by the CeO_2 symmetry, the correct interpretation of all the peaks by our model provides evidence that the peak at ~4.1 Å is due to a termination ripple.

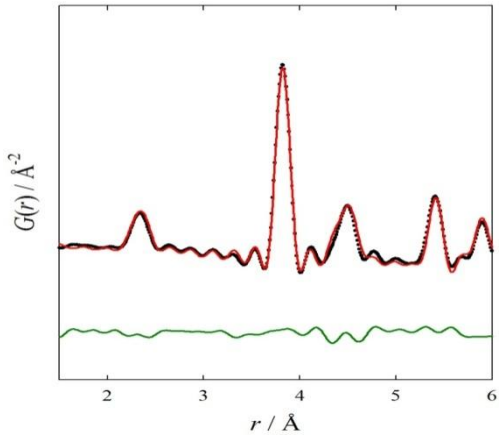

Fig. A2. Black dots: Experimental CeO_2 G(*r*), red line: Calculated G(*r*) by fluorite model, green line: Residual.

If we consider the short range G(*r*) related to doped samples, we have noted that the ~4.1 Å peak has been never fitted by the fluorite model, as shown in chapter 5, Fig.5.11. This supports the fact that the ~4.1 Å peak observed in pure CeO_2 has nothing to do with structural feature but only with the data reduction process. Moreover the fit of the NPD G(*r*) of CeO_2 gave very small residual supporting that pure CeO_2 is very ordered even at the nanoscale with no local deviations with respect to the fluorite structure. In general, even the small ripple arising on the left side of peak at ~3.8 Å is correctly fitted employing the *biphasic* model, while this is not the case with the *average* one. Indeed, to account for static disorder the *average* model produces a large *msd*, not consistent with the observed ripples.

Formerly in chapter 5, we demonstrated that the area of the peak at ~4.1 Å, normalized to the one of the nearly peak at ~3.8 Å, is the same within the standard deviation for all the dopants, except for Y. Being Y characterized by a lower scattering factor than the other dopants, a lower area observed upon Y-doping is a further evidence that *RE* dopant ions contribute to this peak.

Finally, we cannot exclude the position of the peak to be somehow affected by the presence of some spurious oscillations, particularly for the *x*(*RE*)=0.125 composition

The *x*(Y)=0.25 sample was measured twice at the ID31: at 0.3099 Å (8 hours), just below the Ce K-absorption edge and at 0.3541 Å (3 hours). away from Ce and Y absorption edges.

Being the former dataset collected just below the Ce K-absorption edge, it is characterized by larger ripples, which most likely do not arise from truncation effects (the Q_{max} is the same), but from noise.

As a consequence, the C-type-like peak in the PDF collected just below edge is detected at ~4.14 Å, whereas away from absorption edges at ~4.10 Å. Note that the latter is plotted in Fig 4.11 of the main text and is in line with the trend as a function of dopant concentration. Conversely, for the *x*(Y)=0.125 sample (measured below edge) the peak occurs at a larger interatomic distance. The same effect is observed with Sm: the smallest doping fraction (x = 0.125, 0.250) correspond to a larger peak distance compared to the samples having slightly large doping amount, but collected away from edge

A4.3 Results of *biphasic model*

Results of the biphasic model for all the samples investigated with the PDF method. By increasing the dopant concentration, the general trend is the increase of the C-type fraction and the shift of the *x*(*RE2*) coordinates towards more negative values.

	Y		*Gd*		*Sm*	
x(RE)	*C-type frac.*	*x(RE2)*	*C-type frac.*	*x(RE2)*	*C-type frac.*	*x(RE2)*
0.125	0.0858(9)	-0.0245(2)	0.123(2)	-0.0252(4)	0.150(5)	-0.0266(4)
0.250	0.259(2)	-0.0282(1)	0.199(3)	-0.0262(3)	0.225(3)	-0.0264(4)
0.3125	0.262(2)	-0.0282(2)	0.263(3)	-0.0276(4)	0.240(3)	-0.0270(3)
0.34375	0.297(3)	-0.0298(3)	0.301(3)	-0.0282(3)	0.260(4)	-0.0279(3)
0.375			0.295(3)	-0.0292(3)	0.294(3)	-0.0291(3)
0.4375	0.368(4)	-0.0304(2)	0.374(3)	-0.0305(5)	0.341(3)	-0.0310(3)
0.500	0.432(4)	-0.0319(3)	0.323(2)	-0.0321(4)	0.401(2)	-0.0315(4)
0.625					0.467(4)	-0.0308(2)
0.750	0.651(4)	-0.0320(3)	0.6378(4)	-0.0302(3)	0.645(2)	-0.0288(3)
0.875			0.820(3)	-0.0309(2)		

A5.1 combined XRPD and NPD refinements

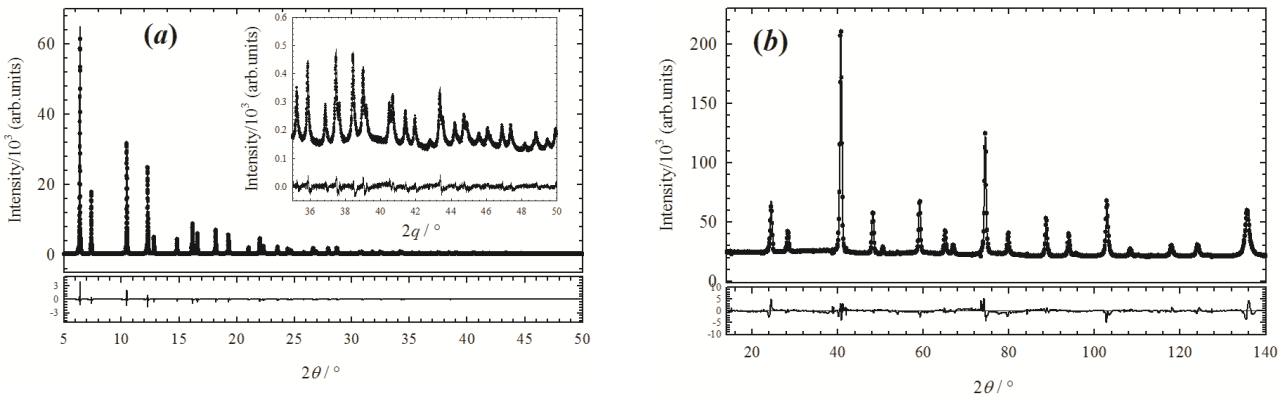

Fig. A5.1. XRPD (a) and NPD (b) for *RE*=La collected at T = 90K.

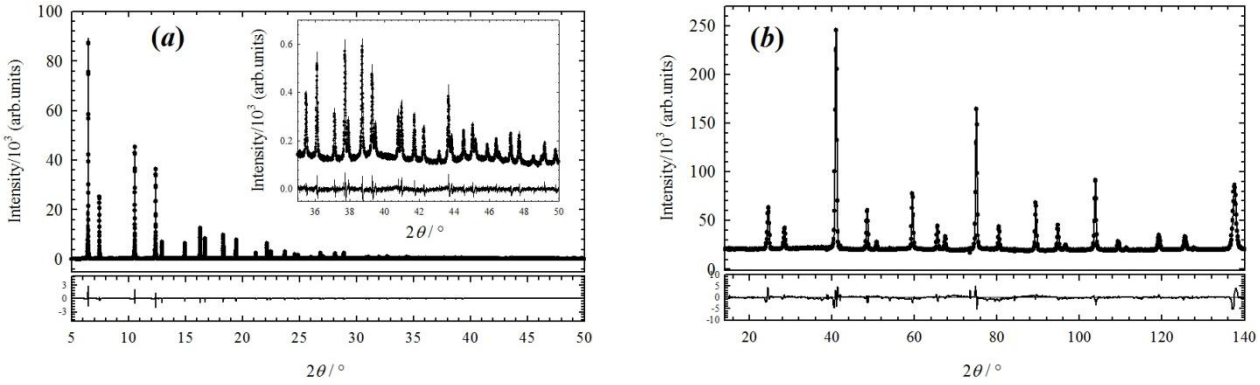

Fig. A5.2. XRPD (a) and NPD (b) for *RE*=Nd collected at T = 90K.

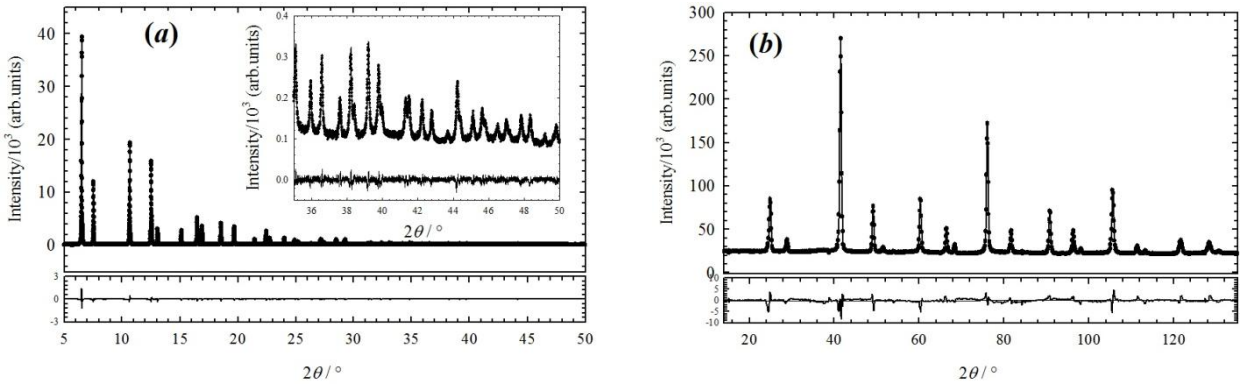

Fig. A5.3. XRPD (a) and NPD (b) for *RE*=Yb collected at T = 90K.

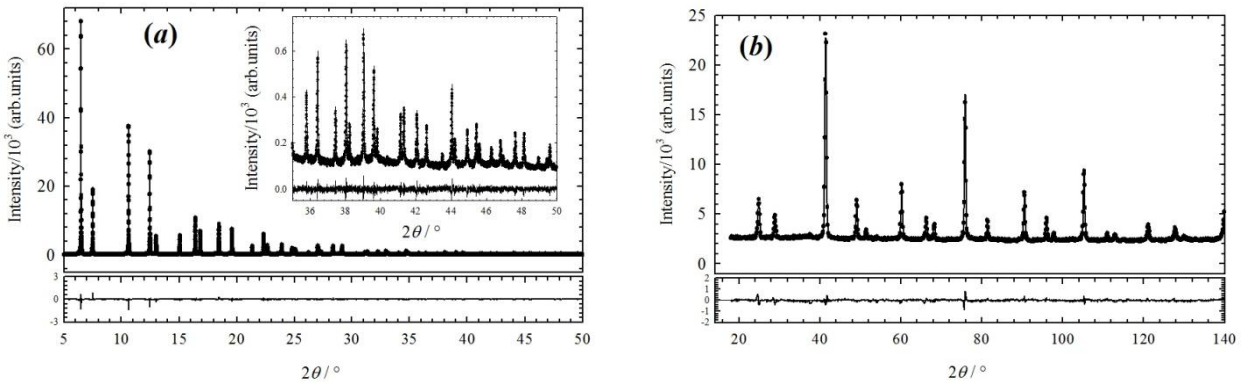

Fig. A5.4. XRPD (a) and NPD (b) for *RE*=Y collected at T = 90K.

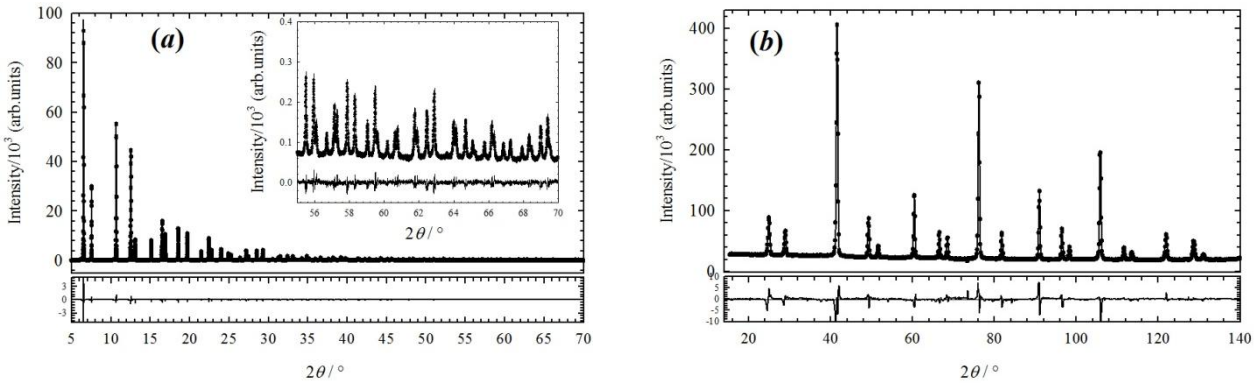

Fig. A5.5.. XRPD (a) and NPD (b) for *RE*=Tb collected at T = 90K.

Results of the combined refinement (X+N) performed on x(Y)=0.500 with data collected at T = 90 K for both datasets collected at the D20 instrument of the ILL and at the ID31 beamline of the ESRF. They are compared to the results of the refinement of the only XRPD pattern.

***x*(Y)**	**0. 500 X**	**0.500 X+N**
phase	C	C
a	10.75948(8)	10.76044(9)
xM2	-0.01497(4)	-0.01501(5)
x(O1)	0.3809(4)	0.3807(3)
y(O1)	0.1425(4)	0.1413(2)
z(O1)	0.3809(4)	0.3798(3)
x(O2)	0.3766(12)	0.3816(6)
U11(M1)	0.0246(7)	0.0253(9)
U12(M1)	0.0169(5)	0.0169(5)
U11(M2)	0.0066(2)	0.0070(2)
U22(M2)	0.0079(3)	0.0076(3)
U33(M2)	0.0218(8)	0.0211(10)
U23(M2)	-0.0094(2)	-0.0096(3)
U11(O1)	-	0.0257(10)
U22(O1)	-	0.0134(10)
U33(O1)	-	0.0113(7)
U12(O1)	-	-0.0108(7)
U12(O1)	-	-0.0006(7)
U12(O1)	-	-0.0047(6)
Uan(M1)	0.0246(7)	0.0253(9)
Uan(M2)	0.0121(6)	0.0119(5)
Uan(O)	0.0165(4)	0.0168(9)
$R(F^2)$	0.0521	0.0521-0.729
R_{wp}	0.0485	0.490-0.432

A6.1 Data correction at ID11

From the analysis of the G(r) curves, we observed that the r-position of the G(r) peaks were larger than expected, this effect amplifying with increasing r. In order to correct for this aberration, we collected a XRPD pattern at the ID31 beamline of the ESRF at an incident wavelength 0.3191 Å at T=100°C on $Ce_{0.75}La_{0.25}O_{1.875}$. Due to its very narrow instrumental resolution function, at ID31 it is possible to determine the cell parameter with very high accuracy. Once known the cell parameter, a G(r) was calculated based on the fluorite structural model and using proper thermal parameters to simulate the experimental G(r) curves.

As discussed in chapter 4 and 5, from ~10 Å on, the G(r) of doped ceria can be correctly described by the fluorite structure. For this reason the calculated PDF can be used a reference. Note that peak positions

deriving from the average structure cannot be used directly as reference, since both Ce-Ce and Ce-O pairs contribute to some G(*r*) peaks.

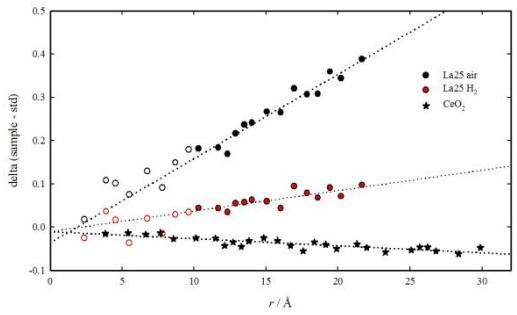

Fig. A6.1. *r*-position mismatch between observed and calculated peak positions. Black circles: La25air, red circles: La25H2, stars: ceria. Empty circles are points not considered in the linear regression.

In Fig. A6.1 the mismatch between the peak *r*-positions observed in the collected PDF and those calculated is plotted as a function of *r*. The data in the $10 < r < 25$ Å range were fitted with a linear regression.

The *r* position in G(*r*) was then corrected with the equation

$$r_N = r_E - mr_E - q \qquad \text{(A6.1)}$$

where r_N stands for normalized *r* peak position, r_E for observed peak position, *m* is the slope of the regression line and *q* its intercept. This correction is based on the assumption that no reduction occurs at *T*=100°C, that is La25air and La25H2 exhibit the same structure.

It should be noted that this correction does not modify the temperature evolution of a peak, but rather it is fundamental in order to compare sample distances and for fitting a structural model over a wide *r* range. This is the case, for example, of the determination of instrumental related parameters (e.g. Q_{damp} and Q_{broad} in PDFGUI), which require the refinement of a reference structure over a wide *r*-range.

List of publications:

1. M. Scavini, M. Coduri, M. Allieta, L. Mollica, M. Brunelli, L. Malavasi, A. Lascialfari and C. Ferrero, *"Effect of local disorder on the transport properties of Al doped $SmBa_2Cu_3O_{6+\square}$ superconductor"* *The Journal of Physical Chemistry C*, 2010, **114**, 19509-20.
2. M. Allieta, M. Brunelli, M. Coduri, M. Scavini and C. Ferrero, "*Differential Pair Distribution Function applied to $Ce_{1-x}Gd_xO_{2-x/2}$ system*" *Zeitschrift für Kristallographie Proceedings* 2011, **1**, 15-20.
3. M Coduri, M Scavini, M Allieta, M Brunelli and C Ferrero, "*Local disorder in yttrium doped ceria ($Ce_{1-x}Y_xO_{2-x/2}$) probed by joint X-ray and Neutron Powder Diffraction*" *Journal of Physics: Conference Series* 2012, **340**, 012056.
4. M. Coduri, M. Brunelli, M. Scavini, M. Allieta, P. Masala, L.Capogna, H.E. Fischer and C. Ferrero, "*Rare Earth doped ceria: a combined X-ray and Neutron Pair Distribution Function study*" *Zeitschrift für Kristallographie* 2012, **227**, 272-279.
5. M. Scavini, M. Coduri, M. Allieta, M. Brunelli, C. Ferrero, *"Probing complex disorder in $Ce_{1-x}Gd_xO_{2-x/2}$ using the Pair Distribution Function Analysis*", *Chemistry of Materials* 2012, **29**, 1338-1345.
6. M. Scavini and M. Coduri, *"Disorder in oxides"* *Current Inorganic Chemistry*, in press

Acknowledgements

So, three years is a lot of time. . three years later the last thesis, again the same mistake. It's late night and the most of the work is done, the thesis is "ready" to be submitted. But something is still lacking.. the acknowledgements..

Let's start with the group, the first thanks go to the boss Marco Scavini for introducing me in this strange life of research, synchrotrons and coffees. More than a colleague, a big thanks to Mattia Allieta, the best powder diffractionist ever. But also a friend, which is far better. And then Paolo J Masala, last but not least, sometimes laziness hides wisdom.

Thanks to the Grenoblois, Michela Brunelli and Claudio Ferrero (öööhh...). After days spent together, especially nightshifts, they are now more than colleagues. Also thanks to Henry Fischer for usefule and very long discussions, to Gavin Vaughan for letting me spend six months in Grenoble, to Prof. Philippe Papet and Marco Longhin in Montpellier and to Monica Dapiaggi and Andrea Bernasconi here in Milan.

Thanks to my family, a special mention goes to my parents. Not only because without them I wouldn't be here. And to my aunt Lina, like a grandma. Thanks to the little growing cousins for useful distractions, maybe one day you will read through these pages. A still larger thanks to Ester, the best of the distractions.

And thanks to the uni-friends, expecially to Maviii and Yuriii. Serena (Mrs or Ms?!?).

Thanks to the people who sometimes helped me to get by in these three years, I think of Chiara, Claudia, Ema, Michi e Fede and again Yuri and Mavi.

Thanks to Sant'Elena, but this is not a matter of religion..

And thanks to the people who will decided to spend some of their time to read this thesis or to be at the discussion.

Gute Nacht und viel Glück.

Mauro